

**DEVELOPMENT OF CONFORMATIONAL MYOCILIN
ANTIBODIES, AND BIOPHYSICAL CHARACTERIZATION OF
THE MOUSE MYOCILIN OLFACTOMEDIN DOMAIN**

A Dissertation
Presented to
The Academic Faculty

by

Athéna C. Patterson-Orazem

In Partial Fulfillment
of the Requirements for the Degree
Doctor of Philosophy in the
School of Chemistry and Biochemistry

Georgia Institute of Technology
May, 2019

COPYRIGHT © 2019 BY ATHÉNA C. PATTERSON-ORAZEM

**DEVELOPMENT OF CONFORMATIONAL MYOCILIN
ANTIBODIES, AND BIOPHYSICAL CHARACTERIZATION OF
THE MOUSE MYOCILIN OLFACTOMEDIN DOMAIN**

Approved by:

Dr. Raquel Lieberman, Advisor
School of Chemistry and Biochemistry
Georgia Institute of Technology

Dr. Loren Williams
School of Chemistry and Biochemistry
Georgia Institute of Technology

Dr. Adegboyega Oyelere
School of Chemistry and Biochemistry
Georgia Institute of Technology

Dr. Cheng Zhu
Department of Biomedical Engineering
Georgia Institute of Technology

Dr. Ingeborg Schmidt-Krey
School of Biology
Georgia Institute of Technology

Date Approved: March 7th, 2019

To those who came before, and to those will come after.

ACKNOWLEDGEMENTS

First, I would like to acknowledge my advisor, Dr. Raquel Lieberman, for her support and guidance throughout my doctoral research. Particular mention is due to Dr. Shannon Hill and Elaine Nguyen for their pioneering work characterizing N-terminal myocilin, but also for ‘teaching me the ropes’ as a new graduate student. My undergraduates, Yemo Ku and Yasmin Ajirniar, have contributed experimental assistance with infectious enthusiasm and constant questions. Additionally, I must thank current and past Lieberman lab members for their teaching, feedback and support throughout the past several years.

I would like to thank my committee members, Dr. Inga Schmidt-Krey, Dr. Yomi Oyelere, Dr. Loren Williams and Dr. Cheng Zhu for their guidance and input on this dissertation. Additionally, my growth as a scientist would be incomplete without numerous research collaborations. Special thanks to Dr. Jennifer Maynard and Jeong-min Hyun for early antibody collaborations which inspired my thesis project, and Ahlam Qerqez for important contributions to our myocilin antibody engineering efforts. I also take this opportunity to acknowledge Dr. Ana Carmona for the opportunity to contribute a crystal structure to an already-international collaboration.

Finally, and most importantly, I would like to acknowledge my parents, Jennifer K. Patterson and Dr. Mark E. Orazem for their love and support throughout my endeavors.

Specific Acknowledgements by Chapter:

Chapter 1. Thanks to Dr. Lieberman for the opportunity to co-author this perspective. Work in the Lieberman lab on myocilin is supported by the National Institutes of Health (NIH) R01EY021205.

Chapter 2. This work was supported by the BrightFocus Foundation and NIH R01EY021205. Additional thanks to I. Dominic, D. J. E. Huard, Y. Ku, for technical assistance, E. Snider and C.R. Ethier for hTM cell media, E. Nguyen for hTM myocilin enrichment, and J. A. Maynard for helpful discussions.

Chapter 3. This work was supported by the BrightFocus Foundation G2016027 (R.L.L.), NIH National Eye Institute R01EY021205 (R.L.L.), Welch Foundation F-1767 (J.A.M.), and NSF GRFP fellowship (A.N.Q.). We thank E. Snider and C. R. Ethier for hTM media, E. Nguyen for hTM myocilin enrichment, J. M. Hyun for mouse immunizations and Y. Ajirniar for experimental assistance. We gratefully acknowledge the Petit Institute (Georgia Institute of Technology) for use of core facilities equipment.

Chapter 4. This work was supported by the NIH (R01EB006006 to C.K.H. and EYR01021205 to R.L.L.), and BrightFocus Foundation G2016027 (R.L.L). SER-CAT is supported by its member institutions (see www.ser-cat.org/members.html), and NIH equipment grants (S10_RR25528 and S10_RR028976). Use of the Advanced Photon Source was supported by the U. S. Department of Energy, Office of Science, Office of Basic Energy Sciences, under Contract No. W-31-109-Eng-38. Additional thanks Y. Ku and Y. Ajirniar for experimental assistance, and the Parker H. Petit Institute for Bioengineering (Georgia Institute of Technology) for use of core facilities equipment.

TABLE OF CONTENTS

ACKNOWLEDGEMENTS	III
LIST OF TABLES	VII
LIST OF FIGURES	VIII
LIST OF SYMBOLS AND ABBREVIATIONS	IX
SUMMARY	XII
CHAPTER 1. Antibodies used to detect glaucoma-associated myocilin: more or less than meets the eye?	1
1.1 Abstract.	1
1.2 Antibodies: important research reagents invite closer scrutiny.	2
1.3 Myocilin: associated with glaucoma yet functionally elusive.	4
1.4 Myocilin antibodies: we don't know what we cannot detect.	6
1.5 The future of myocilin-directed antibodies: our wish list.	8
1.6 Contributions to the future of myocilin antibodies in research.	9
CHAPTER 2. Epitope mapping of Commercial antibodies that detect myocilin.	11
2.1 Abstract.	11
2.2 Introduction.	12
2.3 Materials and Methods.	16
2.3.1 Production of recombinant protein constructs.	16
2.3.2 Enrichment of endogenous hTM-secreted myocilin.	17
2.3.3 Western blots and ELISA.	17
2.4 Results and Discussion.	18
CHAPTER 3. Recombinant antibodies offer conformation-specific targeting of the n-terminal coiled-coils of glaucoma-associated myocilin.	23
3.1 Abstract.	23
3.2 Introduction.	24
Materials and Methods.	27
3.2.1 Commercial Antibodies Used	27
3.2.2 Protein expression and purification: myocilin	28
3.2.3 Mouse Immunization & RT PCR	29
3.2.4 Phage Display Library Construction	29
3.2.5 Phage Production, Purification, & Panning	30
3.2.6 Protein expression and purification: antibodies	33
3.2.7 ELISA & Competition ELISA	34
3.2.8 Dot Blots and Western Blots	35
3.2.9 Immunoprecipitation	36
3.2.10 Differential Scanning Fluorimetry	37

RESULTS	38
3.2.11 Development and identification of candidate antibody sequences	38
3.2.12 Initial evaluation of LZ-targeting scAbs	40
3.2.13 Evaluation of CC-targeting scAbs	42
3.2.14 Conformational specificity of CC- and LZ-targeting IgGs	43
3.3 DISCUSSION	46
CHAPTER 4. Differential misfolding properties of glaucoma-associated olfactomedin domains from human and mouse.	48
4.1 Abstract.	48
4.2 Introduction.	49
4.3 Materials and Methods.	51
4.3.1 Molecular biology.	51
4.3.2 Expression and purification.	52
4.3.3 Crystallization and structure determination.	54
4.3.4 Thermal stability assay.	56
4.3.5 Thioflavin-T (ThT) endpoint fluorescence and de novo aggregation assays.	56
4.3.6 Coarse grain (PRIME20) molecular dynamics simulations.	57
4.3.7 Atomic force microscopy (AFM).	59
4.4 RESULTS	60
4.4.1 MmOLF structure.	60
4.4.2 Thermal stability of wild-type and mutant MmOLFs.	63
4.4.3 Aggregation properties of MmOLF.	67
4.4.4 End-point aggregate morphologies of MmOLF and HsOLF.	71
4.5 DISCUSSION	73
CHAPTER 5. Future Directions.	76
5.1 Introduction.	76
5.2 Optimization of Existing Antibodies.	76
5.3 Development of OLF-Targeting Antibodies.	77
5.4 Anticipated Applications of New Antibodies	78
5.4.1 Diagnostic and Therapeutic Applications of OLF Antibodies	78
5.4.2 Identification of Functional Binding Partners.	79
5.4.3 Visualizing myocilin conformations in biological context.	80
5.4.4 Obtaining high-resolution insight into N-terminal myocilin structure.	80
5.5 Conclusion.	81
REFERENCES	82

LIST OF TABLES

Table 3.1	Commercial antibodies used in antibody development and testing.	27
Table 4.1	Primers used for site-directed mutagenesis of MmOLF and HsOLF used in this manuscript.	52
Table 4.2	Data collection and refinement statistics for the structure of the olfactomedin (OLF) domain of mouse myocilin, PDB 6NAX.	55
Table 4.3	Thermal stability of wild-type and mutant MmOLF resemble HsOLF counterparts.	66

LIST OF FIGURES

Figure 1.1	Artistic renderings of antibody, myocilin, trabecular meshwork and ocular structures.	3
Figure 2.1	Introduction to myocilin structure, commercial antibodies, and protein constructs tested.	14
Figure 2.2	Epitope mapping of commercial antibodies reveals four distinct epitopes.	20
Figure 3.1	Introduction to myocilin structure and constructs.	26
Figure 3.2	Schematic workflow for mouse immunizations and <i>in-vitro</i> selection of candidate antibody sequences.	39
Figure 3.3	Testing of LZ-targeted scAbs.	41
Figure 3.4	Testing of CC-targeted scAbs.	43
Figure 3.5	Testing of IgGs targeting CC and LZ.	45
Figure 4.1	<i>Mm</i> OLF and <i>Hs</i> OLF share key structural features.	61
Figure 4.2	Biochemical environment of glaucoma-causing myocilin mutations.	62
Figure 4.3	Aggregates of MBP- <i>Mm</i> OLF isolated from <i>E. coli</i> are ThT-positive, a hallmark of amyloid.	65
Figure 4.4	Representative DSF thermal melting transitions for wild-type and mutant OLFs.	66
Figure 4.5	<i>Mm</i> OLF aggregation kinetics, and DMD/PRIME20 simulations of amyloidogenic mouse P3.	68
Figure 4.6	Representative simulation results and analysis of the dominant morphologies of human P1 and mouse P1 aggregates.	70
Figure 4.7	Simulation snapshots of mouse P1 aggregates.	70
Figure 4.8	Simulation snapshots of mouse P3 aggregates.	70
Figure 4.9	Atomic force micrographs of mouse and human OLF endpoint aggregate morphologies.	72

LIST OF SYMBOLS AND ABBREVIATIONS

Å	Angstrom
Ab	Antibody
BstNI	Restriction enzyme used for DNA fingerprinting
C	Celsius (unit of temperature)
CC	Coiled-coil (structural motif)
cDNA	Complementary DNA (synthesized from RNA template)
CDR	Complementary determining region (for antibody)
cgMD	Coarse-grain molecular dynamics
DMD	Dimensional Molecular Dynamics
DNA	Deoxyribonucleic acid
DSF	Differential scanning fluorimetry
<i>E. coli</i>	<i>Escherichia coli</i>
ELISA	Enzyme-linked immunosorbent assay
ER	Endoplasmic reticulum
HBS	HEPES-buffered saline
hCC	Coiled-coil portion of human myocilin (residues 33-111)
hCCLZ	Coiled-coil leucine-zipper of human myocilin (residues 69-185)
HEPES	4-(2-hydroxyethyl)-1-piperazineethanesulfonic acid
hLZ	Leucine-zipper portion of human myocilin (residues 112-185)
hNTD	N-terminal portion of human myocilin (residues 33-226)
HRP	Horseradish peroxidase
<i>Hs</i>	<i>Homo sapiens</i> (human)

hTM	Human trabecular meshwork
IACUC	Institutional animal care and use committee
IgG	Immunoglobulin G (antibody sub-type)
IOP	Interocular pressure
IPTG	Isopropyl β -D-1-thiogalactopyranoside
K	Kelvin (unit of temperature)
k_B	Boltzmann's constant
LZ	Leucine zipper (coiled-coil subtype)
mAb	Monoclonal antibody
MBP	Maltose-binding protein
mCCLZ	Coiled-coil leucine-zipper of mouse myocilin (residues 55-171)
mLZ	Leucine-zipper portion of mouse myocilin (residues 93-171)
<i>Ms</i>	<i>Mus musculus</i> (mouse)
MW	Molecular weight
NEI	National Eye Institute
NIH	National Institutes of Health
OD ₆₀₀	Optical density at 600 nm
OLF	Olfactomedin domain
pAb	Polyclonal antibody
PBS	phosphate-buffered saline
PCR	Polymerase chain reaction
PDB	Protein Data Bank
PEG	Polyethylene glycol
pI	Isoelectric point
r	Recombinant

rAb	Recombinant antibody
RGC	Retinal ganglion cell
RMSD	Root mean squared deviation
RNA	Ribonucleic acid
RPM	Rotations per minute
RRID	Research resource identifier
scAb	Single-chain antibody
scFv	Single-chain (antibody) variable fragment
SDM	Site-directed mutagenesis
SDS-PAGE	Sodium dodecyl sulfate poly-acrylamide gel electrophoresis
SEC	Size-exclusion chromatography
SEC-SAXS	Size-exclusion chromatography small angle X-ray scattering
SER-CAT	Southeast Regional Collaborative Access Team
T	Temperature
TEV	Tobacco etch virus protease
ThT	Thioflavin-T
TM	Trabecular meshwork
UV-Vis	ultraviolet-visible
VH	Variable heavy (antibody region)
VL	Variable light (antibody region)
ϵ_{HB}	Hydrogen bond energy
μ	Micro

SUMMARY

This thesis encompasses research towards the development of a new suite of conformation-specific antibodies targeting glaucoma-associated myocilin which bind both mouse and human myocilin, including the characterization of commercial myocilin antibodies, the development of antibodies specific to folded N-terminal myocilin domains, and the biophysical characterization of mouse myocilin olfactomedin domains.

Chapter 1 explores the importance of antibodies to myocilin research, offering a brief perspective on advances in antibody development methodology and biophysical characterization of myocilin which will drive our development of new, conformational antibodies to enable detection of folded (functional) and misfolded (disease-associated) myocilin in tissue samples, and identification of functional binding partners.

Chapter 2 details the testing of commercial myocilin antibodies against a variety of myocilin constructs to determine the epitopes recognized and conformational specificity. The antibodies recognize a variety of epitopes across the length of myocilin, binding both endogenous full-length myocilin and recombinant *E. coli*-expressed portions of human myocilin. However, they do not distinguish between folded and unfolded conformations of myocilin, demonstrating the need for further development of new, conformationally-specific myocilin antibodies.

Chapter 3 encompasses the generation and identification of conformationally-specific antibodies towards the N-terminal coiled-coil and leucine-zipper domains of myocilin. Antibody sequences from mice immunized with human and mouse N-terminal

myocilin were selected for high affinity through phage display, then produced as antibody fragments to characterize their target epitope and binding properties; the most promising candidates were selected for further characterization in the standard and widely-applicable immunoglobulin-G (IgG) format. Three conformational antibodies competent for immunoprecipitation of endogenous human myocilin were identified, two of which bind myocilin's leucine zipper and one which binds human coiled-coil. These antibodies will allow the broader glaucoma research community to track folded, functional N-terminal myocilin in mouse and human samples, assisting in identifying myocilin's elusive function.

Chapter 4 explores phenotypic differences between myocilin-based mouse models of glaucoma through the biophysical characterization of the olfactomedin domain of mouse myocilin, including crystal structure, melting temperatures of wild type and disease-associated mutants, aggregation propensity and simulated aggregation of amyloid-prone peptide within myocilin. Human and mouse myocilin olfactomedin domains display highly similar structure and biophysical properties, suggesting that that – barring differences in cellular toxicity of aggregates – mouse and human myocilin mutants should result in similar glaucoma phenotypes.

Chapter 5 provides perspective on future directions to apply the scientific developments detailed in the previous chapters to enhance our understanding of myocilin function and dysfunction towards a deeper molecular understanding of both healthy and glaucomatous eye physiology, and towards potential diagnostic and therapeutic applications.

CHAPTER 1. ANTIBODIES USED TO DETECT GLAUCOMA-ASSOCIATED MYOCILIN: MORE OR LESS THAN MEETS THE EYE?

Sections 1.1-1.5 were adapted from “A. C. Patterson-Orazem & R. L. Lieberman, Antibodies used to detect glaucoma-associated myocilin: more or less than meets the eye?” Manuscript under review at IOVS, February 2019; submitted draft is included here.

I contributed substantially to the writing of this manuscript and both designed and created the figure.

1.1 Abstract.

Antibodies are key reagents used in vision research, indeed across biomedical research, but they often do not reveal the whole story about a sample. It is important for researchers to be aware of aspects of antibodies that may affect or limit data interpretation. Federal agencies now require funded grants to demonstrate how they will authenticate reagents used. There is also a push for recombinant antibodies, enabled by technology awarded the 2018 Nobel Prize in Chemistry, which allow for thorough validation and a fixed DNA sequence. Here, we discuss how issues surrounding antibodies are pertinent to detecting myocilin, a protein found in trabecular meshwork and associated with hereditary glaucoma. Confirmation of myocilin expression in tissues and cell culture has been adopted as validation standard in trabecular meshwork research; thus, a discussion of antibody characteristics and fidelity is critical. Further, based on our basic structural understanding of myocilin architecture and its biophysical aggregation properties, we provide a wish list for the characteristics of next-generation antibody reagents for vision researchers. In the

long term, well characterized antibodies targeting myocilin will enable new insights into its function and involvement in glaucoma pathogenesis.

1.2 Antibodies: important research reagents invite closer scrutiny.

Antibodies, highly diverse proteins designed to bind specific targets and assist in combating infections, have been used in research to track specific target antigens across biomedical science since the mid-20th century [1]. Antibody biologics have also been transformative in their ability to treat a range of diseases [2]. At the protein level, antibodies consist of constant domains, similar across all antibodies, and variable domains whose diverse complementarity determining regions (CDRs) confer specificity to nearly any desired target antigen (Figure 1.1 A). Several subtypes of antibodies are commonly used in research; the most commonly used is immunoglobulin G (IgG). Antibodies used in research are designated polyclonal (pAb), monoclonal (mAb) or recombinant (rAb) based on their basic production method and composition. Traditional pAbs comprise a mixture of antibodies produced by the immune response of an animal to an antigen; the precise mixture varies over time and across individual animals. In contrast, mAbs consist of single antibody “clones” produced by a hybridoma fusion of spleen cells with an immortal myeloma cell line. Still tighter control of the antibody product can be achieved recombinantly by inserting a plasmid containing the DNA sequence encoding the desired antibody into a specialized cell line.

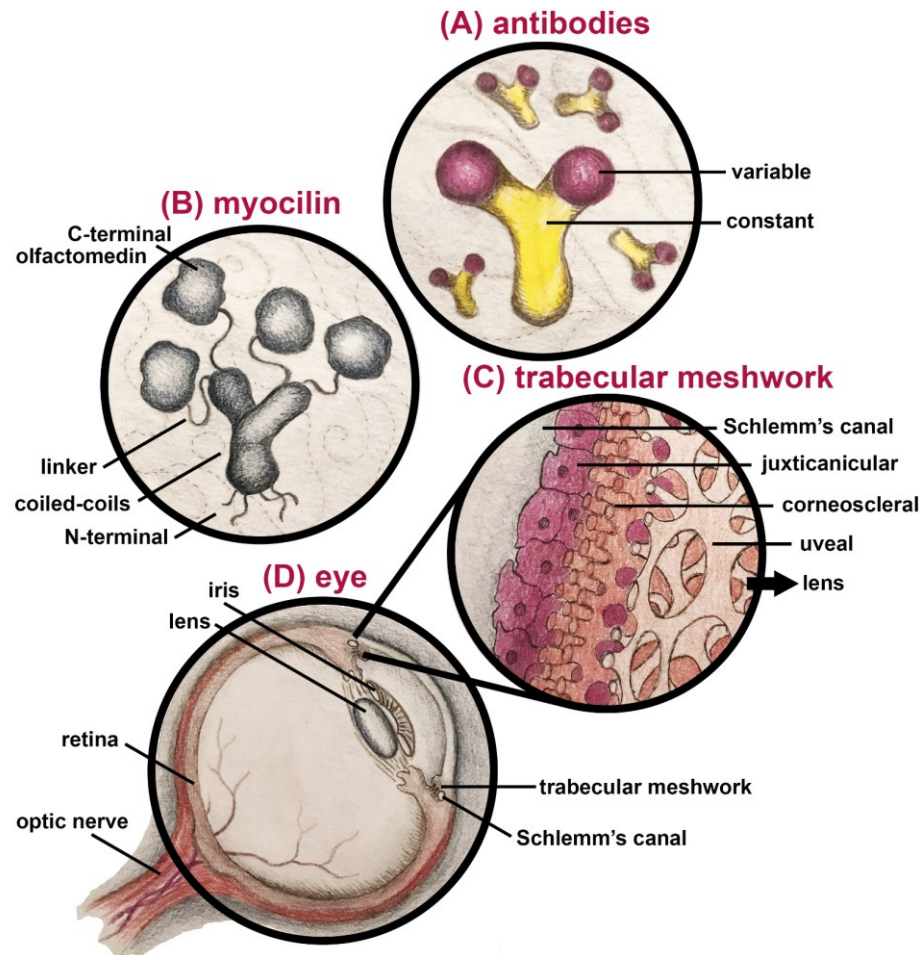


Figure 1.1 Artistic rendering (not to scale) of antibody, myocilin, trabecular meshwork and ocular structures. (A) Antibodies display a Y-shape, with constant domains at the base and variable domains at the end of the arms. (B) Myocilin forms a Y-shaped tetramer through its coiled-coil domains, which are attached to four C-terminal olfactomedin structural domains by linkers. (C) The trabecular meshwork is composed of three structurally distinct layers of cells leading away from the lens and towards the Schlemm's canal. (D) Basic anatomy of the eye.

Although antibodies are indispensable laboratory research reagents, in general they are not rigorously characterized. Natural variation in animal titers leads to cross-reactivity and batch-to-batch variability of polyclonal antibodies, and only a low percentage of serum antibodies bind the intended target [3]. Even antibodies subjected to antigen affinity purification include a variety of antibody isotypes that target multiple epitopes with a variety of affinities [4]. The use of hybridomas to express monoclonal antibodies overcomes some of this variability but, over time, spontaneous mutations introduce a new

source of variability [5]. Antibody fidelity has come under scrutiny after being identified as the likely culprit for irreproducible studies in cancer research, resulting in NIH and other funding bodies requiring more rigorous validation and documentation of research reagents used in the lab [3, 6].

1.3 Myocilin: associated with glaucoma yet functionally elusive.

As a case study for how antibodies might not necessarily reveal the whole story of a system, we consider the case of glaucoma-associated myocilin. Wild-type myocilin (Figure 1.1 B) is secreted at relatively high levels to the outflow-regulating trabecular meshwork (TM) extracellular matrix (Figure 1.1 C) within the eye (Figure 1.1 D) [7]; the TM is diseased in most forms of glaucoma. At the protein level, myocilin contains multiple distinct domains: a N-terminal signal sequence for secretion, a structured coiled-coil region for multimerization, a long ~60 amino acid linker and finally, at its C-terminus, a ~250 amino acid β -propeller [8] olfactomedin (OLF) domain. In its wild-type conformation, the coiled-coil region confers a Y-shaped tetrameric dimer-of-dimers architecture (Figure 1.1 B) [9]. If the explicit function of myocilin, or its binding partners, could be readily identified, it would have been already: despite 20 years of research effort in the community, there is no consensus regarding the role of myocilin in normal TM function.

By contrast, our understanding of the role of myocilin in glaucoma is relatively sophisticated. Genetic mutations in myocilin, particularly within its OLF domain, are causative for ocular hypertension that subsequently leads to early-onset glaucoma [10]. Myocilin-associated glaucoma is a remarkable example of an autosomal dominant Mendelian inheritance pattern, with affected families harboring unique mutations

throughout the world. Overall, non-synonymous mutations in myocilin are responsible for approximately 3-5% of the 70 million open angle glaucoma cases worldwide [11]. These changes in amino acid sequence result in reduced OLF stability [12], protein aggregation and intracellular accumulation in endoplasmic reticulum (ER) [13, 14]. An anomalous interaction with the ER-resident molecular chaperone Grp94 [15] leads to ER stress [15-21] and cell death [13, 17], hastening the hallmark glaucoma risk factor of increased intraocular pressure.

Myocilin is not a susceptibility gene for sporadic forms of glaucoma [22], as single nucleotide polymorphism variants are found in control populations. However, from a protein perspective, it is easy to envision broader relevance of wild-type myocilin to glaucoma pathogenesis. Most cells deal with proteostasis-related problems – imbalances in protein production, trafficking, and degradation – by undergoing apoptosis. However, long-lived cells such as TM cells [23] are programmed to avoid cell death [24] and, consequently, are particularly sensitive to the accumulation of misfolded proteins [25]. Toxicity to long-lived cells can be triggered by environmental factors as well as destabilizing mutations [26]. While wild-type OLF is thermally stable when folded [27], it possesses an intrinsic propensity to form a misfolded precipitate of a particular kind called amyloid that is common to many misfolding disorders [26]. *In vitro*, purified OLF remains unchanged when incubated at 37 °C for weeks at high concentration, but aggregation is readily initiated by adding mimics of glaucoma-associated environmental stressors – including low levels of acid (pH fluctuations), peroxide (oxidative stress), mechanical shear (rocking), and elevated temperature [28, 29]. Even though transgenic mice overexpressing wild-type myocilin do not develop glaucoma [30], and overexpression

alone cannot drive the association of normal myocilin with Grp94 [15], myocilin driven to misfold by impairing cellular glycosylation interacts with Grp94, culminating in accumulation and toxicity observed for disease-causing variants [15]. The misfolding susceptibility of wild-type myocilin is further supported by histopathological studies demonstrating its accumulation into punctate bodies in several forms of glaucoma [31]. Whether accumulated wild-type myocilin contributes to TM damage and outflow resistance remains unknown, but it is clear that our understanding of wild-type myocilin function and dysfunction remains blurry.

1.4 Myocilin antibodies: we don't know what we cannot detect.

Limitations of the reagents vision scientists have been using to detect myocilin in primary cell culture and tissue samples necessarily affect our contextual understanding of myocilin. For example, early in myocilin research there were reports of an apparent 66 kDa isoform, which was visible by Western blot using multiple myocilin antibodies [28, 32], but was not consistently observed. The jury is still out regarding this 66 kDa species, but it has not been confirmed as myocilin by mass spectrometry [29, 33], and may instead be a closely sequence-related protein [34] or serum albumin [29]. Myocilin protein expression in TM tissue and cell culture has been adopted as validation standard for the research community [7], elevating the need for transparent evaluation of antibody reagents available for the community to use.

Recently, we reported that commercially-available myocilin-directed antibodies now used in vision research target epitopes distributed across the protein [35], but do not differentiate among folded and misfolded states. Thus, at minimum, we are currently

missing information about whether myocilin is properly folded or whether it is adopting a disease state in a given sample. Even without destabilizing mutations, we know myocilin is very sensitive to its chemical environment. Beyond OLF being driven to misfold upon exposure to environmental stressors discussed above [36, 37], higher order oligomeric states beyond the native tetramer [9], mediated by disulfide bonds at the far N-terminal before the coiled-coils but after its signal sequence, have been detected in several experiments [38, 39]. Based on functional studies of olfactomedin family members, all of which contain eponymous OLF domains, post-translational modifications and protein-protein interactions are relevant to antibody detection. Cleavage of myocilin has been detected in mammalian cell culture [40], in line with a functional feature of other olfactomedin family members [41-43]. This feature has not been observed in tissue samples containing myocilin, however, likely because the antibodies used to stain for myocilin only detect one of the cleavage products. Other posttranslational modifications such as phosphorylation or glycosylation may also impede antibody binding, leading to the conclusion that myocilin is not present when it is simply not detectable. Additionally, other olfactomedin family members are known to function through complex macromolecular assemblies – such interactions between latrophilin OLF and a leucine-rich repeat protein which help modulate contacts between nerve cells [44]. On the other hand, the N-terminal coiled-coil domains of myocilin are “sticky” and predicted to interact with other extracellular matrix proteins [9]. These features of myocilin demand further elucidation, but also experimental consideration including, but not limited to, not relying on any single myocilin epitope to detect myocilin.

1.5 The future of myocilin-directed antibodies: our wish list.

To develop the most effective and reliable antibody reagents, consideration of the molecular properties of both antigens and antibodies is key. Understanding how an antibody interacts with its target antigen allows researchers to engineer antibodies for their own purposes, using a selection of epitopes enlightened by our structural understanding of the antigen. In addition, high-throughput and efficient *in-vitro* methods are now available to identify, design and optimize identified antibodies. Indeed, the 2018 Nobel Prize in Chemistry shared by Arnold, Smith, and Winter recognizes contributions to the directed evolution and phage display strategies, which represent landmark developments in protein engineering methodology directly applicable to antibodies.

Knowledge of myocilin structure and misfolding should facilitate the development of new antibody tools to study the protein in unprecedented detail. Ideal antibodies would harbor the following characteristics: (a) detect a variety of unique epitopes throughout the myocilin protein (b) be conformationally specific to a well-defined state of myocilin (folded, misfolded) (c) be recombinant to enable high quality control standards maintained by DNA sequencing [6] and not constitute a limited reagent, and (d) harbor cross-reactive for myocilin from multiple species, to streamline antibody use in the vision research community.

Beyond their application in validating primary human TM cells and tissues [7], a new suite of antibodies targeting deliberate molecular aspects of myocilin would reveal currently inaccessible specifics of myocilin in any given research sample of interest. Such information should lead to a better understanding of myocilin in normal physiology, as

well as the role of myocilin misfolding in normal eye aging, glaucoma, and possibly other scenarios in the body. In turn, the community will develop a more nuanced molecular picture of the TM, a complex and fascinating eye tissue that is regularly subjected to numerous chemical and biomechanical insults, unveiling new targets for anti-glaucoma therapies.

1.6 Contributions to the future of myocilin antibodies in research.

In this thesis, concerns regarding the quality and properties of existing myocilin antibodies are addressed first (Chapter 2) by identifying the target epitope and conformational specificity of four commercial myocilin antibodies used in the literature. This study provides a more thorough understanding of available myocilin antibodies such that researchers are aware of, including 1) the specific portion of myocilin detected, 2) potential non-specific binding interactions observed and 3) that none of these antibodies distinguish between folded and unfolded myocilin.

To afford new functionality in myocilin antibodies, conformational antibodies specific to folded N-terminal domains of myocilin were developed which are both recombinant and cross-reactive to human and mouse myocilin (Chapter 3). Recent advances in myocilin structure were combined with established antibody engineering technologies allowing *in-vitro* selection of antibody sequences from immunized mice which were then characterized for affinity to mouse and human myocilin, target epitope and conformational specificity. Three new conformational antibodies – two targeting mouse and human LZ, one targeting human CC – are competent for immunoprecipitation of folded endogenous TM-secreted myocilin from primary TM cells and are now available

to track the localization of folded N-terminal myocilin in tissue samples and for application to immunoprecipitation-shotgun proteomics approaches to identify functional myocilin binding partners.

Lastly, to inform the future development of C-terminal OLF-targeting antibodies to folded and misfolded mouse myocilin, and additionally to elucidate potential discrepancies in myocilin-based mouse models of glaucoma due to differences in the biophysical properties of mouse OLF, the structure and aggregation of mouse OLF was biophysically characterized (Chapter 4). Human and mouse OLF display largely similar properties in terms of structure, stability and aggregation which can be applied to generation of new antibodies specific only to folded or only to misfolded OLF and which can be used to further elucidate myocilin function and dysfunction in both humans and mouse models.

CHAPTER 2. **EPITOPE MAPPING OF COMMERCIAL ANTIBODIES THAT DETECT MYOCILIN.**

Adapted from “A.C. Patterson-Orazem, S. E. Hill, M. P. Fautsch & R. L. Lieberman; Epitope mapping of commercial antibodies that detect myocilin; Experimental Eye Research, 2018” [35]. Reproduced with permission from Elsevier.

I contributed to the work in this chapter in design, execution and analysis of antibody characterization experiments, design and execution of figures, and the writing and editing of the paper. S. E. Hill contributed N-terminal myocilin constructs, experimental design, figure design, and editing of the paper. M. P. Fautsch contributed antibodies developed in his lab and paper editing. R. L. Lieberman contributed to the experimental design, figure design, and paper crafting, writing and editing.

2.1 Abstract.

The presence of myocilin is often used in the process of validating trabecular meshwork (TM) cells and eye tissues, but the antibody reagents used for detection are poorly characterized. Indeed, for over a century, researchers have been using antibodies to track proteins of interest in a variety of biological contexts, but many antibodies remain ill-defined at the molecular level and in their target epitope. Such issues have prompted efforts from major funding agencies to validate reagents and combat reproducibility issues across biomedical sciences. Here we characterize the epitopes recognized by four commercial myocilin antibodies, aided by structurally and biochemically characterized myocilin fragments. All four antibodies recognize enriched myocilin secreted from human TM cell media. The detection of myocilin fragments by ELISA and Western blot reveal a variety of epitopes across the myocilin polypeptide chain. A more precise understanding of myocilin antibody targets, including conformational specificity, should aid the community

in standardizing protocols across laboratories and in turn, lead to a better understanding of eye physiology and disease.

2.2 Introduction.

Antibodies, protein molecules derived from the immune response in animals, are powerful scientific and therapeutic reagents due to their ability to strongly and specifically bind a desired target antigen. Polyclonal antibodies have been used for over a century and monoclonal antibodies from hybridoma cell lines for decades [45]. Although antibodies have been indispensable in addressing research questions across the biomedical sciences, these reagents are generally not rigorously characterized and are thus of variable quality [6, 46]. Polyclonal antibodies are notorious for problems with cross-reactivity and batch-to-batch variability due to natural variation in animal titers [47]. Only 0.5-5% of the antibodies in a polyclonal antibody sample bind their target protein [3, 4, 48], and even antibodies purified by using an antigen affinity step may include a variety of antibody isotypes targeting multiple epitopes with a variety of affinities [4]. The use of hybridomas to express monoclonal antibodies overcomes some of this variability [49]. However, over time, hybridomas can undergo mutations that alter specificity, thus introducing a new source of variability [5]. The rigorous validation of research reagents, including of antibodies, has become a high priority for NIH and other funding bodies due to the multitude of research studies that cannot be independently replicated [50].

Vision researchers who study trabecular meshwork (TM) rely on antibodies to detect myocilin, a protein secreted from TM cells [27, 51] and associated with heritable glaucoma [10]. Namely, myocilin expression is often used to distinguish TM cells and

tissues from other anterior segment regions [52, 53]. Our lab recently characterized the structural regions of myocilin (Figure 2.1 A, B) including the N-terminal coiled-coil domains by solution X-ray scattering, chemical crosslinking, and X-ray crystallography [9], and the C-terminal β -propeller olfactomedin domain (OLF) by X-ray crystallography [8]. Our studies reveal that myocilin is a Y-shaped dimer-of-dimers (Figure 2.1 B) [9]: the N-terminal coiled-coil region (CC, residues 33-111) forms a tetrameric stem with disulfides at Cys47 and Cys61, and the leucine-zipper (LZ, residues 112-185), a special type of coiled-coil, forms two dimeric arms, each of which is stabilized by a C-terminal disulfide bond [9]. Finally, a ~60 residue linker connects the LZ to two pairs of monomeric OLF domains (Figure 2.1 B).

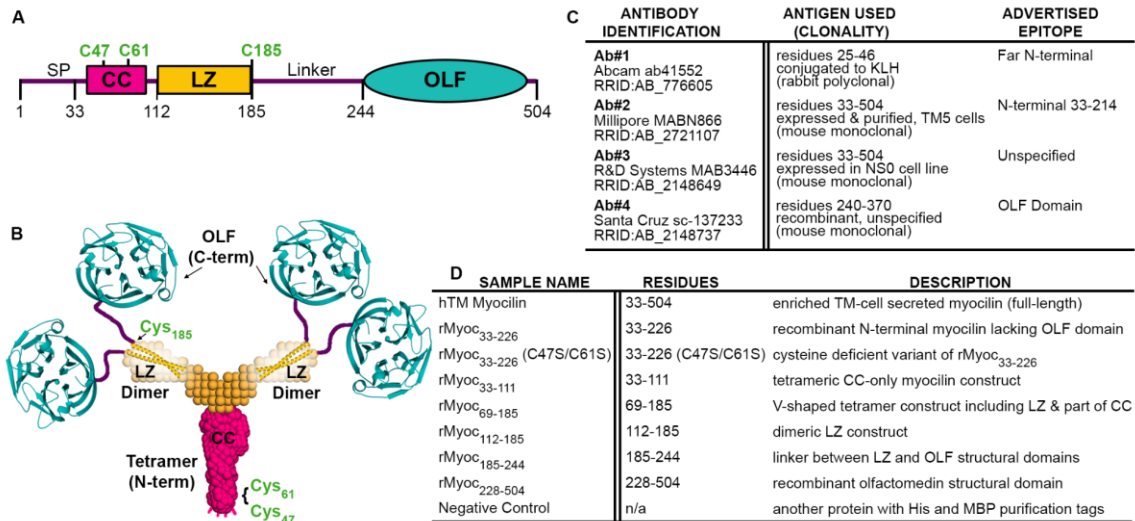


Figure 2.1 Introduction to myocilin structure, commercial antibodies, and protein constructs tested. (A) Gene structure depicting the domains of myocilin, including signal peptide (SP), location of key cysteine residues (C47, C61 and C185) and its coiled-coil (CC), leucine zipper (LZ) and olfactomedin (OLF) domains. (B) Myocilin quaternary structure based on solution X-ray scattering, X-ray crystallography and chemical cross-linking experiments. (C) Identifying information for commercial myocilin antibodies selected for this study, including antigen used for antibody development, clonality, and currently advertised epitope. (D) Myocilin constructs used in this study represent a combination of shorter and longer myocilin fragments. Each potential epitope for antibody recognition is represented at least twice.

Currently, there are several commercially-available antibodies against myocilin, but little is known about the epitope(s) recognized and specificity for detecting myocilin in the context of the (extra)cellular milieu. Knowledge of epitopes detected by these antibodies is important for several reasons. First, cleavage of myocilin has been reported in mammalian cells [40], like for other olfactomedin family members latrophilin [41] and gliomedin [42, 43] where such cleavage is functional. Using a single antibody reagent to detect myocilin may not fully describe its whereabouts or function, especially if cleavage is functional. Related, not all epitopes may be accessible to myocilin in a functional context, for example, in the case of complexation with a binding partner or upon post-translational modification. Second, the OLF domain of myocilin can be driven to misfold,

even in the absence of destabilizing disease-associated mutations, with selected environmental stressors [36, 37]. Indeed, the overall oligomeric state of myocilin may be sensitive to its environment, as higher-ordered states of myocilin, mediated by disulfide bonds, have been detected in several experiments [38, 39]. Detailed knowledge of epitope and conformational specificity of antibodies against myocilin could be transformative in our understanding of the functional role of myocilin processing, oligomerization, and misfolding.

Here, we took advantage of the well-defined domain constructs our lab used for structural studies of myocilin to characterize four anti-myocilin antibodies from commercial vendors (Ab#1-Ab#4). We describe the specific amino acid epitope within myocilin recognized by the four reagents, the conformational specificity of the respective epitope, and, to the extent possible, cross-reactivity (Figure 2.1 C). Ab#1 (Abcam Cat# ab41552, RRID:AB_776605) is a rabbit polyclonal antibody raised against recombinant myocilin residues 25-46 conjugated to keyhole limpet hemocyanin (KLH) and purified by protein A affinity chromatography. This antigen includes several residues within the signal peptide (residues 1-33), cleaved prior to secretion [54], and far N-terminal residues without predicted structure. Ab#2 (Millipore Cat# MABN866, RRID:AB_2721107) is a mouse monoclonal antibody raised against myocilin residues 33-504 produced in TM5 cells with C-terminal V5 and hexa-histidine (6x-His) tags. This antibody was purified from mouse hybridoma culture supernatant by protein A/G affinity chromatography and its epitope was previously localized to residues 33-214 within N-terminal myocilin [34]. Ab#3 (R&D Systems Cat# MAB3446, RRID:AB_2148649), is also an affinity-purified monoclonal mouse antibody, raised against recombinant myocilin (residues 33-504) that was produced

in the mouse myeloma cell line NS0. Finally, Ab#4 (Santa Cruz Biotechnology Cat# sc-137233, RRID:AB_2148737) is a monoclonal mouse antibody raised against recombinant myocilin residues 240-370 (cell line unspecified), a predominantly internal sequence of the C-terminal OLF structural domain, which spans residues 245-504 [8].

2.3 Materials and Methods.

2.3.1 Production of recombinant protein constructs.

Cell pastes containing recombinant proteins were gathered from S. E. Hill (all N-terminal myocilin constructs), D. J. E. Huard (control), I. M. Dominic (linker region) and A. C. Patterson-Orazem (C-terminal). Cell lysates and purified proteins were prepared by A. C. Patterson-Orazem. Recombinant myocilin subdomains (Figure 2.1 D) were cloned and expressed in *E. coli*, and purified as previously described [9, 55]. The linker region between the LZ and OLF domains (residues 185-244) was cloned into pET-28b vector with N-terminal 6x-His and S-tags (Genscript). The plasmid containing the linker region was transformed into *E. coli* BL21(DE3)pLysS, grown in Terrific Broth (Fisher) and expression was induced at $OD_{600}=0.8$ with 1 mM isopropyl- β -D-thiogalactopyranoside for 3 hours at 37 °C. Cell lysates were prepared by gently resuspending 0.5 g cells in 2.5 mL HBS (50 mM Hepes (pH 7.5), 200 mM NaCl, 10% glycerol) and 1/10 Complete EDTA-Free Protease Inhibitor Cocktail tablet (Roche), lysed by sonication, clarified by centrifugation at $\sim 20,000 \times g$.

2.3.2 *Enrichment of endogenous hTM-secreted myocilin.*

Enrichment of endogenous hTM-secreted myocilin was conducted by E. Nguyen. Human TM (hTM) cell medium was a kind gift from E. Snider and C. R. Ethier [56]. To enrich secreted myocilin from these samples, 20 mL of conditioned hTM medium was purified by heparin affinity (1-mL HiTrap Heparin HP, GE Healthcare) employing phosphate-buffered saline (10 mM Na₂HPO₄, 1.8 mM KH₂PO₄, 130 mM NaCl, 2.7 mM KCl, 10% glycerol, PBS) and an elution gradient to 1 M NaCl across 80 column volumes. Myocilin, detected by Western blot using the polyclonal anti-myocilin antibody N-15 (Table 3.1, RRID:AB_2148741, no longer commercially available), eluted at approximately 0.4 M NaCl. Corresponding fractions were pooled and concentrated approximately 36-fold using an Amicon Ultra centrifugal filter with 30 kDa molecular weight cut-off.

2.3.3 *Western blots and ELISA.*

Western blots and ELISA were conducted by A. C. Patterson-Orazem. Western blots were conducted on 25-100x dilutions of clarified *E. coli* cell lysates or 5 µL heparin-enriched hTM myocilin and transferred from SDS-PAGE to polyvinylidene difluoride membranes (Millipore) by standard electrophoresis methods. Primary antibodies were used at either 1 µg/mL or the manufacturer-recommended concentration, followed by 1:2000 dilution of secondary antibody: goat anti-mouse (Thermo Fisher Scientific Cat# 62-6520, RRID:AB_2533947) or goat anti-rabbit (KPL, Cat# 074-1506, RRID:AB_2721169). Blots were imaged using an Amersham Imager A600 (GE Healthcare). Western blot results represent at least two biological replicates per antibody tested. For a given antibody tested

in ELISA, triplicates of all proteins samples were immobilized on one medium-binding 96-well Costar plates (Corning) by overnight 4 °C incubation of 50 µL/well 2x diluted cell lysate in HBS (with non-myocilin cell lysate as negative control), or 1-5 µM purified protein [9, 55], employing antigen-free wells as a control. Samples were treated with serial dilutions of primary antibody (starting from 5 µg/mL) and 1:2000 dilutions of appropriate secondary antibody. Absorbance of HCl-quenched 3,3',5,5'-tetramethylbenzidine (TMB, 450 nm) was measured using a BioTek Synergy 2 plate reader. ELISA results are an average of at least two biological replicates per antibody tested. Absorbance values for each ELISA plate were normalized to the maximum absorbance within that plate, then multiple, normalized plates were averaged and plotted in Origin Professional 2016. Error bars represent standard deviation across all samples.

2.4 Results and Discussion.

Ab#1 primarily recognizes the far N-terminal residues of myocilin (residues 33-46), but a secondary epitope and other non-specific bands are also detected. In Western blot, Ab#1 recognizes recombinant human myocilin comprising residues 33-226 (rMyoc₃₃₋₂₂₆, Figure 2.2 A) and secreted full-length myocilin from hTM media (Figure 2.2 B). Over-exposure of Western blots results in detection of endogenous proteins from the *E. coli* cell lysate (not shown) as well as weak bands ~70 and 100 kDa in the hTM sample (Figure 2.2 B). A “66 kDa myocilin isoform” has been detected by multiple myocilin antibodies [27, 28] but has fallen under suspicion due to poor reproducibility. The 66 kDa band has yet to be confirmed as myocilin by mass spectrometry [29, 33], but it has been speculated that this band may instead comprise sequence-related proteins [34] or albumin [29]. In Western blot (Figure 2A) and ELISA (Figure 2.2 C), Ab#1 also recognizes the smaller far-N-

terminal tetrameric construct composed of residues 33-111 (rMyoc₃₃₋₁₁₁). Thus, of the residues within the antigen for Ab#1 (25-46), residues 33-46 are sufficient for detecting larger myocilin constructs containing these residues. Ab#1 also weakly recognizes the construct composed of residues 69-185 (rMyoc₆₉₋₁₈₅) in ELISA (Figure 2.2 C) and in over-exposed Western blots (not shown). This could arise from two segments within this construct (residues 102-109 and 158-168), which share 75 and 81% sequence similarity, respectively, with the antigen. This weak interaction likely benefits from the increased avidity of tetrameric rMyoc₆₉₋₁₈₅ in ELISA.

Ab#2 recognizes an epitope within rMyoc₃₃₋₁₁₁, and its detection is sensitive to the presence of disulfide bonds formed by C47 and C61. In Western blot, Ab#2 detects *E. coli* lysates containing rMyoc₃₃₋₂₂₆ and rMyoc₃₃₋₁₁₁ (Figure 2.2 D) as well as secreted hTM myocilin (Figure 2.2 E). In initial ELISA experiments, Ab#2 detected rMyoc₃₃₋₂₂₆ and, to a lesser extent, rMyoc₃₃₋₁₁₁ (not shown). These results were reproduced in a follow-up ELISA experiment conducted using equimolar concentrations of purified recombinant rMyoc₃₃₋₂₂₆ and rMyoc₃₃₋₁₁₁ (Figure 2.2 F). To test the contribution of disulfide bond formation to the recognized epitope given previously characterized variations in *E. coli* disulfide bonding for rMyoc₃₃₋₂₂₆ and rMyoc₃₃₋₁₁₁, ELISA was also conducted on the purified disulfide-disrupted variant rMyoc₃₃₋₂₂₆ C47S/C61S (rMyoc₃₃₋₂₂₆ (C47S/C61S)) [9], revealing apparent reduced affinity when compared to wild-type rMyoc₃₃₋₂₂₆.

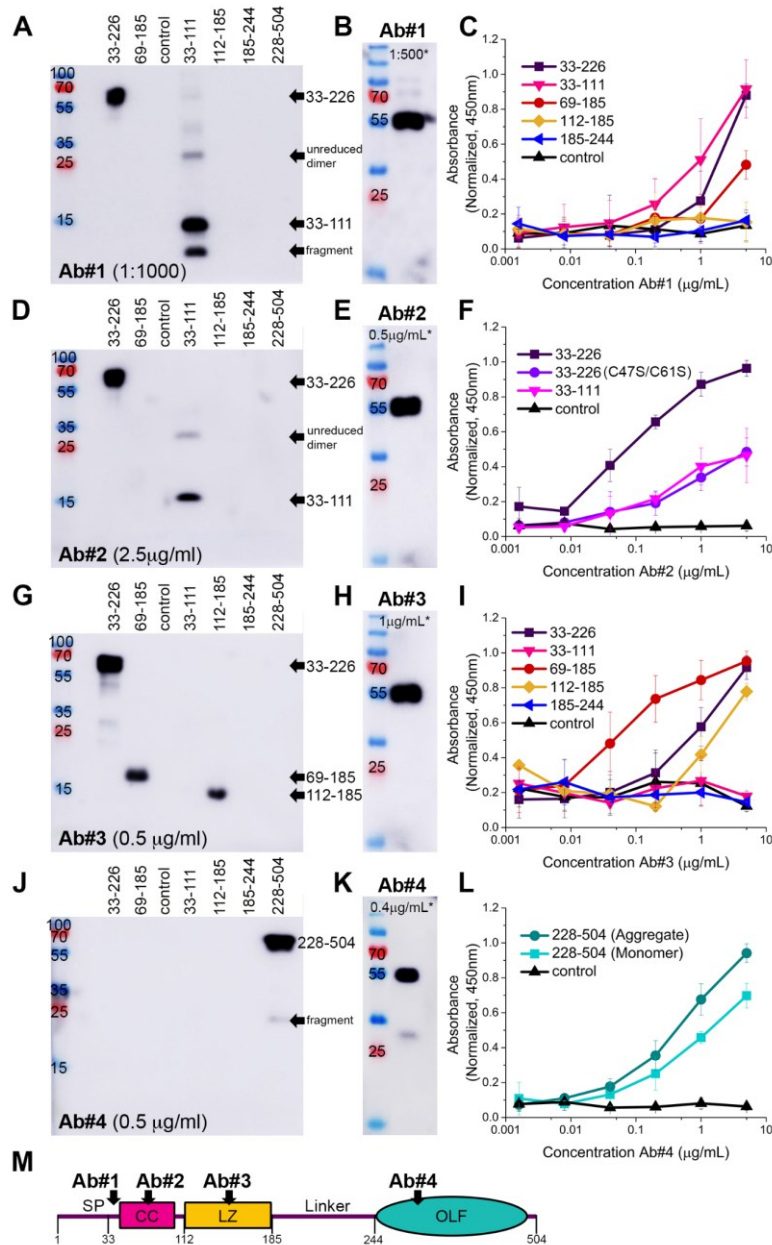


Figure 2.2 Epitope mapping of commercial antibodies reveals four distinct epitopes. (A,D,G,J) Western blots demonstrate binding of antibodies against cell lysates containing recombinant myocilin fragments under denaturing conditions. Manufacturers' recommended primary antibody concentrations are indicated with an asterisk, and standards (PageRuler™ Plus, Thermo Scientific) are indicated in kilodaltons. (B,E,H,K) All antibodies tested recognize myocilin enriched from hTM cell-conditioned medium in Western blots. ELISA conducted against clarified cell lysates (C,I) and purified protein (F,L) demonstrate antibody binding to recombinant myocilin constructs in native conditions. (M) Schematic representation of target regions of the four commercial antibodies on myocilin.

Ab#3 recognizes the LZ region (residues 112-185) of myocilin. This antibody recognized rMyoc₃₃₋₂₂₆ (Figure 2.2 G) and hTM-secreted full-length myocilin (Figure 2.2 H) in Western blots, and rMyoc₃₃₋₂₂₆ in ELISA (Figure 2.2 I). Both Western blot and ELISA yield robust recognition of smaller N-terminal constructs, corresponding to residues 69-185 (rMyoc₆₉₋₁₈₅) and the LZ-containing subdomain 112-185 (rMyoc₁₁₂₋₁₈₅).

Ab#4 recognizes the myocilin OLF domain, as designed (Figure 2.2 C) but does not distinguish between natively folded and misfolded states. In Western blot, Ab#4 detects the purified OLF domain (Figure 2.2 J) as well as full-length secreted hTM myocilin (Figure 2.2 K). In ELISA (Figure 2.2 L), Ab#4 recognizes both folded OLF monomer and amyloid-like misfolded OLF comprising residues 228-504 (rMyoc₂₂₈₋₅₀₄), expressed and purified from *E. coli* as a maltose-binding protein (MBP) fusion [37]. Notably, we previously showed that the polyclonal precursor to this antibody (Santa Cruz H-130, no longer available) recognizes related domains from other olfactomedin family members [57], which share a conserved interior [8], suggesting that this antibody may be similarly non-selective.

In sum, our study reveals that the commercial myocilin antibodies tested recognize amino acid sequence-derived epitopes across myocilin structural domains (Figure 2.2 M), including far N-terminal (residues 25-46, Ab#1), CC (residues 33-111, Ab#2), LZ (residues 112-185, Ab#3) and C-terminal OLF domain (residues 240-370, Ab#4). All four antibodies recognize myocilin secreted from hTM media; however, Ab#1 also exhibits non-specific binding to other proteins at high exposures. The diversity of epitopes revealed by our *in vitro* ELISA and Western blot experiments suggest that biological insights may be gleaned from employing different antibodies to detect the same myocilin-containing tissue sample.

Such comparative tissue studies could assess the accessibility of a given epitope, tying into protein function, processing, or misfolding. Conversely, by using a single myocilin antibody to a given epitope, functionally relevant myocilin fragments may remain undetected or non-myocilin contaminants may be inadvertently detected. Our library of recombinant myocilin constructs will be useful to monitor changes in epitope recognition by myocilin antibodies over time and from lot-to-lot. Finally, beyond the currently available myocilin antibodies, we anticipate that the TM research community may benefit from recombinant antibodies [6]. Such antibodies can be held to higher quality control standards due to gene sequencing, and can be tailored by engineering for sensitivity, selectivity, and even bifunctionality.

CHAPTER 3. RECOMBINANT ANTIBODIES OFFER CONFORMATION-SPECIFIC TARGETING OF THE N- TERMINAL COILED-COILS OF GLAUCOMA-ASSOCIATED MYOCILIN.

Adapted from “A. C. Patterson-Orazem, A. Qerqez, S. E. Hill, Y. Ku, J. A. Maynard & R. L. Lieberman, Recombinant antibodies offer conformation-specific targeting of the N-terminal coiled-coils of glaucoma-associated myocilin,” a manuscript in preparation for submission.

I contributed to experimental design for antibody development and characterization, and conducted experiments including epitope mapping of candidate antibodies, dot blots and Western blots to assess conformational specificity, dot blots against enriched endogenous myocilin, immunoprecipitation of endogenous myocilin and IgG thermal stability measurements. I additionally designed and executed figures (for Figure 2, execution only) and contributed to the organization, writing and editing of the manuscript.

A. Qerqez contributed to antibody-directed experimental design, phage display, scAb and IgG expression and purification, ELISA experiments with purified scAbs and IgGs, and designed Figure 2. S. E. Hill provided N-terminal myocilin constructs, prepared proteins for mouse immunizations, and assisted in myocilin-directed experimental design. Y. Ku conducted replicate western blot, dot blot and immunoprecipitation experiments, Image J analyses for heat maps, and assisted in manuscript editing. J. A. Maynard contributed antibody-directed experimental design; R. L. Lieberman contributed overall experimental design and to editing this manuscript.

3.1 Abstract.

Recombinant antibodies with well-characterized epitopes and known conformational specificity are key reagents for robust interpretation and reproducibility of immunoassays across biomedical research. For glaucoma-associated myocilin, recent developments in our understanding of its unique branched architecture and aggregation indicate that epitopes recognized by myocilin-directed antibodies used currently in the field do not differentiate among numerous disease-associated states of the protein, limiting

insight. Here, we used protein engineering methods to develop new recombinant antibodies that detect the N-terminal coiled-coil and leucine-zipper structural domains of myocilin. We identified two leucine-zipper-directed antibodies that detect human and mouse myocilin. Both are competent for immunoprecipitation of secreted myocilin from spent media of primary human trabecular meshwork cells. One of these antibodies preferentially detects folded myocilin and thus is conformationally selective. A third antibody, directed to the human coiled-coil, is conformationally selective and competent for immunoprecipitation of endogenous myocilin. The availability of these new antibodies offers unique opportunities to visualize and characterize murine and human myocilin in unprecedented detail.

3.2 Introduction.

Antibodies are indispensable and ubiquitous tools for targeting a specific antigen across biomedical research. Advances in antibody engineering methodology [58] and concerns over reproducibility of antibody reagents [3] are fueling a movement towards highly characterized recombinant antibodies [6] which avoid the batch-to-batch variability of traditional polyclonal antibodies [47] and the genetic drift of traditional monoclonal antibodies [5]. These new antibodies can be designed with the structure, function and dysfunction of their targets in mind – including conformationally-specific antibodies targeted, for example, to amyloid [59] and other misfolded proteins [60] with uses ranging from structural and mechanistic characterization to potential therapeutic applications.

Myocilin is a multi-domain protein (Figure 3.1 A) highly expressed in the trabecular meshwork (TM) [27, 51], an ocular tissue in the anterior segment involved in

the filtration of aqueous humor and therefore the regulation of intraocular pressure (IOP), [52] the causal risk factor for vision loss in glaucoma, a disease estimated to affect ~65 million people worldwide by 2020 [61]. Destabilizing mutations in myocilin [10, 62] result in hereditary primary open-angle glaucoma. Mutant myocilin aggregates and accumulates intracellularly, leading to cell death, reduced TM outflow, hastening the timeline for glaucoma-associated IOP elevation and vision loss [63]. While the biological function of myocilin in TM still remains elusive, increased myocilin expression due to glaucoma-relevant stressors such as steroid treatment [51] and mechanical stretching [64] suggest broad relevance of myocilin to the TM and ocular pressure homeostasis.

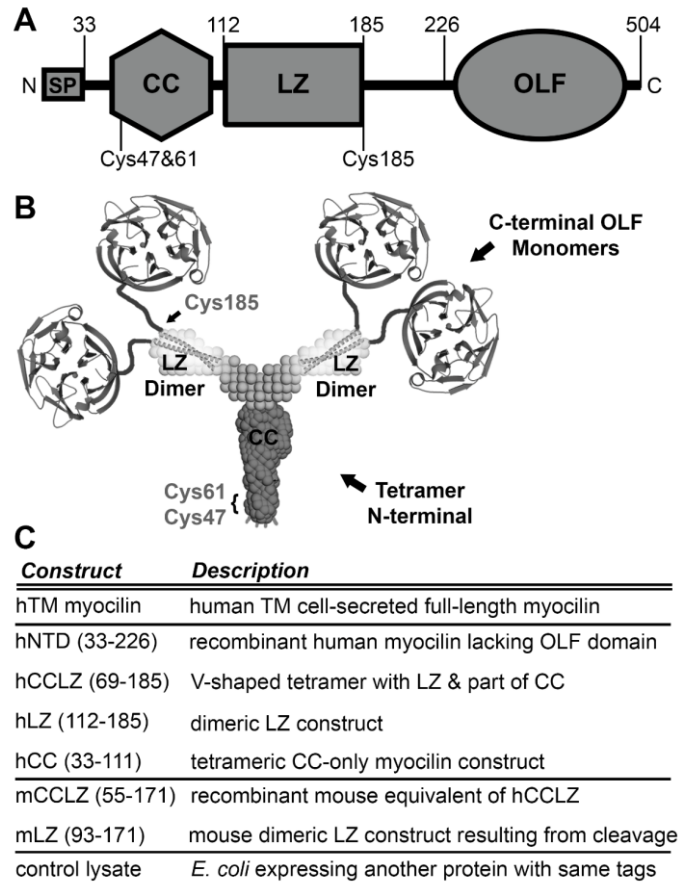


Figure 3.1 Introduction to myocilin structure and constructs. A. Myocilin gene sequence includes a N-terminal signal peptide (SP), coiled-coil (CC) and leucine-zipper (LZ) structural domains and a C-terminal olfactomedin domain (OLF). B. Model of myocilin architecture based on SEC-SAXS, X-ray crystallography and chemical crosslinking. C. Table of myocilin constructs used in this paper. Amino acids for recombinant proteins shown in parenthesis.

Myocilin antibodies are used to track the protein in a variety of human samples and animal models, as well as validate TM cell lines [65]. Recently, we tested the commercial myocilin antibodies recommended by the TM research community [65] to clarify the specific epitopes targeted [35]. These antibodies recognized several epitopes across the myocilin protein, but were unable to distinguish between folded and misfolded forms, which are disease-relevant [35]. Thus, antibodies used to study myocilin are contributing to the still-blurry functional picture. Lack of conformational selectivity limits insight

gained from TM studies as myocilin is prone both to amyloid aggregation [36, 37] and proteolysis [66, 67].

Here we leverage our understanding of myocilin structure to develop new antibodies. We targeted the N-terminal tetrameric coiled-coil domain and dimeric leucine-zipper domain (Figure 3.1 B). Our new antibodies are recombinant, which allows for DNA sequence confirmation, unlimited production via cell culture, and facile conversion to other formats (IgG, Fab). They are also cross-reactive, binding human and mouse myocilin (~80% sequence identity) to streamline lab reagents. Finally, their sensitivity to the conformational state of myocilin is well-defined.

Materials and Methods.

3.2.1 Commercial Antibodies Used

Table 3.1 Commercial antibodies used in antibody development and testing.

Antibody	Identification	Epitope & Clonality
Commercial anti-LZ	R&D Systems Cat# MAB3446 RRID: AB_2148649	human myocilin LZ within residues 112-185 (monoclonal)
Mouse anti-His <i>4A12E4</i>	Fisher Scientific Cat #37-2900 RRID: AB_2533309	Hexahistidine Tag (monoclonal)
M13 <i>RL-ph1</i>*HRP	Santa Cruz Cat #sc-53004 RRID: AB_673750	M13 phage coat protein (monoclonal*HRP)
Mouse anti-Myc <i>9E10</i>	Santa Cruz Cat #sc-40 RRID:AB_627268	human C-terminal Myc residues 408-439 (monoclonal)
Goat anti-mouse*HRP	Thermo Fisher Cat# 62-6520 RRID: AB_2533947	mouse IgG (polyclonal*HRP)
Goat anti-human κ*HRP	Southern Biotek Cat# 2060-05 RRID: AB_619883	human kappa light chain (polyclonal*HRP)

Antibody conjugation indicated by *; clone designations are italicized.

3.2.2 Protein expression and purification: myocilin

N-terminal myocilin constructs, designed by S. E. Hill, were expressed and purified by S. E. Hill and A. C. Patterson-Orazem. Clarified cell lysates were produced by A. C. Patterson-Orazem and Y. Ku. N-terminal myocilin fragments (see Figure 3.1 C) were expressed in *E. coli* BL21-DE3-pLysS using pET-30 XaLIC [9] or in pMAL (hNTD, comprising residues 33-226, only) [35] vectors. Proteins were purified as described previously [9] by nickel affinity chromatography followed by size-exclusion on AKTA Pure or Purifier (GE). For immunization and panning, expression tags were cleaved using Factor-Xa (New England Biolabs) and purified proteins isolated by heparin affinity and size-exclusion chromatography. Protein concentrations were determined by absorbance at 280nm using ExPaSy-predicted extinction coefficients, as described previously [9].

Our intent was to immunize mice with hCCLZ (comprising residues 69-198) and boost with the orthologous mouse construct mCCLZ (residues 55-171). However, post immunization, we learned that during purification our mCCLZ construct was cleaved by Factor Xa at a fortuitous site (TLGR₉₂) [9]. Thus, the actual immunogen used was mLZ (residues 93-171). Similar secondary sites have been reported in literature exploring Factor-Xa specificity [68, 69].

For dot blot characterization, clarified cell lysates were prepared by sonicating 0.2g cell paste in 1 mL buffer (50mM HEPES (pH 7.5), 200mM NaCl, 10% glycerol) until clarified, then removing the insoluble fractions by centrifugation at 17,000 x g [35]. Cell lysates used for the negative control were derived from BL21-DE3-pLysS cells expressing a non-myocilin protein with both tags present in the N-terminal constructs used here. Full-

length endogenous myocilin was enriched from spent hTM medium by heparin affinity, also as described previously [35].

3.2.3 Mouse Immunization & RT PCR

Immunizations were conducted by J.M. Hyun, RNA extraction and cDNA storage by A. Qerqez (Maynard Lab, U. T. Austin). All protocols were approved by the University of Texas at Austin IACUC, and all mice were handled in accordance with IACUC guidelines. Three 6 week old BALB/c mice were immunized subcutaneously with 5mg of hCCLZ using Freund's adjuvant. Four weeks later, the mice were bled through a tail vein and boosted subcutaneously with 5 mg of mLZ using incomplete Freund's adjuvant. Mice were then sacrificed and their spleens were harvested and stored in 1mL RNAlater solution at -80°C. Blood collected was used in an ELISA to determine the serum antibody titers against hCCLZ and mLZ. Total RNA was extracted from frozen spleens with TRIzol (Invitrogen) and the PureLink RNA kit (Invitrogen) according to the manufacturers' instructions. Concentration of RNA was determined using a NanoDrop2000 (Thermo Scientific). RNA was stored at -80°C until further use. For first strand cDNA synthesis, a total of 500 ng of RNA was used. First strand cDNA synthesis was performed using the SuperScript IV Transcriptase (Invitrogen) kit following the manufacturer's instructions. cDNA was then stored at -20°C until further use.

3.2.4 Phage Display Library Construction

Phage display libraries were constructed by A. Qerqez, Maynard Lab at U. T. Austin. The cDNA was then used to generate variable heavy (V_H) and variable light (V_L) chain repertoires for each mouse using the primer sets and PCR conditions described

previously [70]. The V_H and V_L fragments were then used as a template (30 ng of each) for the overlapped PCR [70] to generate V_L-linker-V_H fragments (scFv). The overlapped PCR fragments (about 10 µg per mouse scFv) were gel purified using Zymoclean Gel DNA Recovery kit and then digested using SfiI restriction enzyme (New England BioLabs) overnight at 50°C. About 50 µg of freshly purified pMopac24 vector was also digested overnight using SfiI at 50°C. The digests were gel purified and cleaned using Zymoclean Gel DNA Recovery kit. Ligation between the two fragments was performed using T4 DNA ligase (New England BioLabs) (400 - 500 µL ligations per mouse) and was left at 16°C overnight. The next morning (after 16-18 hours), the ligation was heat inactivated for 20 minutes at 65°C and all ligations were pooled together and concentrated using n-butanol by tenfold. The concentrated ligation was then desalted using nitrocellulose membranes for two hours before electroporating in freshly prepared XL1Blue electrocompetent cells (30 to 40 electroporations). The electroporations were recovered in warm SOC medium for 1 hour before plating on medium 2XYT agar plate with 1% glucose and 100 µg/mL ampicillin plates. An aliquot was 10-fold serially diluted and plated to count library size. Plates are left overnight at room temperature and then scraped the next morning into 2XYT medium with 1% glucose. The scraped bacteria was pooled to form the master library, then frozen down in 1 mL aliquots at -80°C at an OD₆₀₀ of 5.

3.2.5 Phage Production, Purification, & Panning

Phage display was conducted by A. Qerqez (Maynard Lab, U. T. Austin). One aliquot from the library was thawed and used to inoculate a 30 mL 2XYT culture supplemented with 1% glucose and 100 µg/mL ampicillin at a starting OD₆₀₀ of 0.08-0.1.

The flask labeled “input” was then grown at 37°C shaking at 225 RPM for 2-3 hours until the OD₆₀₀ was between 0.4 and 0.6. 1mM final IPTG concentrated as well as M13KO7 helper phage at a multiplicity of 20. The flask was allowed to shake an additional 20 to 30 minutes at 37°C and then the temperature is switched to 25°C. Three hours after adding the helper phage, the culture was supplemented with 25 ug/mL kanamycin and allowed to shake overnight at 25°C. Phage were then purified from the supernatant of the culture using 1/5th volume of precipitation solution (2.5M NaCl and 20% PEG-8000). Phage concentration was assessed using phage forming units (pfu) with serially diluted phage added to mid-log phase XL1Blue cells. These dilutions were then plated on 2XYT agar plate with 1% glucose and 100 ug/mL ampicillin.

The first round of panning was performed using mouse anti-Myc 9E10 (Table 3.1, RRID: AB_627268) as bait to remove any clones with possible stop codons. The subsequent rounds were panned against hCCLZ or mLZ. For panning, the protein was coated on eight ELISA plate wells (Costar) and allowed to incubate at 2 - 4 ug/mL overnight at 4°C. The following day the plates were blocked using 5% milk + 1x PBST for 1 hour. Another non-coated plate was blocked with 5% milk (8 wells). Once the phage was purified from the culture’s supernatant, it was resuspended in a 1:1 ratio in 10% milk and then aliquoted across 8 wells of non-coated but blocked plate and allowed to incubate at room temperature on a rocker for 1 hour. This ensures that any milk binding proteins are removed and do not propagate during the panning. The milk and phage mixture is then added to the antigen bound plate and allowed to incubate for 2 hours. Finally, the wells are washed rigorously using sterile PBS plus 0.1% Tween-20 and bound phage are eluted using 0.1 M glycine at pH of 2.5, pooled, and then neutralized with 24 uLs of 2 M Tris-HCl (pH

of 8.0). Half of the output phages were added to mid-log phase XL1Blue culture and incubated for 30 minutes shaking at 37°C. The input growth process was repeated for subsequent rounds of panning until a general consensus of scFv variants was reached.

Eight ELISA plate wells (Costar) were coated with 50 uLs of 2 ug/mL anti-Myc (9E10 from BioXCell) monoclonal antibody, hCCLZ protein, or mLZ protein overnight at 4°C. The library is first panned against anti-Myc antibody to ensure that only full length scFvs are screened for in subsequent rounds of panning. Panning was then performed on the hCCLZ and mLZ antigen to ensure the generation of cross reactive scFv sequences. Sequence diversity was monitored throughout all the steps by colony PCR and BstNI fingerprinting as well as Sanger Sequencing.

Monoclonal phage ELISAs were performed on unique clones with interesting complementary determining regions (CDRs). Single clone cultures (2 mL) grown up an OD₆₀₀ of 0.5 in 2XYT media supplemented with 1% glucose and 100 ug/mL ampicillin. Single cultures were then induced with 1 mM IPTG and helper phage at a multiplicity of 20 and were left shaking at 37°C for thirty minutes before switching to room temperature shaking. After three hours of shaking at room temperature, 50 ug/mL kanamycin was added to the cultures and they were left to shake overnight. ELISA plates were coated with 2 ug/mL antigen (hCCLZ or mLZ) diluted in PBS overnight at 4°C. The next day the phage was harvested as described previously and used as a primary stain in an ELISA. Phage binding to the antigen was detected using a 1:2000 dilution of mouse anti-M13*HRP antibody (Table 3.1, RRID: AB_673750) in 1x PBS, 0.1% Tween-20, 5% milk.

3.2.6 *Protein expression and purification: antibodies*

Expression and purification of scAbs were performed by A. Qerqez (primarily) and A. C. Patterson-Orazem (for a few follow-up experiments). All IgG expression and purification were performed by A. Qerqez (Maynard Lab, U. T. Austin.)

3.2.6.1 Single chain antibodies (scAbs)

To produce soluble scAbs (V_L-linker-V_H- human constant κ), the pMopac24 scFvs and pMopac54 vector were minipreped and digested with SfiI (New England BioLabs) for 3 hours at 50°C. The inserts from the digest were then ligated into digested pMopac54 vector, which includes the human constant κ sequence and a 12X his tag. The ligation was then electroporated into BL21 (DE3) competent cells (New England BioLabs) and plated on 2XYT agar plates supplemented with 100 ug/mL ampicillin and 1% glucose. Single colonies were sequence verified and inoculated into a 3 mL culture of TB supplemented with 100 ug/mL ampicillin and 1% glucose and were allowed to shake at 37°C until an OD600 of 5. Smaller cultures were then used to reinoculate a larger 250 mL culture of TB in 1 L flasks. Large cultures were supplemented with 1% glucose and 100 ug/mL ampicillin and were allowed to shake overnight at 37°C and 225 rpm. The next day the large cultures are harvested by centrifugation at 5000 rpm for ten minutes. The pellets are resuspended in fresh media and returned to flasks with fresh 250 mL TB supplemented with 100 ug/mL ampicillin. They were allowed to shake one hour at 25°C and were then induced with a final concentration of 1mM IPTG. They were allowed to shake for an additional five hours before the cells were harvested again. Osmotic shock was performed as previously described [71]. ScAbs were then purified using IMAC resin followed by size exclusion

chromatography with a Superdex 75 column on FPLC (GE Healthcare). Protein concentrations were measured using Nanodrop 200 and purity was assessed by SDS-PAGE on a 4-20% gel (Bio-Rad).

3.2.6.2 Immunoglobulin G (IgGs)

scFvs were generated into full length chimeric human IgG1 antibodies by cloning the V_H and V_L domains with primers into Ig κ -Abvec and IgG-Abvec vectors as described previously [72]. IgGs were produced in CHO-K1 cells using 1:1 ratio of both heavy and light chain vectors and lipofectamine 2000 (Invitrogen). Transfection was performed following the manufacturer's protocol using DMEM supplemented with 10% low IgG FBS. Media was collected from T-150 transfections and replaced every two days over the course of an entire week. Media was then pooled and applied to a HiTrap protein A column (GE Healthcare) and eluted from the column using 0.1 M glycine (pH = 2.5). Purity of proteins was assessed by SDS-PAGE gels 4-20% (Bio-Rad) and concentration was measured using Nanodrop 2000.

3.2.7 *ELISA & Competition ELISA*

ELISA and competition ELISA were performed by A. Qerqez (Maynard Lab at U. T. Austin). For all proteins, ELISA was performed by coating high binding plates (Corning 9018) with 1 ug/mL mLZ, hCCLZ, or hCC overnight in PBS at 4°C. The following day plates were blocked with PBS supplemented with 5% milk and 0.1% Tween-20 (milk solution) for one hour at room temperature. ScAbs or IgGs were then serially diluted (1:5) in milk solution to the blocked plates. Secondaries were then added at 1:1000 dilution of either goat anti-human κ *HRP for scAbs or goat anti-human IgG Fc HRP for full length

antibodies. ELISAs were then developed using TMB solution (Thermo Scientific Pierce) and then quenched with 1 N HCl.

For competition ELISA, the scAbs (starting concentration of 50 ug/mL) were serially diluted in the presence of 1:1000-1:3000 dilution of scFv variant in the presence of milk solution. The phage mixture concentration remained constant across all wells. Competition of phage and scAbs was then detected using 1:2000 dilution of mouse anti M13 HRP antibody (Table 3.1, RRID: AB_673750) in milk solution. EC50s for competition were then calculated using GraphPad prism and compared to controls. Absorbance was measured using a plate reader at wavelength of 450nm.

3.2.8 Dot Blots and Western Blots

Dot and western blots were conducted by A. C. Patterson-Orazem and Y. Ku using protocols previously described in detail [35]. Briefly, protein samples were immobilized on methanol-activated polyvinylidene difluoride membranes (Millipore) by electrophoresis for Western blots and by direct deposition of 2 μ L sample per dot for dot blots. Membranes were blocked overnight in 2% milk in PBS supplemented with 0.5% TWEEN-20, then probed with primary antibodies. Custom scAbs were tested at 1 μ g/mL; IgGs were tested at 0.5 μ g/mL to account for bivalency. Protein expression in cell lysates was confirmed using 1:1000 mouse anti-His (Table 3.1, RRID: AB_2533947). Commercial anti-LZ antibody (RRID: AB_2148649) was used as a positive control. Custom scAbs and IgGs were detected with 1:2000 (whole cell lysate dot blots) or 1:5000 (all other experiments) dilution of HRP-conjugated goat anti-human κ light chain secondary antibody (RRID: AB_619883). Binding of control antibodies was detected using

1:2000 (whole cell lysate dot blots) or 1:5000 (all other experiments) dilution of HRP-conjugated goat anti-mouse secondary (RRID: AB_2533947).

Following application of primary and secondary antibodies, membranes were treated with HyGlo Quick Spray (Denville Scientific) and imaged using an Amersham Imager A600 (GE Healthcare). Western and dot blot results represent at least two biological replicates per antibody tested. Heat maps were generated by measuring the intensity of the 25-fold diluted cell lysate dots using ImageJ's Gel Analyzer function [73]. Heat maps were generated in Origin 2016, and represent the average of four measurements across two biological replicates.

3.2.9 Immunoprecipitation

Immunoprecipitation was conducted by A. C Patterson-Orazem and Y. Ku. Antibodies in IgG format (0.5 ng/mL) were incubated with 10 mL spent hTM medium (experiment) or 10 mL buffer control (50 mM HEPES pH 7.5, 200 mM NaCl, 10% glycerol) overnight at 4 °C on a rocker. Subsequently, PierceTM Protein A/G Plus agarose suspension (50 µL, ThermoFisher Scientific) was added, and samples were rocked an additional 2 hours at room temperature. Resin was pelleted by centrifugation (10 minutes at 1,000 x g), washed at least 5 times with 500uL buffer. Bound proteins were eluted by adding 50 µL 2x Laemmli buffer, incubated for 10 minutes at room temperature, followed by pelleting and removing the supernatant. Samples were supplemented to 3% v/v β-mercaptoethanol and heated 10 minutes at 95 °C prior to SDS-PAGE and Western blot analysis.

3.2.10 Differential Scanning Fluorimetry

Differential scanning fluorimetry was conducted by A. C. Patterson-Orazem. Melting temperatures were determined by differential scanning fluorimetry using 5x Sypro Orange (Invitrogen) and 1 μ M IgG in 50 mM sodium phosphate pH 7.2, 150 mM NaCl (PBS). Samples, including protein-free controls to account for background fluorescence, were prepared on ice and dispensed into 96-well optical plates (Applied Biosystems) in triplicate, 30 μ L per well. Thermal melts were performed from 25–95 °C with a 1 °C per min ramp rate using an Applied Biosciences Step-One Plus RT-PCR instrument with fixed excitation wavelength (480 nm) and ROX® emission filter (610 nm). Baseline-corrected data were analyzed via Boltzmann sigmoidal regression in Origin 2016; values represent an average of triplicate samples from two separate experiments with sample standard deviation.

RESULTS

3.2.11 Development and identification of candidate antibody sequences

Development and identification of candidate antibody sequences was conducted by Ahlam Qerqez in the Maynard Lab at U. T. Austin; mouse immunizations were conducted by Jeong-min Hyun. Mice were immunized (Figure 3.2) with purified hCCLZ, a well-characterized and stable N-terminal structural domain comprising residues 69-185 and including both dimer and tetramer regions [9]. While our intent was to raise additional antibodies against the mouse equivalent, mCCLZ (comprising residues 55-171), we later learned that cleavage by Factor Xa during purification resulted in a smaller immunogen mLZ (residues 93-171). Mice were given boosters alternating between hCCLZ and mLZ until sufficient immune response to both immunogens was observed in animal titers. Candidate DNA libraries were generated by extracting RNA from mouse spleens by PCR amplification of V_L and V_H using degenerate primers and subsequently cloning the light and heavy chains into scFv plasmid format. Library diversity was assessed by Sanger Sequencing of 10 individual colonies (~150 million single colonies for entire library). Truncated scFvs lacking C-terminal Myc tags were eliminated by panning against anti-Myc antibodies, then myocilin-targeting antibodies were enriched in successive rounds of panning against hCCLZ and mLZ (Figure 3.2). Thirteen candidates were identified for further characterization in scAb format.

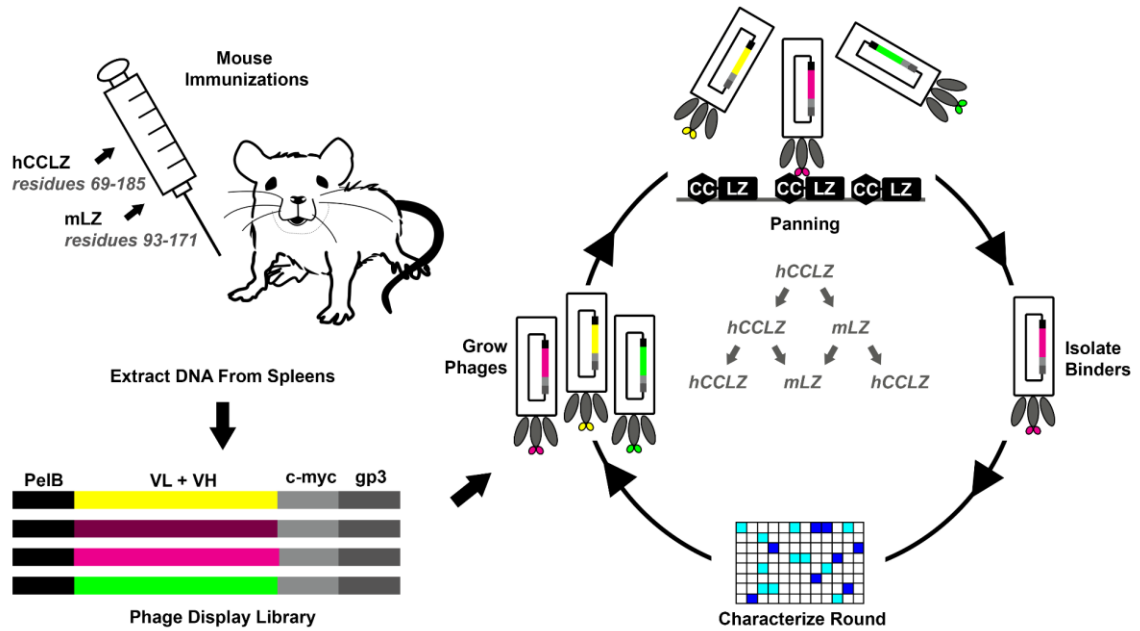


Figure 3.2 Schematic workflow for mouse immunizations, phage display library construction and *in-vitro* selection of candidate antibody sequences. Mice were immunized then boosted with alternate rounds of hCCLZ and mLZ, then sacrificed. Antibody sequences extracted from their spleens with degenerate primers were cloned into a phage display library for successive panning against both immunogens. After 3 rounds of panning, top hits were identified by indirect ELISA and sequenced.

3.2.12 Initial evaluation of LZ-targeting scAbs

Candidate scAbs were produced recombinantly in a soluble form in *E. coli*, expressed and purified for further characterization. All thirteen scAbs expressed well, but six exhibited poor hCCLZ binding in follow up ELISAs (data not shown) and thus were eliminated. The remaining 7 scAbs demonstrate a range of affinities towards purified hCCLZ and mLZ in ELISA (Figure 3.3 A), with strongest affinity and cross-reactivity observed for 1C7, 2F6, and 2G9. Competition ELISAs reveal that 1C7, 2F6, and 2G9 target the same epitope (Figure 3.3 B), whereas 1B9, 1G12, 1A1, and 2A4 appear unique.

Next, 1C7, 2F6, 2G9, 1B9, 1G12, 1A1, and 2A4 scAbs were tested for their ability to recognize myocilin constructs in dot blot (Figure 3.3 C). In this technique, the folded antigen is presented to the antibody, like in ELISA. For these experiments we tested recognition in the context of cell lysates, not purified proteins, but all were constructs we structurally characterized [9]. All antibodies preferentially target LZ (Figure 3.1 B), likely due to boosting with an aberrant mouse construct (see above). Interestingly, the majority of scAbs only weakly recognized the longer hNTD construct (residues 33-226), which includes additional linker regions before and after CCLZ, perhaps due to the previously noted conformational heterogeneity for hNTD [9]. ScAbs that initially displayed poor affinity to mLZ in ELISA (Figure 3.3 A) showed strong cross-reactivity to mLZ in dot blot, likely benefiting from the increased avidity afforded by the dimer-of-dimers architecture of CCLZ.

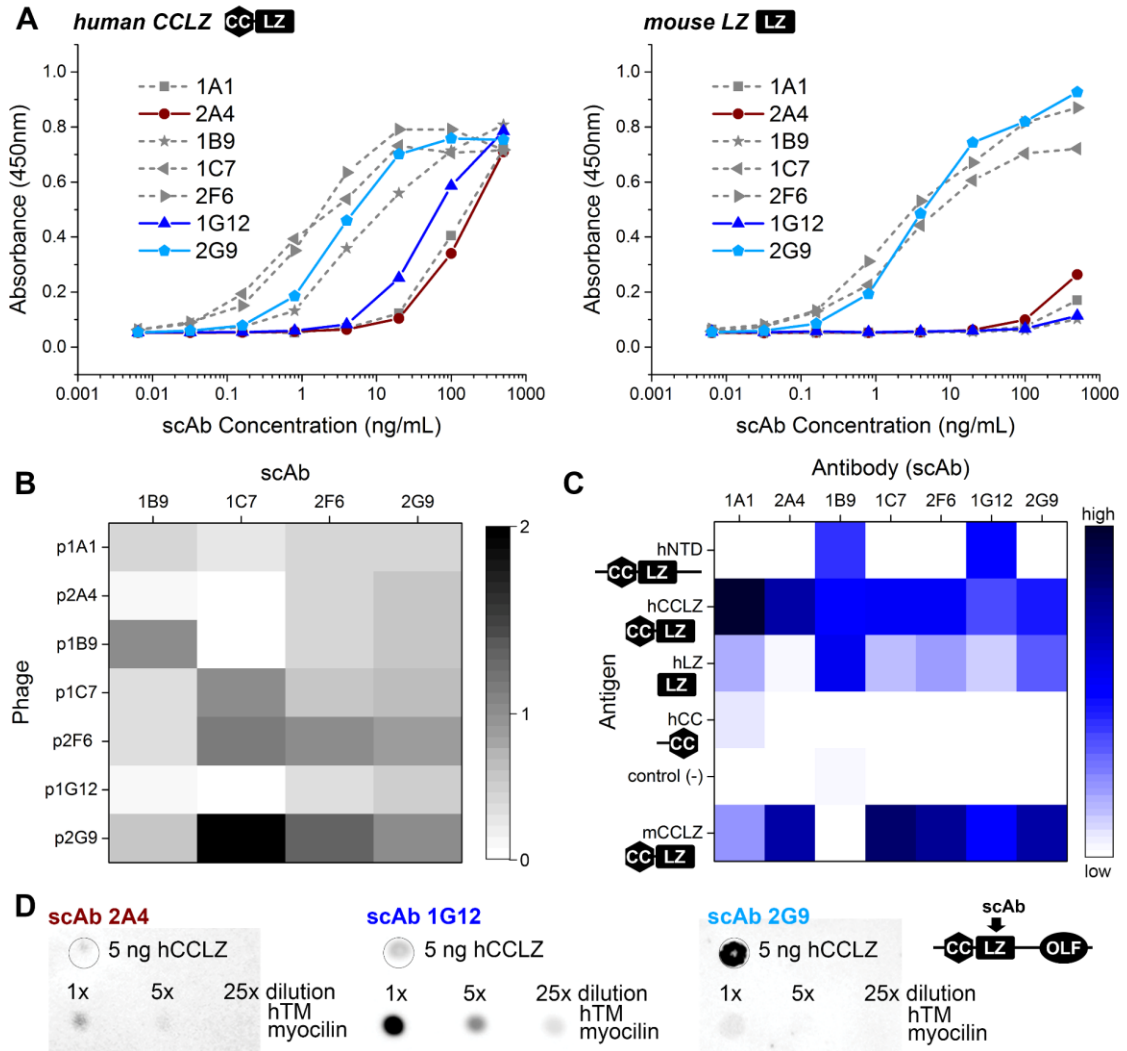


Figure 3.3 Testing of LZ-targeted scAbs. A. Binding affinity of candidate scAbs towards hCCLZ and mLZ, with scAbs important for later discussion highlighted with color and solid curves. B. Heat map representation of competition ELISA results wherein values ≥ 1 indicate competing epitopes. C. Heat map representation of scAb binding affinity in dot blots against cell lysates containing a range of N-terminal myocilin constructs or a control protein with identical tags. D. Representative dot blots testing scAb binding to heparin-enriched hTM-secreted myocilin.

To confirm scAbs recognize full-length myocilin, dot blots with 2A4, 2G9, and 1G12 next performed using immobilized myocilin from spent media of human TM cells (Figure 3D). Dot blots using 2A4 and 2G9 scAbs weakly, but reproducibly detected full-length myocilin. This result was surprising for 2G9, which had exhibited the strongest affinity in ELISA but appeared to very weakly recognize full-length myocilin. Conversely,

dot blots with 1G12 elicited a strong signal for full-length myocilin, perhaps due to greater availability of its epitope within the protein sample or recognition of a less conformational epitope than 2A4 or 2G9 (see below).

3.2.13 Evaluation of CC-targeting scAbs

To identify antibodies targeting the CC domain (Figure 3.1 B), hCC (comprising residues 33-111) was panned against the scFv display library. Promising hits from phage display were expressed in *E. coli* as scAbs and analyzed as previously described for LZ-targeting scAbs. These scAbs exhibit weak affinity for hCC and hCCLZ (Figure 3.4 A), as ELISA was conducted at concentrations up to 10 ug/mL (Figure 3.4 B) compared to 1 ug/mL for LZ-scAbs; scAb 6F7 exhibited the strongest affinity. Competition ELISA revealed that all scAbs competed for the same epitope except for 7H4 (Figure 3.4 B).

Epitope mapping of these new scAbs across the myocilin constructs in dot blot (Figure 3.4 C) demonstrates that 7C8 exhibits promising cross-reactivity towards mCCLZ, and 5D12 and 6C11 weakly recognize proteins within the negative control. Full-length myocilin from primary cell culture was recognized robustly by 5D12, 6C11, 6F7 and 7C8 in dot blot (Figure 3.4 D). Of these, three were chosen for further characterization: 6F7 (high affinity to CC without binding to negative controls), 7C8 (cross-reactivity to mouse even without selection process) and 7H4 (unique epitope).

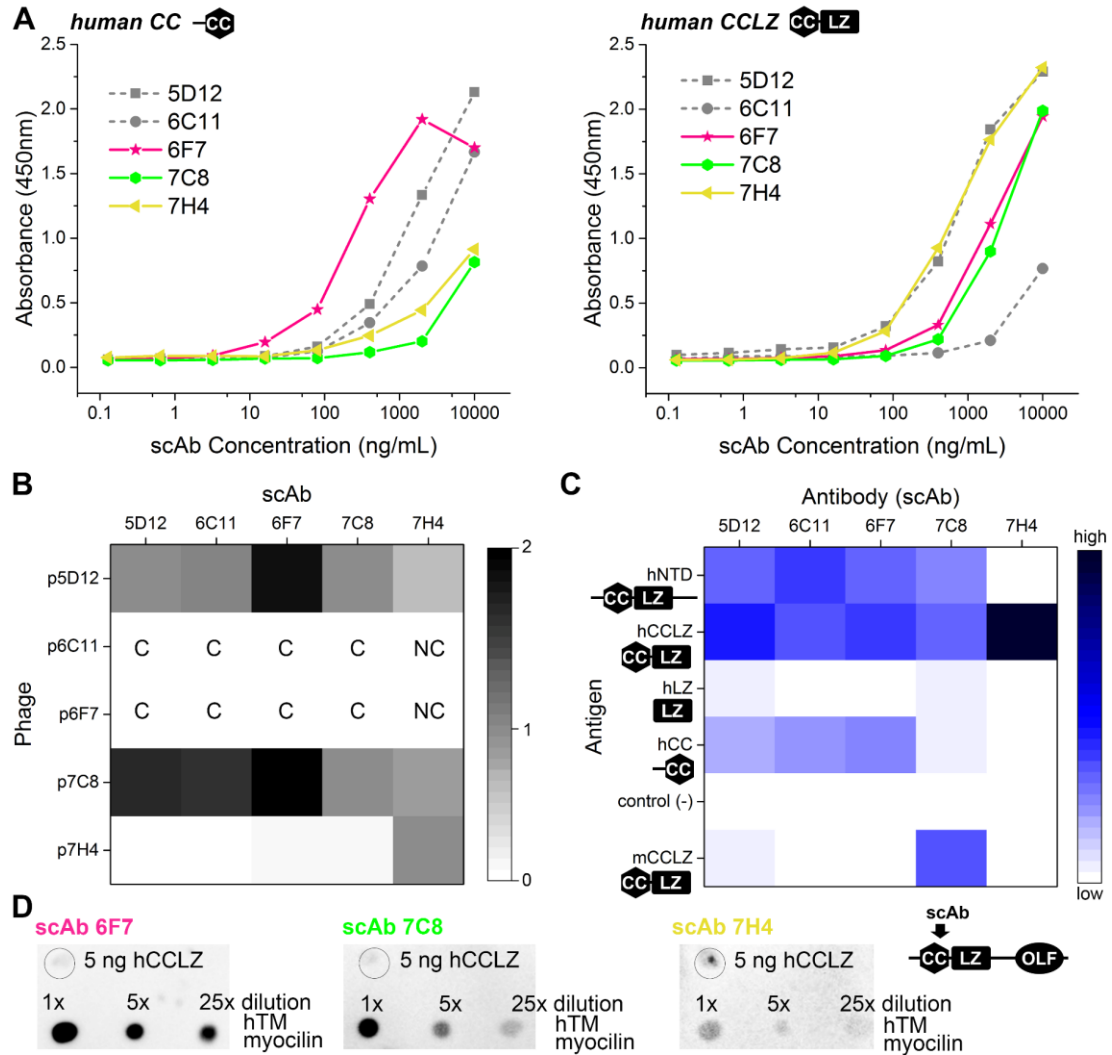


Figure 3.4 Testing of CC-targeted scAbs. A. Binding affinity of candidate scAbs towards hCC and hCCLZ. B. Heat map representation of competition ELISA results wherein values ≥ 1 indicate competing epitopes. Squares marked with letters indicate antibodies which qualitatively compete (C) or don't compete (NC) but for whom IC50 could not be calculated. C. Heat map representation of scAb binding affinity in dot blots against cell lysates containing a range of N-terminal myocilin constructs or a control protein with identical tags. D. Representative dot blots testing scAb binding to heparin-enriched hTM-secreted myocilin.

3.2.14 Conformational specificity of CC- and LZ-targeting IgGs

LZ-targeting (2A4, 2G9, 1G12) and CC-targeting (6F7, 7C8, 7H4) were converted next to IgG format. All but 2G9 were tested for thermal stability, with suitable a range of melting temperatures for constituent Fab domains from 64-77 °C [74]. All six IgGs

recognize the same epitopes as identified in scAb format but displayed apparent increased affinity, as expected for the bivalent format. Since 7H4 still bound the negative control samples, and 7C8 exhibited very weak affinity, neither was considered further.

Conformational specificity was assessed by comparing results from dot blots (Figure 3.5 A) and Western blots (Figure 3.5 B), experiments conducted in parallel with specific quantities of purified myocilin constructs. Most IgGs displayed robust affinity towards hCCLZ and hNTD in dot blots, detecting as little as 5ng. In Western blot, where the samples are denatured, detection was weak (1G12), very weak (6F7) or not visible (2A4). 2G9 robustly recognized only hCCLZ in both Western blot and dot blot, from which we deduce that its epitope includes the C-terminal disulfide bond composed of two Cys185; this epitope is obstructed in longer constructs such as hNTD and full-length myocilin. Thus, at this point 2G9 was removed from further consideration. Weak binding of 6F7 to hNTD, but not to hCCLZ, in Western blot suggests a partial linear epitope including further N-terminal residues not present within hCCLZ.

Finally, LZ-targeting (2A4, 1G12) and CC-targeting (6F7) IgGs were tested for their ability to purify endogenous myocilin from spent media of human TM cells. All three immunoprecipitated full-length myocilin, as well as trace amounts of an N-terminal (~25 kDa) fragment for 2A4 and 1G12 (Figure 3.5 B). Qualitatively, 1G12 immunoprecipitated more myocilin than did 2A4 despite similar epitope and affinity. This observation is consistent with the finding that 2A4 is selective for a folded conformation whereas 1G12 recognizes a less structural epitope, allowing it to bind additional conformers of myocilin that are apparently present in solution.

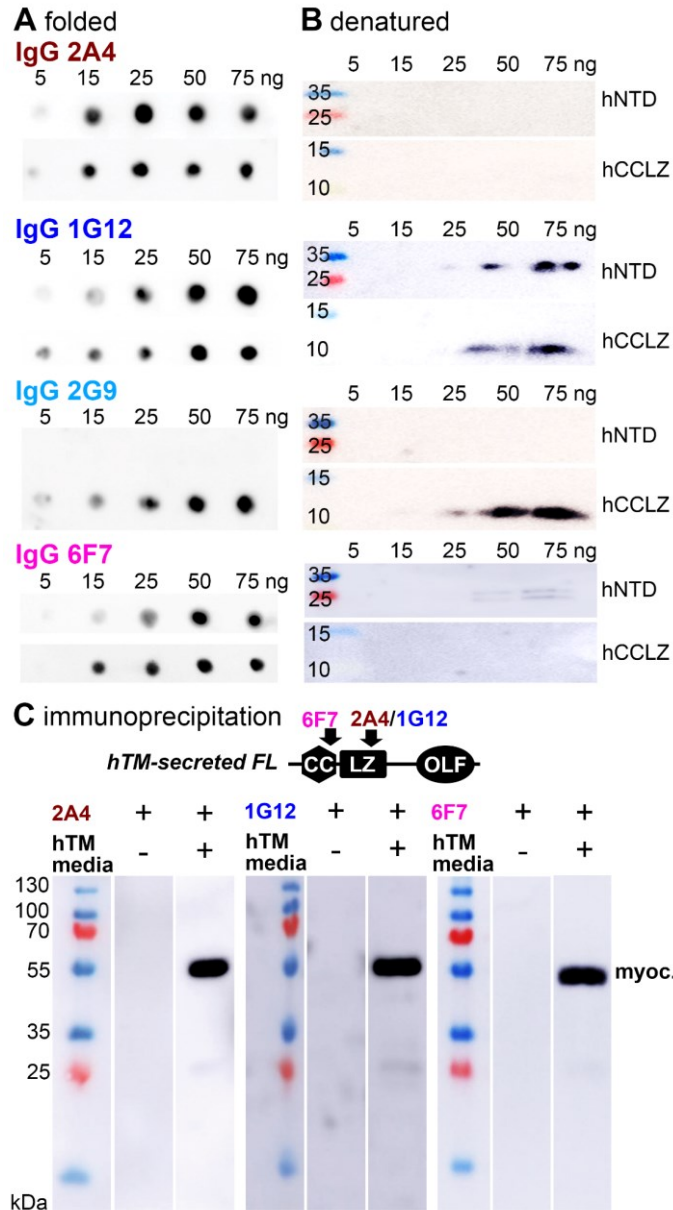


Figure 3.5 Testing of IgG targeting CC and LZ. To assess conformational specificity, IgG binding was assessed in **A.** dot blot and **B.** western blot against nanogram quantities of purified myocilin. **C.** IgG immunoprecipitation of hTM myocilin from spent media reveals a ~55kDa band corresponding to full-length myocilin, detected in western blot using a commercial hLZ-targeting antibody.

3.3 DISCUSSION

The use of conformationally-selective antibodies has been invaluable in gaining new insight into misfolding disease like Alzheimer's [75] and Parkinson's [76]; conversely, not critically evaluating antibodies in use hinders research, as noted for Parkinson's over a decade ago [77]. Structure-based conformational antibodies are even now under development to treat protein misfolding diseases including Alzheimer's (amyloid-beta [59]), amyloidosis (transthyretin [78]) and amyotrophic lateral sclerosis (superoxide dismutase 1 [79, 80]). Inspired by the advances made for other misfolding diseases by the availability of new antibody reagents, we set out to identify conformational antibodies that could be used to provide new structural context for the misfolding-prone myocilin protein in eye research, with the long-term goal of as conversion to a diagnostic or therapeutic. Our antibodies conform to the movement towards sequence-based recombinant antibodies [3, 6], which offer superior reproducibility and longevity over traditional monoclonal and polyclonal antibodies.

We identified 6F7, which targets human CC, as well as 2A4 and 1G12, which detect LZ. 6F7 and 2A4 are highly sensitive to the conformation of myocilin, as they only recognize the protein when in the folded form and not when it is denatured. 2A4 and 1G12 are both cross reactive with mouse LZ, streamlining research reagents across relevant cells, tissue samples, and glaucoma animal models [81, 82]. It is likely that a conformational epitope conserved in mouse and human is conserved across other species used in glaucoma research, such as monkey or cat, as has been found for Ebola virus nucleoprotein [83] and pollen antigens [84].

Through our workflow of antibody development, we have already started to glean new insight about myocilin present in spent media from human TM cells. First, our finding that the LZ-targeting IgGs 2A4 and 1G12 exhibit similar affinity towards recombinant myocilin yet the less-conformational 1G12 immunoprecipitates more myocilin from TM media than 2A4 indicates there is a heterogeneous mixture of myocilin, including both native and non-native conformations. While the N-terminal region confers the oligomerization state of myocilin [9, 85], endogenous myocilin has been identified in a variety of oligomerization states, ranging from dimer [86] to tetramer and higher [38, 39], with unknown functional or glaucoma relevance. Our antibodies offer the first opportunity to compare these myocilin species, and see how they change with glaucoma-relevant stressors, including but not limited to myocilin mutations [62], steroid treatment [51], mechanical stress [64] and oxidative stress [87, 88]. Second, immunoprecipitation with our new IgGs yielded full-length myocilin (~55kDa) as well as a minority of truncated myocilin (~25kDa). While myocilin cleavage has been observed in mammalian expression systems [40, 67], to our knowledge, ours is the first observation of myocilin fragments in spent media from primary cell culture; fragments may have been detected in lysed TM cells [34]. Proteolytic cleavage for myocilin may play a functional role, as it does for olfactomedin family-members gliomedin [42, 43] and latrophilin [41]. More broadly, the availability of a myocilin epitope for detection by any given antibody might be modulated by posttranslational modification [29, 39] and contextual binding partners. In sum, we anticipate that these new antibodies, in conjunction with existing antibodies targeting linear epitopes and those detecting other structural domains, will allow researchers to map myocilin with a new level of detail, in many relevant samples across vision research.

CHAPTER 4. DIFFERENTIAL MISFOLDING PROPERTIES OF GLAUCOMA-ASSOCIATED OLFACTOMEDIN DOMAINS FROM HUMAN AND MOUSE.

Adapted from “A. C. Patterson-Orazem, S. E. Hill, Y. Wang, I. M. Dominic, C. K. Hall & R. L. Lieberman; Differential misfolding properties of glaucoma-associated olfactomedin domains from human and mouse; in press ACS Biochemistry, 2019.” Reproduced with permission from ACS Biochemistry; unpublished work copyright 2019, American Chemical Society.

I contributed structural determination of mouse OLF, ThT-binding experiments, in-vitro aggregation kinetics experiments and some thermal stability measurements, and the design and execution of all figures which include these data. I contributed to the organization, writing and editing of the manuscript.

S. E. Hill contributed to experimental design, initial expression and purification of mouse OLF, interpretation of aggregation kinetics, and atomic force microscopy experiments and figure. Y. Wang contributed molecular dynamics simulations and related sub-figures. I. M. Dominic contributed protein purifications and thermal stability measurements. C. K. Hall contributed molecular dynamics experimental design and editing of the paper. R. L. Lieberman contributed to experimental design and to the writing of the manuscript.

4.1 Abstract.

Mutations in myocilin, predominantly within its olfactomedin (OLF) domain, are causative for the heritable form of open angle glaucoma in humans. Surprisingly, mice expressing Tyr423His mutant myocilin, corresponding to a severe glaucoma-causing mutation (Tyr437His) in human subjects, exhibit a weak, if any, glaucoma phenotype. To address possible protein-level discrepancies between mouse and human OLFs, which might lead to this outcome, biophysical properties of mouse OLF were characterized for comparison with those of human OLF. The 1.55 Å resolution crystal structure of mouse myocilin OLF reveals an asymmetric 5-bladed β -propeller that is nearly indistinguishable from previous structures of human OLF. Wild type and selected mutant mouse OLFs

mirror thermal stabilities of their human OLF counterparts, including characteristic stabilization in the presence of calcium. Mouse OLF forms thioflavin T-positive aggregates with similar end-point morphology as human OLF, but amyloid aggregation kinetic rates of mouse OLF are faster than human OLF. Simulations and experiments support the interpretation that kinetics of mouse OLF are faster because of decreased charge repulsion arising from more neutral surface electrostatics. Taken together, phenotypic differences observed in mouse and human studies of mutant myocilin could be a function of aggregation kinetics rates, which would alter the lifetime of putatively protofibrillar intermediates.

4.2 Introduction.

Mouse models offer valuable insights into human disease progression and are often the first testing grounds for novel treatments. In the case of protein misfolding disorders, however, mouse models have been somewhat less successful, either failing to replicate key disease phenotypes found in humans or exhibiting a weaker phenotype. In mouse models of tau-based Alzheimer disease and transthyretin-based amyloidosis [89, 90], differences between the mouse and human proteins have been attributed to differences in observed phenotypes. At the molecular level, it is known that even minor changes in protein sequence can have dramatic effects on protein structure, stability, and misfolding properties in the cell [91].

A recent addition to the list of protein misfolding disorders is a heritable sub-type of the age-onset ocular disease glaucoma, a worldwide leading cause of blindness. Mutations in human (*Homo sapiens*) myocilin (Uniprot Q99972), predominantly within its

olfactomedin (*HsOLF*) domain, are causative for glaucoma in approximately 3 million of the 70 million total glaucoma patients [92, 93]. The predominant pathogenic mechanism is a toxic gain of function: mutant myocilin is prone to cytotoxic aggregation within the trabecular meshwork (TM) cells that maintain the extracellular matrix that serves as an anatomical sieve to drain aqueous humor. This cytotoxicity hastens the causal risk factor of elevated pressure leading to retinal ganglion cell (RGC) death and vision loss characteristic of glaucoma [94]. Typically, individuals expressing a mutant form of myocilin, such as the variant Tyr437His, exhibit severely elevated intraocular pressure (IOP, 44 mmHg vs 20 mmHg in control population) at a young age (20 years old) [95, 96]. Data to date indicate that myocilin is not otherwise a susceptibility gene for sporadic forms of glaucoma [22].

Numerous glaucoma rodent models are available and widely used in the field [82], but for myocilin-associated glaucoma, a robust IOP elevation phenotype accompanied by RGC loss has been a challenge to elicit in mouse. In two mouse models that express either the human Tyr437His myocilin mutation [97] or its equivalent in *Mus musculus* myocilin (Uniprot O70624), Tyr423His [98], modest IOP elevation was measured [97, 98], but only in older mice. In these models, which both used the bacterial artificial chromosome method that overexpresses the target protein, IOP elevation was accompanied by some degenerative features in RGCs [97, 98]. No increase in IOP was observed in mice when Tyr423His was introduced in the endogenous mouse myocilin gene [99]. In a fourth transgenic model, high levels of human mutant myocilin Tyr437His expressed specifically in eye drainage structures and sclera using cytomegalovirus methods, exhibit the strongest and earliest glaucoma-like phenotypes to date [18].

Here we test the hypothesis that molecular level differences in *HsOLF* and mouse *OLF* (*MmOLF*) explain the differing phenotypes observed in these myocilin-glaucoma models. Although *HsOLF* and *MmOLF* share high sequence identity (87%), differences are observed in regions thought to template amyloid aggregation [36], raising the possibility this could contribute to species-based differences in disease phenotype, as in other misfolding disorders. We compare structural, biophysical, and aggregation properties of *MmOLF* with well-studied characteristics of *HsOLF*. Our results demonstrate high levels of similarities between the two proteins in their folded state and final aggregated states, but faster aggregation rates observed for *MmOLF* point to the possibility that a toxic species relevant to glaucoma is hidden in a transiently present protofibrillar intermediate.

4.3 Materials and Methods.

4.3.1 Molecular biology.

Molecular biology was conducted by A. C. Patterson-Orazem and I. M. Dominic. Codon-optimized *MmOLF* was synthesized and sub-cloned by Genscript into pMAL-c4x vector similar to previously published *HsOLF*, except that the Factor Xa cleavage site was replaced with a tobacco etch virus (TEV) protease cleavage site[100]. Maltose binding protein (MBP)-*MmOLF* fusion variants Ala413Thr, Asp366Ala, Tyr423His and Ile485Phe, and MBP-*HsOLF* variant Ile431Val Thr435Ile were all produced by site-directed mutagenesis following manufacturer's recommended protocol (Quick-Change Lightning II Kit, Agilent) and verified by DNA sequencing (Operon or Genscript). Primer sequences are provided in Table 4.1.

Table 4.1 Primers used for site-directed mutagenesis of MmOLF and HsOLF used in this manuscript.

Mutant	Direction	Primer Sequence
<i>MmOLF</i> D366A	Forward	5'-TCCACCGCCAGAGCAATGTCGGTATAGCCAC-3'
	Reverse	5'-GTGGCTATACCGACATTGCTCTGGCGGTGGA-3'
<i>MmOLF</i> A413T	Forward	5'-ATAACAAACGCGTTCGTCACGCTCTGCTTACGG-3'
	Reverse	5'-CCGTAAGCAGAGCGTGACGAACGCGTTTGTAT-3'
<i>MmOLF</i> Y423H	Forward	5'-ATAGCTGCTCACGGTGTGCAGAATACCGCAGATAA-3'
	Reverse	5'-TTATCTGCGGTATTCTGCACACCGTGAGCAGCTAT-3'
<i>MmOLF</i> I485F	Forward	5'-CATTTCCAGCAGCTTGAAATCATAGGTCACCATGTTGA-3'
	Reverse	5'-TCAACATGGTGACCTATGATTTCAAGCTGCTGGAAATG-3'
<i>HsOLF</i> I431V T435I	Forward	5'-CCAATGCCTTCGTTCATCTGTGGCATCTTGACACC-3'
	Reverse	5'-GGTGTACAAGATGCCACAGATGACGAAGGCATTGG-3'

4.3.2 Expression and purification.

HsOLF and *MsOLF* expression and purification, as previously described [55], were conducted by A. C. Patterson and I. M. Dominic. *E. coli* Rosetta Gami 2 cells transformed with myocilin plasmid were inoculated to OD₆₀₀ ~ 0.1 and grown in Superior Broth (US Biological) at 37 °C to OD₆₀₀ of 0.8 to 1.0, cooled to 18 °C, then induced with 0.5 mM isopropyl-β-D-thiogalactopyranoside and 1 mM CaCl₂ overnight. Cells were harvested by centrifugation, flash cooled in liquid nitrogen, and stored at -80 °C. Cell paste (5 g) was gently suspended in 20 mL chilled phosphate buffered saline composed of 10 mM Na₂HPO₄/KH₂PO₄, 200 mM NaCl (PBS), supplemented with half an EDTA-free Roche Protease Inhibitor tablet and 1 mM EDTA, lysed by French press (Sim-Aminco French Press, 25 mL FA-023 cell from Thermo Electron Corporation) and centrifuged at 110,000xg (Beckman Avanti JXN3, JS-24.15 rotor). Clarified cell lysate was purified on AKTA Pure and Purifier systems (GE Healthcare) by amylose affinity chromatography (25 mL column packed with New England BioLabs Amylose Resin), equilibrated with PBS, eluted with PBS supplemented with 10 mM maltose, and concentrated in 15 mL 30 kDa-cutoff Amicon filters (Millipore) prior to fractionation by size-exclusion chromatography

(SEC) with a Superdex-75 pg (GE Healthcare) in PBS buffer. For Tyr423His and Ile485Phe MBP-*Mm*OLF variants, fractions proximal to 55 mL elution volume were concentrated and further purified using a Superdex-75 GL (GE Healthcare) to eliminate residual aggregated protein. Fractions containing monomeric MBP-OLF fusion proteins were cleaved by TEV protease [101] using a 1 TEV:5 MBP-OLF mass ratio overnight at room temperature, then purified by nickel affinity (1mL HisTrap FF, GE Healthcare), amylose affinity and SEC as previously described [55]. After cleavage, pure protein was concentrated with 15-mL 10 kDa-cutoff Amicon filtration units (Millipore).

For aggregation kinetics assays, cleaved *Mm*OLF was subjected to cation-exchange after the first amylose step to bind and remove trace TEV protease. This was accomplished by diluting OLF-containing fractions to 50mM NaCl with 10 mM Na₂HPO₄/KH₂PO₄ and applying the sample to a HiTrap CantoS column (1mL, GE Healthcare) equilibrated with 10 mM Na₂HPO₄/KH₂PO₄, 50 mM NaCl. Residual TEV protease was eluted from the column with gradient to 2M NaCl.

Protein purity was assessed by standard SDS-PAGE analysis with Coomassie staining. Protein concentrations were determined by spectrophotometry using molar extinction coefficients for fusion proteins (human: 134,775 M⁻¹cm⁻¹, mouse: 133,285 M⁻¹cm⁻¹) or for cleaved OLF (human: 68,425 M⁻¹ cm⁻¹ and mouse: 65,440 M⁻¹cm⁻¹) calculated by ExPaSy ProtParam [102]. Predicted isoelectric points were also calculated in ExPaSy.

4.3.3 Crystallization and structure determination.

Crystallization and structure determination were conducted by A. C. Patterson-Orazem with data collection assistance from S. E. Hill. Rectangular prismatic crystals of *MmOLF*, 50-70 μM in diameter, grew within 3 weeks at 16 $^{\circ}\text{C}$ in 4 μL sitting drops containing 1:1 (v/v) of 30 mg/mL *MmOLF* in PBS pH 7.2 and mother liquor solution containing 10% PEG-8000, 200 mM MgCl_2 . Diffraction data were collected at the Southeast Regional Collaborative Access Team (SER-CAT) 22-ID beamline and processed using HKL-3000 [103]. The *MmOLF* structure was solved by molecular replacement in Phaser [104] using the *HsOLF* structure 4WXQ as a search model. The *MmOLF* model was iteratively built and refined using Coot [105] and Phenix.refine [104]. The structure has been deposited to the PDB with ID: 6NAX, and statistics are shown in Table 4.2. Figures were prepared in PyMOL [106], and electrostatics using APBS-PDB₂PQR [107].

Table 4.2. Data collection and refinement statistics for the structure of the olfactomedin (OLF) domain of mouse myocilin, PDB 6NAX.

Data Collection	
Space group	P4
Cell dimensions	
a, b, c (Å)	112.0, 112.0, 44.1
α, β, γ (degrees)	90, 90, 90
Resolution (Å)	33.11 - 1.55 (1.61 - 1.55)
Reflections	
Total	355,190 (29,541)
Unique	79,283 (7,499)
Redundancy	4.5 (3.9)
Completeness (%)	98.5 (95.2)
Wilson B-factor	11.6
R_{sym}	0.0671 (0.210)
I/σ	18.0 (6.1)
CC1/2	0.996 (0.950)
CC*	0.999 (0.987)
Refinement	
Resolution (Å)	33.11 - 1.55 (1.61 - 1.55)
Reflections	
Used in refinement	78,413 (7,499)
Used for R-free	2,000 (193)
R-work/R-free	0.158 (0.173) / 0.178 (0.201)
CC (work) / CC (free)	0.968 (0.934) / 0.970 (0.916)
Molecules	
Protein residues	518
Ligands	29
Solvent	623
B-factor: average	15.0
Protein residues	13.2
Ligands	26.8
Solvent	26.3
RMS	
Bond-lengths (Å)	0.01
Bond-lengths (deg)	0.88
Ramachandran	
Favored (%)	96.69
Allowed (%)	3.31
Outliers (%)	0
Clashscore	3.58

4.3.4 *Thermal stability assay.*

Thermal stability was measured by differential scanning fluorimetry using Sypro Orange (Invitrogen), as previously described [55], and conducted by A. C. Patterson-Orazem and I. M. Dominic. Final mixtures of 30 μ L were prepared at room temperature in 96-well optical plates (Applied Biosystems) and contained protein solutions at a final concentration of 0.5–1.5 μ M in HEPES-buffered saline (10 mM HEPES pH 7.5, 200 mM NaCl). Where indicated, 50 mM maltose and 10 mM CaCl₂ were present. Each experiment contained control wells accounting for background protein, maltose and calcium fluorescence. Fluorescence data were collected on an Applied Biosciences Step-One Plus RT-PCR instrument equipped with fixed excitation wavelength (480 nm) and ROX® emission filter (610 nm). Thermal melts were performed from 25–95 °C with a 1 °C per min increase and acquired data were analyzed with Igor Pro, version 6.37 (WaveMetrics).

4.3.5 *Thioflavin-T (ThT) endpoint fluorescence and de novo aggregation assays.*

Endpoint fluorescence and de novo aggregation assays were conducted by A. C. Patterson-Orazem, with assistance from S. E. Hill. Aggregated MBP-*Mm*OLF species fractionated by Superdex-75 pg were concentrated to 30 μ M protein and supplemented with 10 μ M ThT in PBS. Aliquots (40 μ L) were dispensed in triplicate in half-area flat-bottomed 96-well non-binding plates (Corning #3993). After incubation for 10 min, ThT fluorescence was measured at room temperature using excitation filter 440/30 nm and emission filter 485/20 nm (BioTek Synergy 2). Results represent the average of two biological replicates.

For *de novo* aggregation assays, triplicate samples comprising 150 μL of 30 μM cleaved, monomeric *MmOLF* and 10 μM ThT in PBS were incubated at 42 $^{\circ}\text{C}$ in black flat-bottom medium binding plates (Greiner Bio One #655076), Fluorescence was monitored over 72 hours at 10-minute intervals using the same BioTek plate reader and filters as listed above [100]. Representative results were normalized to the maximum fluorescence of wild type *HsOLF* and plotted in Origin Professional 2016.

4.3.6 Coarse grain (PRIME20) molecular dynamics simulations.

Molecular dynamics simulations were conducted Y. Wang under direction of C. K. Hall. Discontinuous molecular dynamics (DMD) [108], a fast alternative to conventional molecular dynamics, were used in conjunction with the PRIME20, coarse-grained protein model developed in the Hall group [109] to simulate aggregation of *MmOLF* derived peptides, analogous to those of human peptides [110]. In the PRIME20 model, each of twenty different amino acids has three backbone spheres (NH, $\text{C}\alpha$ and CO) and one sidechain sphere (R). Glycine does not have a sidechain sphere. Each sidechain sphere of the twenty different amino acids has a distinct hard sphere diameter (effective van der Waals radius) and distinct sidechain-to-backbone distances (R- $\text{C}\alpha$, R-NH, R-CO). The two major types of non-bonded interactions captured in PRIME20 are directional hydrogen bonding between backbone NH and CO spheres modeled as a directional square well potential and sidechain-sidechain square well interactions between any pair of the twenty different amino acids. Cheon *et al.* [111] used a perceptron learning algorithm to reduce the 210 possible independent square well depths between the 20 different amino acids to 19 different parameter groups while maintaining the 210 independent square well widths to ensure physically meaningful pair interaction energies in discriminating decoys from

native structures in the PDB database. All the other non-bonded interactions are modeled as hard sphere interactions. A detailed description of the derivation of the geometric and energetic parameters of the PRIME20 model is given in earlier work [109, 111, 112].

DMD/PRIME20 simulations of mouse P1 and P3 peptide aggregation were performed in the canonical ensemble (fixed number of particles, constant volume and temperature). The simulation temperature was maintained constant by using the Andersen thermostat [113]. The system contained eight monomeric peptides in a cubic box with box length equal to 110.0 Å corresponding to a total peptide concentration of 20 mM. The reduced temperature was defined as $T^* = k_B T / \epsilon_{HB}$, where the hydrogen bonding energy, $\epsilon_{HB} = 12.47$ kJ/mol. The reduced temperature T^* was chosen to be 0.2, which corresponds to 342 K in real temperature [114]. Ten independent simulation runs were performed, each lasting for at least 220 μ s.

The aggregation propensities of human and the mouse P3 were calculated by introducing the amyloid-forming propensity, β , using the following equation:

$$\beta = \frac{1}{N} \sum_{i=1}^N \frac{n_{HB}(i)}{n_{Site}(i)} \quad (1)$$

where $n_{HB}(i)$ is the total number of backbone hydrogen bonding sites (NH and C=O beads) on the i^{th} peptide in the aggregate that form β -sheet hydrogen bonds, and $n_{Site}(i)$ is the total number of NH and C=O beads on the i^{th} peptide in the aggregate. N is the total number of peptides in the system. β ranges from 1 for a perfect β -sheet structure

with strong amyloid forming propensity, to 0 for a monomeric state or disordered oligomer with weak amyloid forming propensity.

4.3.7 Atomic force microscopy (AFM).

Atomic force microscopy was conducted by S. E. Hill. Immediately after the ThT aggregation assay above, triplicate samples comprising 150 μ L each were removed, combined into a 1.5 mL centrifuge tube, and left at room temperature overnight to pellet by gravity. After visible separation of the insoluble aggregates into a pellet, 40 μ L of the pellet sample was deposited onto freshly-cleaved mica for 30 minutes, rinsed for 3 seconds with ultrapure water, and left to dry overnight in a Petri dish. After drying, the samples were imaged in air with a MFP-3D atomic force microscope (Asylum Research) using PPP-FMR (NanoAndMore) silicon tips with nominal tip radii less than 7 nm. The cantilever was driven at 60–80 kHz in alternating current mode and a scan rate of 0.5 Hz with 512 x 512-pixel or 1024 x 1024-pixel resolution. Raw image data were corrected for image bow and slope using software provided by Asylum Research.

4.4 RESULTS

4.4.1 *MmOLF* structure.

To gain insight into the structural similarities and differences between native *MmOLF* and *HsOLF*, we solved the crystal structure of *MmOLF*, to 1.55 Å resolution (Table 4.2). The 5-bladed β -propeller is nearly identical to that of *HsOLF* (root mean squared deviation (RMSD) = 0.7 Å, Figure 4.1 A). The disulfide clasp that covalently links the N and C termini is conserved, the heptacoordinate Ca^{2+} , pentacoordinate Na^+ and corresponding coordinating ligands identified for *HsOLF* [8] are all present and in similar conformations (Figure 4.1 B). However, while the surface electrostatics of *HsOLF* are predominantly negative [8], the *MmOLF* surface is more varied, with distinct positively-charged patches at both the top and bottom faces of the propeller (Figure 4.1 C).

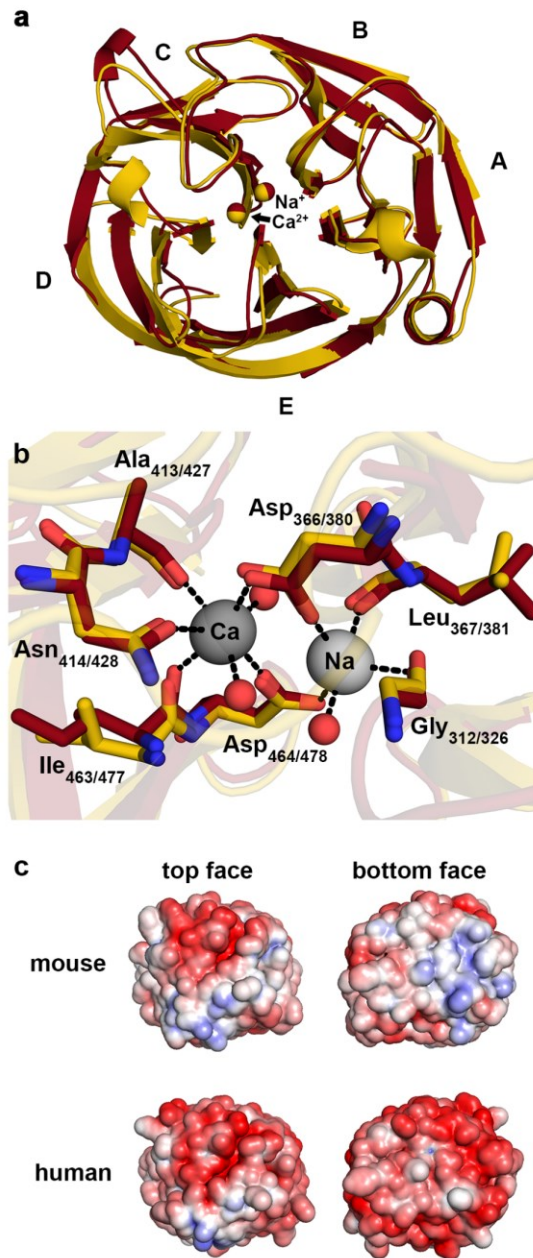


Figure 4.1 *MmOLF* and *HsOLF* share key structural features. (A) Superposition of *MmOLF* structure (dark red, 1.55 Å resolution) and *HsOLF* (PDB code 4WXQ, gold, 2.15 Å resolution), view of top face, RMSD = 0.73 Å. (B) Ca²⁺, Na⁺, and corresponding coordinating residues in the central cavity of *MmOLF* and *HsOLF* are nearly identical. Waters are shown as red spheres, and hydrogen bonding interactions < 3 Å are shown as dashed lines. (C) Surface electrostatics demonstrate similar potentials across the top face, but increased positive charge on the bottom face of *MmOLF* relative to *HsOLF*. Surface potentials are colored negative (red, -5 kT/e-) to positive (blue, +5 kT/e-).

Glaucoma-associated *HsOLF* mutations selected next as representatives for further inspection and study in the context of *MmOLF* represent a range of residual thermal stability [12, 55] and disease phenotypes [115]. These variants range from Ala427Thr, associated with variable (familial and sporadic, and diagnosed past the age of 65) glaucoma phenotypes in a small population [116] and which might only be causative in presence of other genetic risk factors, to the severe Tyr437His mutation which results in juvenile-onset glaucoma symptoms and dramatic elevation in IOP [96] (Figure 4.2 A). Tyr437His and Ile499Phe are located within the hydrophobic interface between propeller blades, while Ala427Thr and Asp380Ala are proximal to the calcium-binding site (Figure 4.2 A).

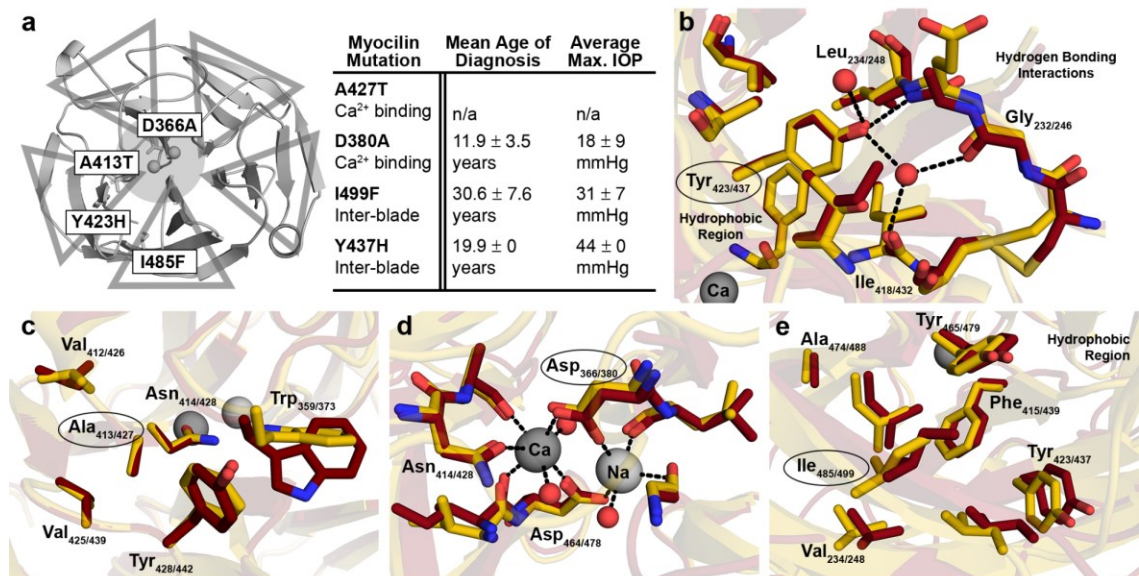


Figure 4.2 Biochemical environment of glaucoma-causing myocilin mutations. (A) Representing a range of clinical phenotypes (table to the right)[115], select myocilin mutations are either in a hydrophobic interface between the blades, highlighted by triangles, or near the calcium-binding site, indicated by shaded circle. (B-E) Overlay of mouse, dark red, and human, gold, OLF structures demonstrate similarities in the biochemical environment of (B) human Tyr437 and its mouse equivalent Tyr423; (C) Ala427 and mouse Ala413; (D) Asp380 and mouse Asp366; and (E) Ile499 and mouse Ile485. Waters are shown as red spheres, and hydrogen bonding interactions < 3Å are shown as dashed lines.

Inspection of these positions in the context of *Mm*OLF reinforces the similarity between the *Hs*OLF and *Mm*OLF structures. Tyr423 in *Mm*OLF (due to a shorter N-terminal signal peptide in *Mm*OLF numbering is offset from *Hs*OLF by 14 amino acids) participates in hydrophobic packing and water-mediated beta-turn stabilizing hydrogen bonding interactions (Figure 4.2 B), both of which are expected to be strongly impacted by mutation to histidine. Ala413 in *Mm*OLF is located under surface loops known to be mobile in *Hs*OLF [8] and other OLF domain family members [117], and should be able to accommodate conservative mutations (Figure 4.2 C). Mutation of Asp366 abolishes calcium binding (Figure 4.2 D) by removing a key metal-coordinating side chain [8, 118]. Ile485 is engaged in hydrophobic packing, which is likely disrupted by the increased steric hindrance of mutation to phenylalanine (Figure 4.2 E). Thus, based on structure, these mutations to *Mm*OLF are expected to have a similar impact on stability and aggregation as previously observed for *Hs*OLF.

4.4.2 Thermal stability of wild-type and mutant *Mm*OLFs.

Expression and purification of *Mm*OLFs proceeded as for *Hs*OLF published previously[55], utilizing a N-terminal maltose binding protein (MBP) fusion to enhance folding efficiency and as a purification handle. Similar to purification of *Hs*OLF, the initial MBP-*Mm*OLF fusion protein is isolated from *E. coli* in two forms (Figure 4.3 A): a misfolded, thioflavin-T-positive aggregate suggestive of amyloid (Figure 4.3 B,C) and a properly folded form used subsequently for characterization, including the structural analysis above, thermal stability and aggregation kinetics assays below. Thermal stability of wild-type *Mm*OLF resembles that of *Hs*OLF (Table 4.3). All four aforementioned disease variants, Ala413Thr, Ile485Phe, Asp366Ala, and Tyr423His, result in

compromised *Mm*OLF stability, with similar trends to *Hs*OLF variants [55], albeit with slightly higher melting temperatures (Table 4.3, Figure 4.4). Wild-type *Mm*OLF as well as *Mm*OLF variants Ala413Thr, Ile485Phe, and Tyr423His, were stabilized in the presence of calcium, confirming that a calcium binding site is retained, as in *Hs*OLF [8, 118]. The outlier is the *Mm*OLF Asp366Ala variant (Table 4.3), confirming the critical importance of Asp366 to calcium binding in *Mm*OLF, like its equivalent Asp380 in *Hs*OLF [118] and confirmed in our crystal structure (Figure 4.1, Figure 4.2).

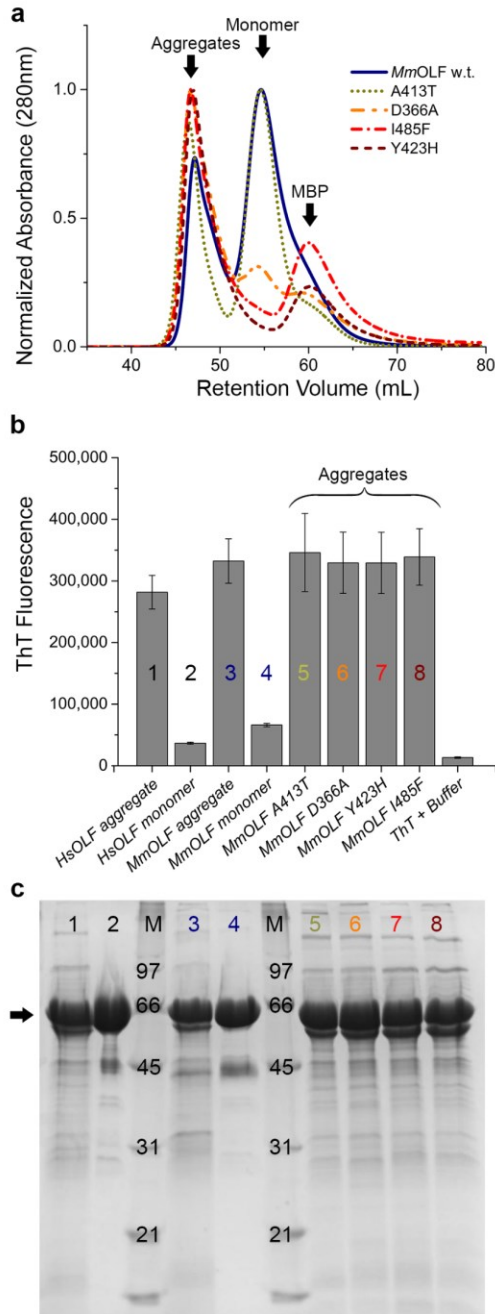


Figure 4.3 Aggregates of MBP-*MmOLF* isolated from *E. coli* are ThT-positive, a hallmark of amyloid. (A) Aligned chromatograms from Superdex-75 purifications of wild-type and mutant MBP-*MmOLF* fusion proteins. (B) ThT fluorescence of MBP-*MmOLF* aggregates compared to selected monomeric MBP-OLFs and (C) corresponding SDS-PAGE analysis demonstrates that, for equal amounts of protein, the average ThT fluorescence is similar for human and mouse.

Table 4.3. Thermal stability of wild-type and mutant *Mm*OLF resemble *Hs*OLF counterparts. Melting temperature (T_M) measured by differential scanning fluorimetry.

Protein	Mouse		Human	
	T _M (°C)	ΔT _M + CaCl ₂	T _M (°C)	ΔT _M + CaCl ₂
Wild Type	52.3 ± 0.1	+ 7.8	53.0 ± 0.5	+ 6.6
A413T (A427T)^a	50.8 ± 0.1	+ 8.1	48.3 ± 0.3	+ 6.9
D366A (D380A)^b	47.5 ± 0.2	- 1.2	46.6 ± 0.3	- 1.5
I485F (I499F)^b	43.9 ± 0.5	+ 8.5	42.8 ± 0.1	+ 7.6
Y423H (Y437H)^b	42.1 ± 0.1	+ 9.8	40.3 ± 0.4	+ 8.3
(I431V/T435I)^c	n/a	n/a	54 ± 2	+8.8

^aNumbering for *Hs*OLF mutants shown in parentheses.

^bLiterature values [118] listed.

^cValues obtained using cleaved *Hs*OLF.

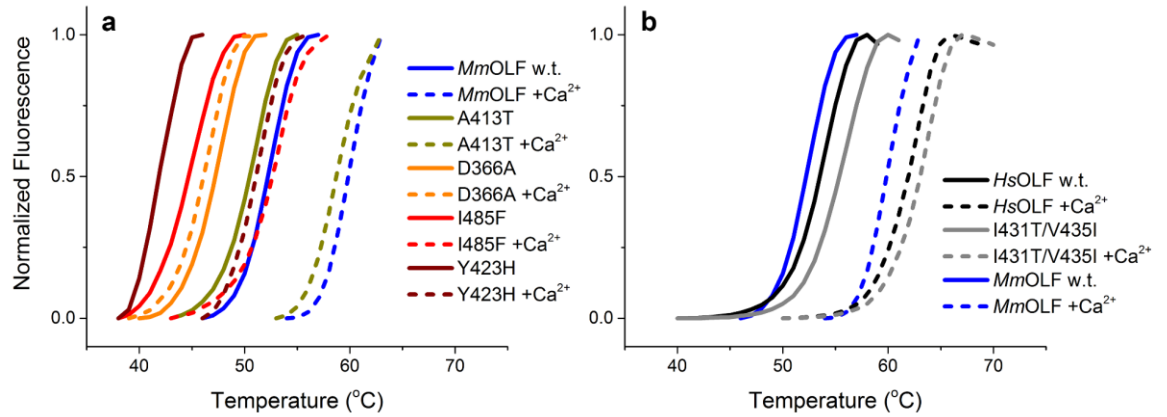


Figure 4.4 Representative differential scanning fluorimetry thermal melt curves for (A) *Mm*OLF wild-type and mutants and (B) *Hs*OLF wild-type and mutant, with and without 10mM CaCl₂.

4.4.3 Aggregation properties of *MmOLF*.

Given the result of ThT-positive cellular aggregates produced by *E. coli* during expression, coupled with nearly identical thermal stabilities and native structures of *MmOLF* and *HsOLF*, similar *in-vitro* aggregation kinetics were expected. Surprisingly, *MmOLF* forms ThT-positive aggregates faster than *HsOLF* under assay conditions developed previously for *HsOLF*, namely aggregation at 42 °C without agitation in a fluorescence plate reader [36] (Figure 4.5 A), with statistically significant differences in ThT fluorescence ($p < 0.0001$, ANOVA) at 24 and 72 hour timepoints.

One possible explanation for the increased initial rate of *MmOLF* aggregation includes differences in the *MmOLF* sequence within previously-identified *HsOLF* amyloidogenic peptide regions [36]. These amyloidogenic stretches (Figure 4.5 B) comprise *HsOLF* residues 326–337 (P1, *MmOLF* residues 312–323) and residues 426–442 (P3, *MmOLF* residues 412–428). Peptides P1 and P3 replicate disparate fibril morphologies associated with different aggregation conditions for the full *HsOLF* domain [36]. For the experimental conditions used here, which provide high throughput *in-situ* ThT kinetic data (Figure 4.5 A, and experimental section), aggregation is thought to be promoted by P3. We previously validated the end point aggregate formed in this non-nucleation dependent growth process as amyloid by using Congo Red absorbance, Fourier transform infrared spectroscopy, and AFM [110].

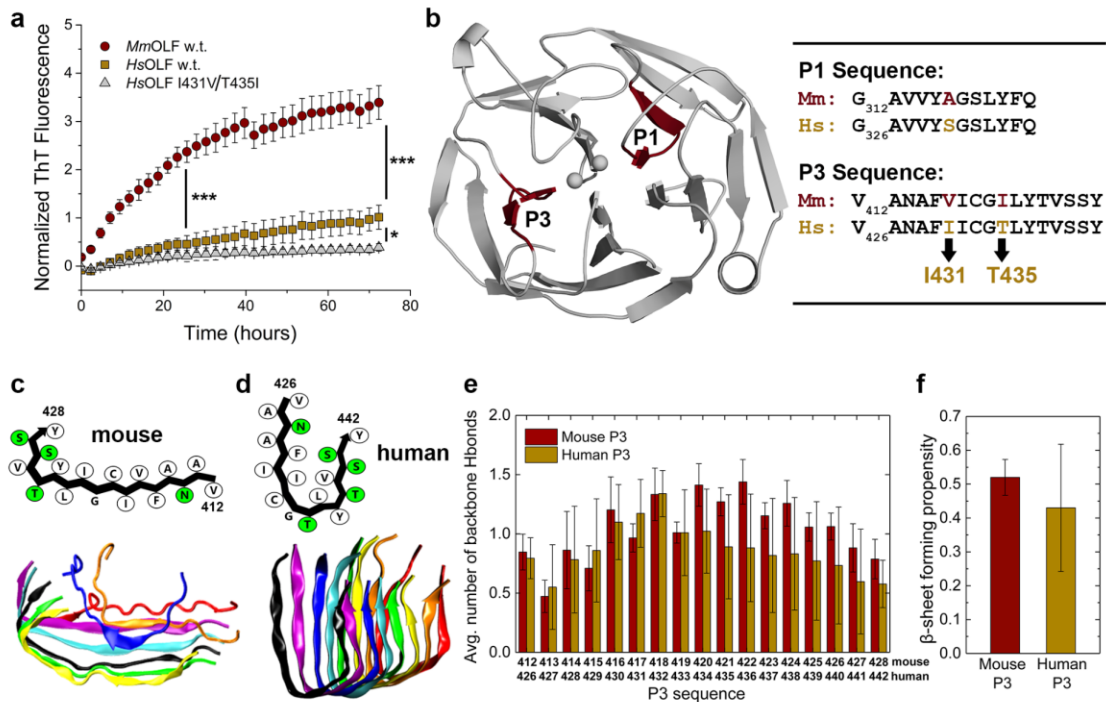


Figure 4.5 *MmOLF* aggregation kinetics, and DMD/PRIME20 simulations of amyloidogenic mouse P3. (A) Aggregation of purified *MmOLF*, *HsOLF* and *HsOLF* variant I431V/T435I monitored by ThT fluorescence at 42 °C over 72 hours; * ($p < 0.01$) and *** ($p < 0.0001$) represent statistically significant differences relative to *HsOLF* at 24h and 72h. (B) Location of amyloidogenic stretches P1 and P3 within the OLF domain (left), and sequence alignment of mouse and human P1 and P3 (right). (C) Simulated L-shaped mouse P3 protofilament in schematic representation (above) with hydrophobic and polar residues indicated in white and green, respectively, and representative final simulation snapshot (below). (D) Simulated U-shaped conformation of human P3 protofilament in schematic representation (above) and representative final simulation snapshot (below). (E) Average number of interpeptide backbone hydrogen bonds (H-bonds) formed per residue and (F) average β -sheet propensities calculated for human and mouse P3 peptides. All error bars represent standard deviation.

To test whether differences in aggregation propensity between *Hs*OLF and *Mm*OLF might originate in sequence differences in respective P1 (Ala to Ser) or P3 (Ile to Val, Thr to Leu) regions (Figure 4.5 B), we first turned to coarse grain molecular modeling using DMD/PRIME20, a method we used recently to simulate aggregation of P1 and P3 peptides derived from *Hs*OLF [110]. For P1, no obvious differences were identified between mouse and human P1 aggregation simulations (Figure 4.6, Figure 4.7), consistent with the single conservative substitution. By contrast, mouse P3 peptides, initially in random coil configurations, aggregate to form a parallel, in-register protofilament with a predominantly L-shaped backbone conformation in eight out of ten runs (Figure 4.5 C, Figure 4.8), a different shape and a more homogeneous aggregate compared to human P3, which formed a U-shaped backbone conformation in just two out of ten runs (Figure 4.5 D) [110]. Based on the average number of inter-peptide hydrogen bonds formed per residue calculated over the last third of the simulation trajectories (Figure 4.5 E), the two different residues, Val417 and Ile421 (corresponding to human residues Ile431 and Thr435), result in higher average β -sheet-forming propensity in the C-terminal region of the peptide and less variability than for human P3. The average β values or amyloid forming propensities for the entire peptide sequence are $\beta(\text{mouse P3}) = 0.52 \pm 0.05$, and $\beta(\text{human P3}) = 0.43 \pm 0.19$, suggesting that mouse P3 has a stronger amyloid forming propensity than human P3 (Figure 4.5 F). These differences do not reach statistical significance ($p < 0.0985$ by normal distribution test), likely due to the heterogeneous conformational landscape of simulated human P3 aggregates, but in principle suggest variations in P3 may explain experimental differences in kinetics between *Mm*OLF and *Hs*OLF.

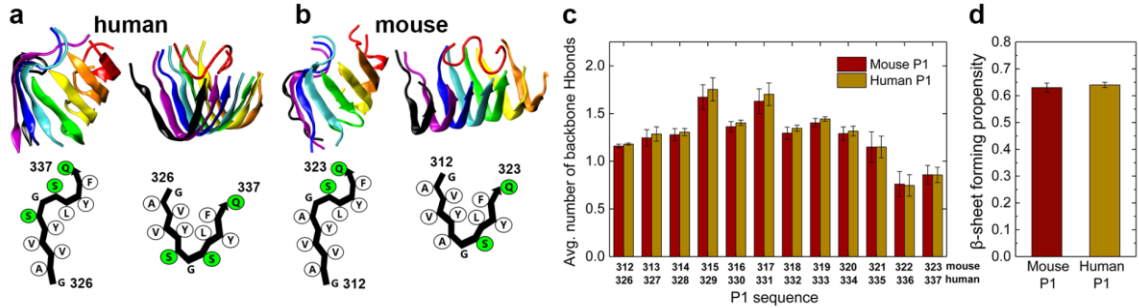


Figure 4.6 Representative simulation results, schematic representations, and analysis of the dominant morphologies of human P1 and mouse P1 aggregates. (A) human P1 (B) mouse P1. Green amino acids are hydrophilic. (C) Average number of interpeptide backbone hydrogen bonds (H-bonds) formed per residue, numbered according to *HsOLF*, and (D) average β -sheet propensities calculated for human and mouse P1 peptides.

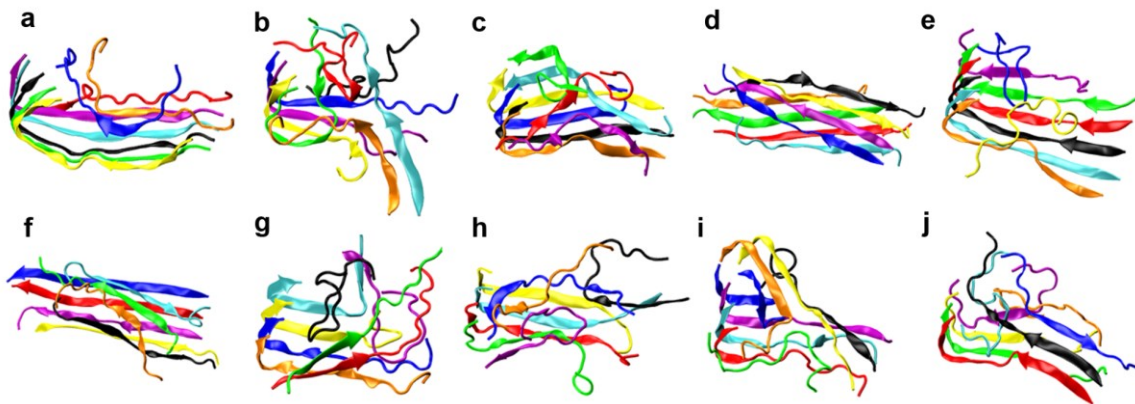


Figure 4.7 Simulation snapshots (A-J) of mouse P1 aggregates from ten independent DMD simulations after 220 μ s.

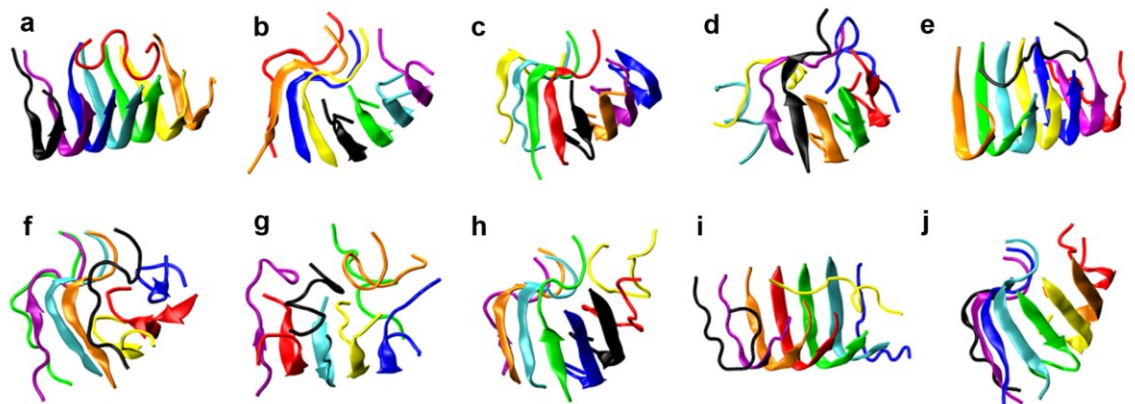


Figure 4.8 Simulation snapshots (A-J) of mouse P1 aggregates from ten independent DMD simulations after 220 μ s.

To experimentally evaluate whether the two amino acid differences in mouse P3 sequence account for more facile *MmOLF* aggregation, the double *HsOLF* variant Ile431Val/Thr435Ile was generated and subjected to an aggregation assay, in parallel with wild type *HsOLF* and *MmOLF* (Figure 4.5 A). Surprisingly, aggregation kinetics were more similar to *HsOLF* than to *MmOLF*, indicating that the specific residues in the mouse P3 sequence are not sufficient to increase *MmOLF* aggregation rates or increase ThT binding of the end-point aggregate. Differences between *HsOLF* wild type and the Ile431Val/Thr435Ile variant were not statistically significant at 24 hours ($p = 0.1645$), though they were at 72 hours ($p = 0.0074$, ANOVA). From this study, we infer that other sequence differences, scattered throughout the rest of the *MmOLF* domain, facilitate changes in the aggregation properties relative to *HsOLF*.

4.4.4 End-point aggregate morphologies of *MmOLF* and *HsOLF*.

Although sequence differences in P3 do not fully explain differing aggregation kinetics of *HsOLF* and *MmOLF*, cgMD results suggest structural differences in the aggregate at the molecular level. To determine whether these structural changes translate into a detectable morphological difference, the end-point aggregates were imaged by AFM. Both *MmOLF* and *HsOLF* samples show flat spherical oligomers ~ 6 nm in height and 1-2 μm in diameter (Figure 4.9). These species are similar in height, diameter, and circular morphology to our previous results for *HsOLF* using the same assay [36]. Still, the aggregates observed in these images are not identical. In the *MmOLF* sample there are additional curvilinear aggregates of varying length with similar height (~ 6 nm) to the spherical oligomers. The background of the *HsOLF* is more pronounced than that of *MmOLF*, perhaps suggesting long-lived smaller oligomeric species. Further studies, such

as AFM studies at different time points during aggregation, and systematic changes to the deposition surface, would be required to delineate the statistical significance of these differences.

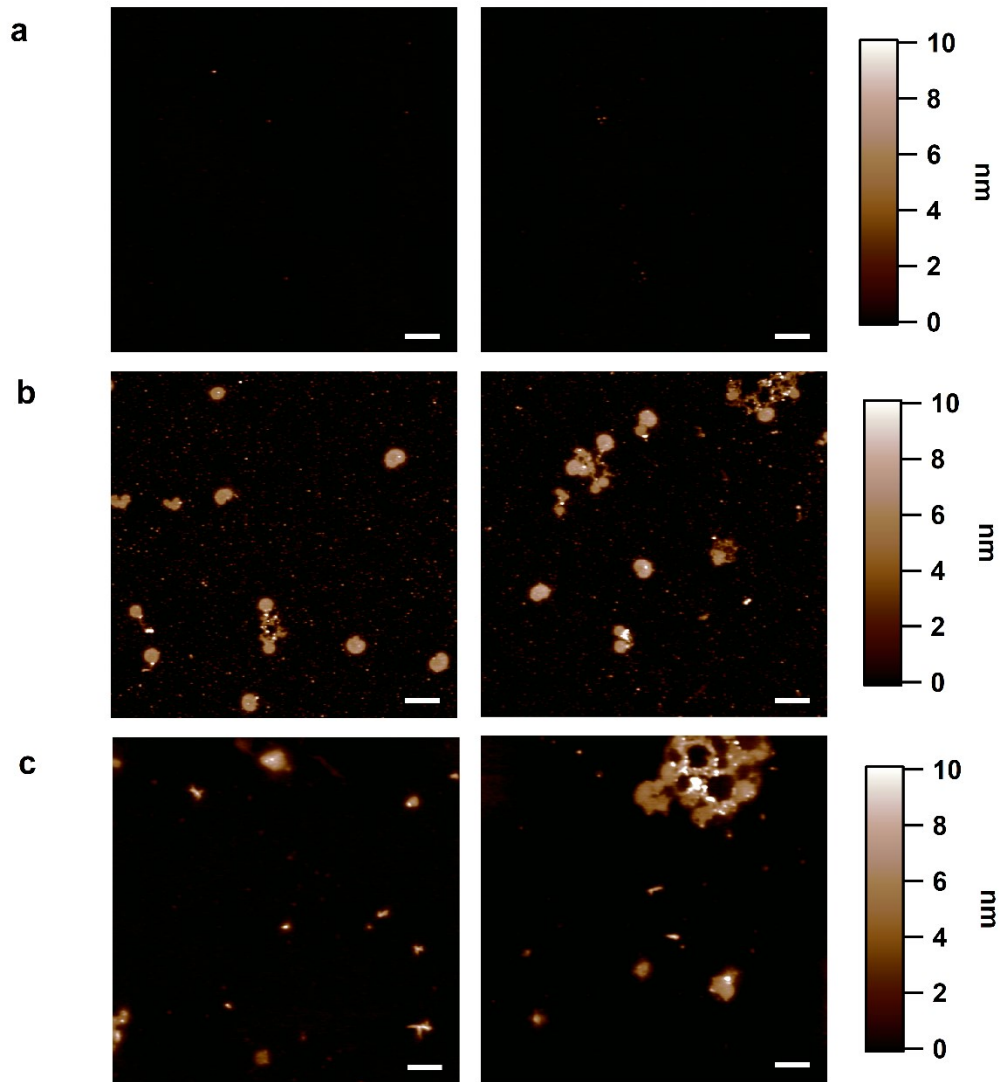


Figure 4.9 End-point aggregate morphologies of *MmOLF* and *HsOLF*. (A-C) Atomic force microscopy height imaging of samples post ThT aggregation confirm (A) a lack of aggregates in ThT-containing buffer control, while (B) *HsOLF* reveals spherical and curvilinear aggregates similar to (C) *MmOLF*. All images have a scale bar of 2 μm and were acquired using the same AFM tip.

4.5 DISCUSSION

Myocilin-associated glaucoma resembles other amyloid diseases like Alzheimer [119] in that numerous genetic mutations lead to a similar disease phenotype [92, 93]. From other well-studied amyloid systems, we know that specific amino acid substitutions, including naturally-occurring variants across species [120, 121] and disease-associated mutations [122-124], can lead to drastic changes in amyloid morphology and structural composition relevant to the severity of disease phenotypes. On the other hand, amyloid-forming stretches with limited sequence similarity often exhibit similar aggregate structures [125], underscoring the complexity of biophysical principles underlying amyloid formation.

In the case of myocilin, non-synonymous mutations in *HsOLF* result in a non-native protein that recruits properly folded myocilin into a template-assisted amyloid aggregation process [36, 37], leading to cell stress and death [13, 126-128]. In vitro, modifying parameters such as elevated temperature, low pH, slow agitation, and redox manipulation also access a partially-folded state of wild-type *HsOLF*, which in turn facilitates fibrilization [36, 37]. Other animals with similar eye anatomy to humans [82] and mutations in the myocilin gene (*e.g.* monkey [129]) do not develop glaucoma, and robust phenotypes are not readily induced in mice [97, 99], prompting us to consider the possibility that myocilin homologs exhibit biophysical features that protect against aggregation or facilitate cellular degradation of aggregates.

Previously, the leading explanation for the weak phenotype for mouse myocilin involved a putative cytosolic peroxisomal targeting sequence unique to *HsOLF*, proposed

to be exposed only upon misfolding [130]. *Hs*OLF structures, however, reveal that the far C-terminal end of native *Hs*OLF containing the suspected obscured signal sequence extends beyond the β -propeller structural domain, in a fully solvent-accessible conformation in the native state [8], so the sequence is not hidden. Another proposed culprit for varied glaucoma phenotypes across murine myocilin glaucoma models is genetic background. Genetics are known to play an important role in eliciting a glaucoma phenotype in DBA/2J mice, which are predisposed to severe ocular-hypertension and RGC death [131]. Genetic backgrounds vary among the mice used to generate the currently available myocilin glaucoma mouse models, and could modulate phenotype severity [82, 131]. Notably, adenovirus-induced overexpression of human Tyr437His myocilin resulted in elevated IOP in A/J, BALB/cJ and C57BL/6J mice, but not in C3H/HeJ mice [132]. Finally, mutant myocilin expression levels may influence resultant phenotypes. High expression appears important for an IOP elevation phenotype in available myocilin glaucoma mouse models. TM cells, like neurons, are long-lived and highly sensitive to protein misfolding, and may not require high levels of mutant myocilin to present aberrant phenotypes, but myocilin is present at relatively high concentrations in the cellular secretion studies [133-135] as well as in our experiments. Whether mutant myocilin overexpression is a general phenotype among myocilin glaucoma patients is currently unclear, but a recent histological analysis of a very rare sample of a glaucomatous donor eye harboring Tyr437His myocilin appears to support the finding that overexpression of mutant myocilin (relative to wild type levels in control eyes) is a factor [136].

Our characterization of *Mm*OLF structure and aggregation in this study, combined with prior cellular secretion studies demonstrating intracellular accumulation of selected

mouse myocilin variants [133] to an extent similar to human disease-causing counterparts [12, 55], would predict a robust aggregation phenotype upon mutation in mouse. Namely, even though native structure and thermal stability are relatively unchanged, *Mm*OLF aggregation kinetics are faster than *Hs*OLF, which cannot be adequately explained by the two hydrophobic alterations found in the mouse P3 sequence. Increased ThT fluorescence seen for *Mm*OLF could be attributed to charge or structural differences in the aggregate species [137]. Thus, one molecular level insight from our study is that differential surface electrostatics could be altering the aggregation profile of *Mm*OLF. Compared to the largely negative *Hs*OLF surface (calculated pI 5.0), the somewhat more neutral and varied *Mm*OLF (calculated pI 5.8) is expected to exhibit faster initial aggregation, as seen in systematic studies of other model amyloid systems [138, 139]. Another molecular explanation could be the relative toxicity of the aggregates. There is an overall resemblance in endpoint morphology for *Mm*OLF and *Hs*OLF aggregates, but we know from other amyloid diseases that the intermediate aggregates are likely the neurotoxic species, not the final endpoint aggregate [140, 141]. Perhaps by aggregating more quickly, the putatively more toxic intermediate in *Mm*OLF does not have time to populate, and instead is driven to the less toxic endpoint aggregate. Since OLF is a relatively new addition to the amyloids, details of such intermediates including their structure and toxicity, as well as aggregation of OLF when tethered to a coiled-coil region by a long linker [9], remain open questions. Taken together, our findings motivate further work into dissecting the factors that elicit glaucoma in mice, to further support their use in glaucoma research.

CHAPTER 5. FUTURE DIRECTIONS.

5.1 Introduction.

This thesis encompasses advancements in 1) our understanding of popular commercial myocilin antibodies currently used as community standards, 2) the development of new, conformational antibodies to N-terminal myocilin and 3) the biophysical characterization of the mouse OLF domain which, alongside that of its human counterpart, and is a prerequisite to further OLF-targeted antibody development. Each of these studies is supported by prior developments in our structural understanding of myocilin itself and in *in-vitro* antibody selection and development technologies, and constitutes an exciting stepping stone for future research. These new antibodies are specifically tailored to address long-standing questions regarding myocilin function and dysfunction including identifying functional binding partners, post-translational modifications, and their contextual changes due to glaucoma. Does myocilin aggregate in the ECM after secretion and perhaps play a role in normal TM aging? Is *in-vivo* imaging of myocilin aggregates a feasible means of detecting glaucoma pathology prior to vision loss? And finally, is myocilin tractable for antibody therapeutics aimed at limiting the formation and accumulation of toxic aggregates?

5.2 Optimization of Existing Antibodies.

My thesis details the development of antibodies targeting N-terminal myocilin that possess a range of conformational specificity and cross-reactivity to mouse myocilin. Currently, the LZ-targeting IgGs 2A4 and 1G12 display strong affinity and cross-reactivity,

but the CC-targeting IgGs exhibit weaker affinity, less conformational specificity, and poor cross-reactivity to mouse. These attributes could be improved upon by 1) conducting additional immunizations with human CC₃₃₋₁₁₁ and its mouse equivalent, 2) *in-silico* affinity maturation or 3) *in-vitro* affinity maturation. Affinity maturation efforts are already underway, by our collaborators, to further increase the power of IgG 2A4 (conformational & LZ-targeting) in downstream applications. The optimized antibodies would be subjected to further characterization, including quantitative determination of binding affinity by surface plasmon resonance and application to further experiments, described in later sections.

5.3 Development of OLF-Targeting Antibodies.

Our collaborators in the Maynard lab have immunized mice with mouse and human OLF and extracted antibody libraries from their spleens in methods very similar to those described in Chapter 3. The existing commercial OLF antibody, besides lacking conformational specificity [35], exhibits weaker affinity relative to its N-terminal commercial counterparts. Therefore, initial panning of phage-displayed scFv antibody candidates should be conducted against folded and misfolded/denatured OLF to separately identify candidate conformational and linear antibodies with high affinity to mouse and human OLF. This approach is not an option for N-terminal myocilin domains as they unfold reversibly [9].

Based on high sequence conservation within the interior of the β -propeller across OLF family members [8], one concern is that new OLF antibodies may exhibit binding to other OLF domains – a feature previously observed of commercial myocilin and noelin

antibodies [57]. Candidate OLF antibodies should be tested against other OLF family members expressed in the eye: optimedin, latrophilin, photomedin [142] and noelin [143]. Importantly, optimedin is known to colocalize with myocilin within the trabecular meshwork [144]. While noelin OLF can be produced by *E. coli* expression [57], mammalian cell expression of other OLF domains will be required.

5.4 Anticipated Applications of New Antibodies

5.4.1 Diagnostic and Therapeutic Applications of OLF Antibodies

While the development of conformational antibodies specific to human and mouse myocilin will allow us to pull down folded myocilin to access N-terminal binding partners and to specifically track folded OLF domains in tissue samples, antibodies targeting specific misfolded OLF conformations are also of interest as potential diagnostics and therapeutics. Since glaucoma is largely painless and progresses gradually, an important clinical concern is finding means of detecting abnormalities prior to the onset of severe retinal and optic nerve damage [145]. It is estimated that by the time vision loss is observed, approximately 40% of RGCs are already dead [146], loss that could be prevented or considerably slowed by early treatment. As a complement to detection of RGC death in the back of the eye [146], detection of aggregate myocilin deposits in the trabecular meshwork could provide an even earlier warning of glaucomatous pathology. Antibodies demonstrate great promise for *in-vivo* imaging as biologically inert, high affinity and tunable markers of diverse species [147]. Antibodies to amyloid-beta and tau, which detect Alzheimer's lesions *in-vivo* [148], provide exciting examples of diagnostic conformational antibodies currently under development for protein misfolding diseases. Similarly, circular and linear

fibril morphologies [36] and oligomers [37] of myocilin previously characterized by the Lieberman lab provide excellent targets for conformational antibody development.

Such antibodies may also have therapeutic applications if they can remove aggregated myocilin, an approach to treatment which has shown promise in other protein misfolding diseases. For example, a number of antibody therapeutics currently under development seek to bind amyloid-beta fibrils, quench fibril elongation and facilitate clearance of the fibrils and oligomers whose accumulation is associated with Alzheimer's disease progression [149]. Similarly, a structural understanding of the toxic forms of myocilin will guide a rational approach to arresting myocilin aggregation and enhancing aggregate clearance.

5.4.2 Identification of Functional Binding Partners.

Despite over twenty years of research there is no consensus as to the function of myocilin. Complicating this process is myocilin misfolding, which drives both self-aggregation and interactions with chaperones such as Grp94 [150]. However, as with other OLF family members, identifying binding partners is key to determining myocilin function within the trabecular meshwork. The oligomeric state of endogenous myocilin likely plays a key role in spacing myocilin domains and their interacting partners and in increasing the avidity of binding interactions – features which appear to have foiled our own attempts to identify binding partners using individual recombinant domains of myocilin.

The new N-terminal-targeting and future OLF-targeting myocilin antibodies offer an exciting solution to this problem through selective immunoprecipitation of well-folded endogenous myocilin from spent media of human trabecular meshwork cells. Such

antibodies should allow us to identify functional binding partners. Using multiple antibodies targeting different epitopes and domains within myocilin will help ensure that our antibodies are not excluding binding interactions to different regions of the protein. Additionally, these samples could be used to confirm myocilin post-translational modifications such as glycosylation, phosphorylation, and thereby gain insight into changes caused by the steroid and mechanical stress conditions associated with glaucoma.

5.4.3 Visualizing myocilin conformations in biological context.

Applying our antibodies to histology would allow tracking of multiple myocilin structural domains in various states of folding/misfolding in tissue samples. Of additional interest is detecting extracellular myocilin aggregates within the trabecular meshwork, which would indicate a role for myocilin the larger context of eye aging. Professor Lieberman is already in correspondence with experts in the broader glaucoma field who have professed interest in applying our antibodies to human and mouse tissues. Outside of gaining a more detailed picture of myocilin localization, these partnerships can give us key feedback to further improve our antibody reagents and will promote awareness of their availability throughout the broader glaucoma research community.

5.4.4 Obtaining high-resolution insight into N-terminal myocilin structure.

Fragments of these antibodies, e.g. Fab, could serve as crystallization chaperones to allow us to further elucidate the structure of N-terminal myocilin by X-ray crystallography. Of particular interest would to explicitly capture the Y-shaped tetrameric assembly formed by the myocilin's N-terminal coiled-coil and leucine zipper domains, including the N-terminal coiled-coil which so far have has eluded crystallization, lending

molecular level insight to the domain structure and the role of Cys47 and Cys61 disulfides. This structure could guide further antibody development (for example, as a potential starting point for *in-silico* affinity maturation of conformational CC-targeting antibodies), but also give additional structural insight into potential extracellular matrix interactions and/or the role of myocilin's coiled-coil domains.

5.5 Conclusion.

A modernized set of custom, recombinant conformational myocilin antibodies will help address broader concerns of antibody reproducibility and offer eye researchers a new set of tools to track myocilin. We anticipate that these antibodies will additionally help us to further characterize myocilin on a functional basis by helping to identify binding partners, and on a dysfunctional basis by differentially tracking various domains and conformations of myocilin. A deeper understanding of the role of myocilin within the trabecular meshwork will help shed light on the molecular-level workings of the trabecular meshwork and its role in maintaining stable ocular pressure.

REFERENCES

- [1] A. H. Coons, H. J. Creech, R. N. Jones, Immunological properties of an antibody containing a fluorescent group. *Proceedings of the Society for Experimental Biology and Medicine* **47**, 200-202 (1941).
- [2] D. M. Ecker, S. D. Jones, H. L. Levine, The therapeutic monoclonal antibody market. *MAbs* **7**, 9-14 (2015).
- [3] A. Bradbury, A. Pluckthun, Reproducibility: Standardize antibodies used in research. *Nature* **518**, 27-29 (2015).
- [4] F. Ferrara, S. D'Angelo, T. Gaiotto, L. Naranjo, H. Tian, S. Graslund, E. Dobrovetsky, P. Hraber, F. Lund-Johansen, S. Saragozza, D. Sblattero, C. Kiss, A. R. Bradbury, Recombinant renewable polyclonal antibodies. *MAbs* **7**, 32-41 (2015).
- [5] V. A. Meliopoulos, S. Schultz-Cherry, Although it's painful: The importance of stringent antibody validation. *PLoS Pathogens* **14**, e1006701 (2018).
- [6] A. R. Bradbury, A. Pluckthun, Getting to reproducible antibodies: the rationale for sequenced recombinant characterized reagents. *Protein Engineering Design & Selection* **28**, 303-305 (2015).
- [7] K. E. Keller, S. K. Bhattacharya, T. Borrás, T. M. Brunner, S. Chansangpetch, A. F. Clark, W. M. Dismuke, Y. Du, M. H. Elliott, C. R. Ethier, J. A. Faralli, T. F. Freddo, R. Fuchshofer, M. Giovingo, H. Gong, P. Gonzalez, A. Huang, M. A. Johnstone, P. L. Kaufman, M. J. Kelley, P. A. Knepper, C. C. Kocczynski, J. G. Kuchtey, R. W. Kuchtey, M. H. Kuehn, R. L. Lieberman, S. C. Lin, P. Liton, Y. Liu, E. Lutjen-Drecoll, W. Mao, M. Masis-Solano, F. McDonnell, C. M. McDowell, D. R. Overby, P. P. Pattabiraman, V. K. Raghunathan, P. V. Rao, D. J. Rhee, U. R. Chowdhury, P. Russell, J. R. Samples, D. Schwartz, E. B. Stubbs, E. R. Tamm, J. C. Tan, C. B. Toris, K. Y. Torrejon, J. A. Vranka, M. K. Wirtz, T. Yorio, J. Zhang, G. S. Zode, M. P. Fautsch, D. M. Peters, T. S. Acott, W. D. Stamer, Consensus recommendations for trabecular meshwork cell isolation, characterization and culture. *Exp Eye Res* **171**, 164-173 (2018).
- [8] R. K. Donegan, S. E. Hill, D. M. Freeman, E. Nguyen, S. D. Orwig, K. C. Turnage, R. L. Lieberman, Structural basis for misfolding in myocilin-associated glaucoma. *Human Molecular Genetics* **24**, 2111-2124 (2015).
- [9] S. E. Hill, E. Nguyen, R. K. Donegan, A. C. Patterson-Orazem, A. Hazel, J. C. Gumbart, R. L. Lieberman, Structure and misfolding of the flexible tripartite coiled-coil domain of glaucoma-associated myocilin. *Structure* **25**, 1697-1707 (2017).
- [10] E. M. Stone, J. H. Fingert, W. L. M. Alward, T. D. Nguyen, J. R. Polansky, S. L. F. Sunden, D. Nishimura, A. F. Clark, A. Nystuen, B. E. Nichols, D. A. Mackey,

- R. Ritch, J. W. Kalenak, E. R. Craven, V. C. Sheffield, Identification of a gene that causes primary open angle glaucoma. *Science* **275**, 668-670 (1997).
- [11] H. A. Quigley, A. T. Broman, The number of people with glaucoma worldwide in 2010 and 2020. *Br J Ophthalmol* **90**, 262-267 (2006).
- [12] J. N. Burns, K. C. Turnage, C. A. Walker, R. L. Lieberman, The stability of myocilin olfactomedin domain variants provides new insight into glaucoma as a protein misfolding disorder. *Biochemistry* **50**, 5824-5833 (2011).
- [13] Y. Liu, D. Vollrath, Reversal of mutant myocilin non-secretion and cell killing: implications for glaucoma. *Human Molecular Genetics* **13**, 1193-1204 (2004).
- [14] N. Jacobson, M. Andrews, A. R. Shepard, D. Nishimura, C. Searby, J. H. Fingert, G. Hageman, R. Mullins, B. L. Davidson, Y. H. Kwon, W. L. Alward, E. M. Stone, A. F. Clark, V. C. Sheffield, Non-secretion of mutant proteins of the glaucoma gene myocilin in cultured trabecular meshwork cells and in aqueous humor. *Hum. Mol. Genet.* **10**, 117-125 (2001).
- [15] A. Suntharalingam, J. F. Abisambra, J. C. O'Leary, 3rd, J. Koren, 3rd, B. Zhang, M. K. Joe, L. J. Blair, S. E. Hill, U. K. Jinwal, M. Cockman, A. S. Duerfeldt, S. Tomarev, B. S. Blagg, R. L. Lieberman, C. A. Dickey, Glucose-regulated protein 94 triage of mutant myocilin through endoplasmic reticulum-associated degradation subverts a more efficient autophagic clearance mechanism. *J. Biol. Chem.* **287**, 40661-40669 (2012).
- [16] M. K. Joe, S. Sohn, W. Hur, Y. Moon, Y. R. Choi, C. Kee, Accumulation of mutant myocilins in ER leads to ER stress and potential cytotoxicity in human trabecular meshwork cells. *Biochem. Biophys. Res. Commun.* **312**, 592-600 (2003).
- [17] G. H. Yam, K. Gaplovska-Kysela, C. Zuber, J. Roth, Aggregated myocilin induces russell bodies and causes apoptosis: implications for the pathogenesis of myocilin-caused primary open-angle glaucoma. *Am. J. Pathol.* **170**, 100-109 (2007).
- [18] G. S. Zode, M. H. Kuehn, D. Y. Nishimura, C. C. Searby, K. Mohan, S. D. Grozdanic, K. Bugge, M. G. Anderson, A. F. Clark, E. M. Stone, V. C. Sheffield, Reduction of ER stress via a chemical chaperone prevents disease phenotypes in a mouse model of primary open angle glaucoma. *Journal of Clinical Investigation* **121**, 3542-3553 (2011).
- [19] J. Kanagavalli, P. J. Pandaranayaka, S. R. Krishnadas, S. Krishnaswamy, P. Sundaresan, In vitro and in vivo study on the secretion of the Gly367Arg mutant myocilin protein. *Mol. Vis.* **13**, 1161-1168 (2007).
- [20] L. Wang, Y. Zhuo, B. Liu, S. Huang, F. Hou, J. Ge, Pro370Leu mutant myocilin disturbs the endoplasm reticulum stress response and mitochondrial membrane potential in human trabecular meshwork cells. *Mol. Vis.* **13**, 618-625 (2007).

- [21] R. R. Anholt, M. A. Carbone, A molecular mechanism for glaucoma: endoplasmic reticulum stress and the unfolded protein response. *Trends Mol. Med.* **19**, 586-593 (2013).
- [22] J. L. Wiggs, R. R. Allingham, D. Vollrath, K. H. Jones, M. De La Paz, J. Kern, K. Patterson, V. L. Babb, E. A. Del Bono, B. W. Broomer, M. A. Pericak-Vance, J. L. Haines, Prevalence of mutations in TIGR/Myocilin in patients with adult and juvenile primary open-angle glaucoma. *American Journal of Human Genetics* **63**, 1549-1552 (1998).
- [23] W. D. Stamer, A. F. Clark, The many faces of the trabecular meshwork cell. *Exp. Eye Res.* **158**, 112-123 (2017).
- [24] A. J. Kole, R. P. Annis, M. Deshmukh, Mature neurons: equipped for survival. *Cell Death Dis.* **4**, e689 (2013).
- [25] M. Bucciantini, E. Giannoni, F. Chiti, F. Baroni, L. Formigli, J. Zurdo, N. Taddei, G. Ramponi, C. M. Dobson, M. Stefani, Inherent toxicity of aggregates implies a common mechanism for protein misfolding diseases. *Nature* **416**, 507-511 (2002).
- [26] F. U. Hartl, Protein Misfolding Diseases. *Annual Review of Biochemistry* **86**, 21-26 (2017).
- [27] T. D. Nguyen, P. Chen, W. D. Huang, H. Chen, D. Johnson, J. R. Polansky, Gene structure and properties of TIGR, an olfactomedin-related glycoprotein cloned from glucocorticoid-induced trabecular meshwork cells. *Journal of Biological Chemistry* **273**, 6341-6350 (1998).
- [28] L. E. Cheng, J. Ueda, K. Wentz-Hunter, B. Y. J. T. Yue, Age independent expression of myocilin in the human trabecular meshwork. *International Journal of Molecular Medicine* **10**, 33-40 (2002).
- [29] A. R. Shepard, N. Jacobson, R. F. Sui, H. T. Steely, A. J. Lotery, E. M. Stone, A. F. Clark, Characterization of rabbit myocilin: Implications for human myocilin glycosylation and signal peptide usage. *BMC Genetics* **4**, 1-10 (2003).
- [30] D. B. Gould, L. Miceli-Libby, O. V. Savinova, M. Torrado, S. I. Tomarev, R. S. Smith, S. W. John, Genetically increasing Myoc expression supports a necessary pathologic role of abnormal proteins in glaucoma. *Mol Cell Biol* **24**, 9019-9025 (2004).
- [31] E. Lutjen-Drecoll, C. A. May, J. R. Polansky, D. H. Johnson, H. Bloemendal, T. D. Nguyen, Localization of the stress proteins alpha B-crystallin and trabecular meshwork inducible glucocorticoid response protein in normal and glaucomatous trabecular meshwork. *Invest. Ophthalmol. Vis. Sci.* **39**, 517-525 (1998).
- [32] T. D. Nguyen, P. Chen, W. D. Huang, H. Chen, D. Johnson, J. R. Polansky, Gene structure and properties of TIGR, an olfactomedin-related glycoprotein cloned from

- glucocorticoid-induced trabecular meshwork cells. *J. Biol. Chem.* **273**, 6341-6350 (1998).
- [33] A. M. Anderssohn, K. Cox, K. O'Malley, S. Dees, M. Hosseini, L. Boren, A. Wagner, J. M. Bradley, M. J. Kelley, T. S. Acott, Molecular chaperone function for myocilin. *Investigative Ophthalmology & Visual Science* **52**, 7548-7555 (2011).
- [34] M. K. Ezzat, K. G. Howell, C. K. Bahler, T. G. Beito, N. Loewen, E. M. Poeschla, M. P. Fautsch, Characterization of monoclonal antibodies against the glaucoma-associated protein myocilin. *Experimental Eye Research* **87**, 376-384 (2008).
- [35] A. C. Patterson-Orazem, S. E. Hill, M. P. Fautsch, R. L. Lieberman, Epitope mapping of commercial antibodies that detect myocilin. *Experimental Eye Research* **173**, 109-112 (2018).
- [36] S. E. Hill, R. K. Donegan, R. L. Lieberman, The glaucoma-associated olfactomedin domain of myocilin forms polymorphic fibrils that are constrained by partial unfolding and peptide sequence. *Journal of Molecular Biology* **426**, 921-935 (2014).
- [37] S. D. Orwig, C. W. Perry, L. Y. Kim, K. C. Turnage, R. Zhang, D. Vollrath, I. Schmidt-Krey, R. L. Lieberman, Amyloid fibril formation by the glaucoma-associated olfactomedin domain of myocilin. *Journal of Molecular Biology* **421**, 242-255 (2012).
- [38] M. P. Fautsch, A. M. Vrabel, S. L. Peterson, D. H. Johnson, In vitro and in vivo characterization of disulfide bond use in myocilin complex formation. *Molecular Vision* **10**, 417-425 (2004).
- [39] S. Gobeil, M. A. Rodrigue, S. Moisan, T. D. Nguyen, J. R. Polansky, J. Morissette, V. Raymond, Intracellular sequestration of hetero-oligomers formed by wild-type and glaucoma-causing myocilin mutants. *Investigative Ophthalmology & Visual Science* **45**, 3560-3567 (2004).
- [40] F. Sanchez-Sanchez, F. Martinez-Redondo, J. D. Aroca-Aguilar, M. Coca-Prados, J. Escribano, Characterization of the intracellular proteolytic cleavage of myocilin and identification of calpain II as a myocilin-processing protease. *Journal of Biological Chemistry* **282**, 27810-27824 (2007).
- [41] J. P. Silva, V. Lelianova, C. Hopkins, K. E. Volynski, Y. Ushkaryov, Functional cross-interaction of the fragments produced by the cleavage of distinct adhesion G-protein-coupled receptors. *Journal of Biological Chemistry* **284**, 6495-6506 (2009).
- [42] Y. Eshed, K. Feinberg, D. J. Carey, E. Peles, Secreted gliomedin is a perinodal matrix component of peripheral nerves. *Journal of Cell Biology* **177**, 551-562 (2007).

- [43] B. Maertens, D. Hopkins, C. W. Franzke, D. R. Keene, L. Bruckner-Tuderman, D. S. Greenspan, M. Koch, Cleavage and oligomerization of gliomedin, a transmembrane collagen required for node of Ranvier formation. *Journal of Biological Chemistry* **282**, 10647-10659 (2007).
- [44] Y. C. Lu, O. V. Nazarko, R. Sando, 3rd, G. S. Salzman, N. S. Li, T. C. Sudhof, D. Arac, Structural Basis of Latrophilin-FLRT-UNC5 Interaction in Cell Adhesion. *Structure* **23**, 1678-1691 (2015).
- [45] G. Kohler, C. Milstein, Continuous cultures of fused cells secreting antibody of predefined specificity. *Nature* **256**, 495-497 (1975).
- [46] J. Bordeaux, A. Welsh, S. Agarwal, E. Killiam, M. Baquero, J. Hanna, V. Anagnostou, D. Rimm, Antibody validation. *Biotechniques* **48**, 197-209 (2010).
- [47] B. Hjelm, B. Forsstrom, J. Lofblom, J. Rockberg, M. Uhlen, Parallel immunizations of rabbits using the same antigen yield antibodies with similar, but not identical, epitopes. *PLoS One* **7**, e45817 (2012).
- [48] P. Nilsson, L. Paavilainen, K. Larsson, J. Odling, M. Sundberg, A. C. Andersson, C. Kampf, A. Persson, C. A. K. Szigyarto, J. Ottosson, E. Bjorling, S. Hober, H. Wernerus, K. Wester, F. Ponten, M. Uhlen, Towards a human proteome atlas: High-throughput generation of mono-specific antibodies for tissue profiling. *Proteomics* **5**, 4327-4337 (2005).
- [49] N. S. Lipman, L. R. Jackson, L. J. Trudel, F. Weis-Garcia, Monoclonal versus polyclonal antibodies: distinguishing characteristics, applications, and information resources. *ILAR Journal* **46**, 258-268 (2005).
- [50] C. G. Begley, L. M. Ellis, Drug development: Raise standards for preclinical cancer research. *Nature* **483**, 531-533 (2012).
- [51] J. R. Polansky, D. J. Fauss, P. Chen, H. Chen, E. Lutjen-Drecoll, D. Johnson, R. M. Kurtz, Z. D. Ma, E. Bloom, T. D. Nguyen, Cellular pharmacology and molecular biology of the trabecular meshwork inducible glucocorticoid response gene product. *Ophthalmologica* **211**, 126-139 (1997).
- [52] W. D. Stamer, A. F. Clark, The many faces of the trabecular meshwork cell. *Experimental Eye Research* **158**, 112-123 (2017).
- [53] J. R. Polansky, D. J. Fauss, C. C. Zimmerman, Regulation of TIGR/MYOC gene expression in human trabecular meshwork cells. *Eye* **14**, 503-514 (2000).
- [54] S. Sohn, M. K. Joe, T. E. Kim, J. E. Im, Y. R. Choi, H. Park, C. Kee, Dual localization of wild-type myocilin in the endoplasmic reticulum and extracellular compartment likely occurs due to its incomplete secretion. *Molecular Vision* **15**, 545-556 (2009).

- [55] J. N. Burns, S. D. Orwig, J. L. Harris, J. D. Watkins, D. Vollrath, R. L. Lieberman, Rescue of glaucoma-causing mutant myocilin thermal stability by chemical chaperones. *ACS Chemical Biology* **5**, 477-487 (2010).
- [56] E. J. Snider, R. T. Vannatta, L. Schildmeyer, W. D. Stamer, C. R. Ethier, Characterizing differences between MSCs and TM cells: Toward autologous stem cell therapies for the glaucomatous trabecular meshwork. *Journal of Tissue Engineering and Regenerative Medicine*, 1-10 (2017).
- [57] S. E. Hill, R. K. Donegan, E. Nguyen, T. M. Desai, R. L. Lieberman, Molecular details of olfactomedin domains provide pathway to structure-function studies. *PLoS One* **10**, (2015).
- [58] A. F. Saeed, R. Wang, S. Ling, S. Wang, Antibody Engineering for Pursuing a Healthier Future. *Front Microbiol* **8**, 495 (2017).
- [59] J. M. Perchiacca, A. R. Ladiwala, M. Bhattacharya, P. M. Tessier, Structure-based design of conformation- and sequence-specific antibodies against amyloid beta. *Proc Natl Acad Sci U S A* **109**, 84-89 (2012).
- [60] E. De Genst, A. Messer, C. M. Dobson, Antibodies and protein misfolding: From structural research tools to therapeutic strategies. *Biochim Biophys Acta* **1844**, 1907-1919 (2014).
- [61] V. V. Kapetanakis, M. P. Chan, P. J. Foster, D. G. Cook, C. G. Owen, A. R. Rudnicka, Global variations and time trends in the prevalence of primary open angle glaucoma (POAG): a systematic review and meta-analysis. *Br J Ophthalmol* **100**, 86-93 (2016).
- [62] J. H. Fingert, E. M. Stone, V. C. Sheffield, W. L. Alward, Myocilin glaucoma. *Surv Ophthalmol* **47**, 547-561 (2002).
- [63] Y. H. Kwon, J. H. Fingert, M. H. Kuehn, W. L. Alward, Primary open-angle glaucoma. *N Engl J Med* **360**, 1113-1124 (2009).
- [64] E. R. Tamm, P. Russell, D. L. Epstein, D. H. Johnson, J. Piatigorsky, Modulation of myocilin/TIGR expression in human trabecular meshwork. *Invest Ophthalmol Vis Sci* **40**, 2577-2582 (1999).
- [65] K. E. Keller, S. K. Bhattacharya, T. Borrás, T. M. Brunner, S. Chansangpetch, A. F. Clark, W. M. Dismuke, Y. Du, M. H. Elliott, C. R. Ethier, J. A. Faralli, T. F. Freddo, R. Fuchshofer, M. Giovingo, H. Gong, P. Gonzalez, A. Huang, M. A. Johnstone, P. L. Kaufman, M. J. Kelley, P. A. Knepper, C. C. Kopczynski, J. G. Kuchtey, R. W. Kuchtey, M. H. Kuehn, R. L. Lieberman, S. C. Lin, P. Liton, Y. Liu, E. Lutjen-Drecoll, W. Mao, M. Masis-Solano, F. McDonnell, C. M. McDowell, D. R. Overby, P. P. Pattabiraman, V. K. Raghunathan, P. V. Rao, D. J. Rhee, U. R. Chowdhury, P. Russell, J. R. Samples, D. Schwartz, E. B. Stubbs, E. R. Tamm, J. C. Tan, C. B. Toris, K. Y. Torrejon, J. A. Vranka, M. K. Wirtz, T.

- Yorio, J. Zhang, G. S. Zode, M. P. Fautsch, D. M. Peters, T. S. Acott, W. D. Stamer, Consensus recommendations for trabecular meshwork cell isolation, characterization and culture. *Experimental Eye Research* **171**, 164-173 (2018).
- [66] F. Sanchez-Sanchez, F. Martinez-Redondo, J. D. Aroca-Aguilar, M. Coca-Prados, J. Escribano, Characterization of the intracellular proteolytic cleavage of myocilin and identification of calpain II as a myocilin-processing protease. *J. Biol. Chem.* **282**, 27810-27824 (2007).
- [67] A. Goldwich, C. R. Ethier, D. W. Chan, E. R. Tamm, Perfusion with the olfactomedin domain of myocilin does not affect outflow facility. *Invest Ophthalmol Vis Sci* **44**, 1953-1961 (2003).
- [68] S. T. Furlong, R. C. Mauger, A. M. Strimpler, Y. P. Liu, F. X. Morris, P. D. Edwards, Synthesis and physical characterization of a P1 arginine combinatorial library, and its application to the determination of the substrate specificity of serine peptidases. *Bioorg Med Chem* **10**, 3637-3647 (2002).
- [69] O. Schilling, U. auf dem Keller, C. M. Overall, Factor Xa subsite mapping by proteome-derived peptide libraries improved using WebPICS, a resource for proteomic identification of cleavage sites. *Biol Chem* **392**, 1031-1037 (2011).
- [70] A. Krebber, S. Bornhauser, J. Burmester, A. Honegger, J. Willuda, H. R. Bosshard, A. Pluckthun, Reliable cloning of functional antibody variable domains from hybridomas and spleen cell repertoires employing a reengineered phage display system. *J Immunol Methods* **201**, 35-55 (1997).
- [71] J. Maynard, E. J. Adams, M. Krogsgaard, K. Petersson, C. W. Liu, K. C. Garcia, High-level bacterial secretion of single-chain alphabeta T-cell receptors. *J Immunol Methods* **306**, 51-67 (2005).
- [72] K. Smith, L. Garman, J. Wrammert, N. Y. Zheng, J. D. Capra, R. Ahmed, P. C. Wilson, Rapid generation of fully human monoclonal antibodies specific to a vaccinating antigen. *Nat Protoc* **4**, 372-384 (2009).
- [73] C. A. Schneider, W. S. Rasband, K. W. Eliceiri, NIH Image to ImageJ: 25 years of image analysis. *Nat Methods* **9**, 671-675 (2012).
- [74] R. M. Ionescu, J. Vlasak, C. Price, M. Kirchmeier, Contribution of variable domains to the stability of humanized IgG1 monoclonal antibodies. *J Pharm Sci* **97**, 1414-1426 (2008).
- [75] R. Kaye, E. Head, J. L. Thompson, T. M. McIntire, S. C. Milton, C. W. Cotman, C. G. Glabe, Common structure of soluble amyloid oligomers implies common mechanism of pathogenesis. *Science* **300**, 486-489 (2003).
- [76] C. Ruffmann, N. Bengoa-Vergniory, I. Poggiolini, D. Ritchie, M. T. Hu, J. Alegre-Abarrategui, L. Parkkinen, Detection of alpha-synuclein conformational variants

from gastro-intestinal biopsy tissue as a potential biomarker for Parkinson's disease. *Neuropathol Appl Neurobiol* **44**, 722-736 (2018).

- [77] E. Croisier, M. R. DE, M. Deprez, K. Goldring, D. T. Dexter, R. K. Pearce, M. B. Graeber, F. Roncaroli, Comparative study of commercially available anti-alpha-synuclein antibodies. *Neuropathol Appl Neurobiol* **32**, 351-356 (2006).
- [78] J. N. Higaki, A. Chakrabartty, N. J. Galant, K. C. Hadley, B. Hammerson, T. Nijjar, R. Torres, J. R. Tapia, J. Salmans, R. Barbour, S. J. Tam, K. Flanagan, W. Zago, G. G. Kinney, Novel conformation-specific monoclonal antibodies against amyloidogenic forms of transthyretin. *Amyloid* **23**, 86-97 (2016).
- [79] R. Rakhit, J. Robertson, C. Vande Velde, P. Horne, D. M. Ruth, J. Griffin, D. W. Cleveland, N. R. Cashman, A. Chakrabartty, An immunological epitope selective for pathological monomer-misfolded SOD1 in ALS. *Nat Med* **13**, 754-759 (2007).
- [80] R. S. Atlasi, R. Malik, C. I. Corrales, L. Tzeplaeff, J. P. Whitelegge, N. R. Cashman, G. Bitan, Investigation of Anti-SOD1 Antibodies Yields New Structural Insight into SOD1 Misfolding and Surprising Behavior of the Antibodies Themselves. *ACS Chemical Biology* **13**, 2794-2807 (2018).
- [81] T. V. Johnson, S. I. Tomarev, Rodent models of glaucoma. *Brain Res Bull* **81**, 349-358 (2010).
- [82] T. V. Johnson, S. I. Tomarev, in *Animal Models of Ophthalmic Diseases*, C. Chan, Ed. (Springer International Publishing, Switzerland, 2016), pp. 31-49.
- [83] K. Changula, R. Yoshida, O. Noyori, A. Marzi, H. Miyamoto, M. Ishijima, A. Yokoyama, M. Kajihara, H. Feldmann, A. S. Mweene, A. Takada, Mapping of conserved and species-specific antibody epitopes on the Ebola virus nucleoprotein. *Virus Res* **176**, 83-90 (2013).
- [84] L. Westernberg, V. Schulten, J. A. Greenbaum, S. Natali, V. Tripple, D. M. McKinney, A. Frazier, H. Hofer, M. Wallner, F. Sallusto, A. Sette, B. Peters, T-cell epitope conservation across allergen species is a major determinant of immunogenicity. *J Allergy Clin Immunol* **138**, 571-578 e577 (2016).
- [85] M. P. Fautsch, D. H. Johnson, Characterization of myocilin-myocilin interactions. *Investigative Ophthalmology & Visual Science* **42**, 2324-2331 (2001).
- [86] W. D. Stamer, K. M. Perkumas, E. A. Hoffman, B. C. Roberts, D. L. Epstein, B. S. McKay, Coiled-coil targeting of myocilin to intracellular membranes. *Experimental Eye Research* **83**, 1386-1395 (2006).
- [87] A. Goyal, A. Srivastava, R. Sihota, J. Kaur, Evaluation of oxidative stress markers in aqueous humor of primary open angle glaucoma and primary angle closure glaucoma patients. *Curr Eye Res* **39**, 823-829 (2014).

- [88] I. Majsterek, K. Malinowska, M. Stanczyk, M. Kowalski, J. Blaszczyk, A. K. Kurowska, A. Kaminska, J. Szaflik, J. P. Szaflik, Evaluation of oxidative stress markers in pathogenesis of primary open-angle glaucoma. *Exp Mol Pathol* **90**, 231-237 (2011).
- [89] N. Reixach, T. R. Foss, E. Santelli, J. Pascual, J. W. Kelly, J. N. Buxbaum, Human-murine transthyretin heterotetramers are kinetically stable and non-amyloidogenic - A lesson in the generation of transgenic models of diseases involving oligomeric proteins. *Journal of Biological Chemistry* **283**, 2098-2107 (2008).
- [90] K. Ando, K. Leroy, C. Heraud, A. Kabova, Z. Yilmaz, M. Authelet, V. Suain, R. De Decker, J. P. Brion, Deletion of murine tau gene increases tau aggregation in a human mutant tau transgenic mouse model. *Biochemical Society Transactions* **38**, 1001-1005 (2010).
- [91] F. U. Hartl, M. Hayer-Hartl, Converging concepts of protein folding in vitro and in vivo. *Nature Structural & Molecular Biology* **16**, 574-581 (2009).
- [92] G. Gong, O. Kosoko-Lasaki, G. R. Haynatzki, M. R. Wilson, Genetic dissection of myocilin glaucoma. *Human Molecular Genetics* **13**, R91-102 (2004).
- [93] E. R. Tamm, Myocilin and glaucoma: facts and ideas. *Progress in Retinal & Eye Research* **21**, 395-428 (2002).
- [94] A. R. Stothert, S. N. Fontaine, J. J. Sabbagh, C. A. Dickey, Targeting the ER-autophagy system in the trabecular meshwork to treat glaucoma. *Experimental Eye Research* **144**, 38-45 (2016).
- [95] W. L. Alward, J. H. Fingert, M. A. Coote, A. T. Johnson, S. F. Lerner, D. Junqua, F. J. Durcan, P. J. McCartney, D. A. Mackey, V. C. Sheffield, E. M. Stone, Clinical features associated with mutations in the chromosome 1 open-angle glaucoma gene (GLC1A). *New England Journal of Medicine* **338**, 1022-1027 (1998).
- [96] J. H. Fingert, E. M. Stone, V. C. Sheffield, W. L. Alward, Myocilin glaucoma. *Survey of Ophthalmology* **47**, 547-561 (2002).
- [97] V. Senatorov, I. Malyukova, R. Fariss, E. F. Wawrousek, S. Swaminathan, S. K. Sharan, S. Tomarev, Expression of mutated mouse myocilin induces open-angle glaucoma in transgenic mice. *The Journal of Neuroscience* **26**, 11903-11914 (2006).
- [98] Y. Zhou, O. Grinchuk, S. I. Tomarev, Transgenic mice expressing the Tyr437His mutant of human myocilin protein develop glaucoma. *Investigative Ophthalmology & Visual Science* **49**, 1932-1939 (2008).
- [99] D. B. Gould, M. Reedy, L. A. Wilson, R. S. Smith, R. L. Johnson, S. W. M. John, Mutant myocilin nonsecretion in vivo is not sufficient to cause glaucoma. *Molecular Cell Biology* **26**, 8427-8436 (2006).

- [100] S. E. Hill, R. K. Donegan, R. L. Lieberman, The glaucoma-associated olfactomedin domain of myocilin forms polymorphic fibrils that are constrained by partial unfolding and peptide sequence. *J Mol Biol* **426**, 921-935 (2014).
- [101] J. E. Tropea, S. Cherry, D. S. Waugh, Expression and purification of soluble His(6)-tagged TEV protease. *Methods Mol. Biol.* **498**, 297-307 (2009).
- [102] E. Gasteiger, C. Hoogland, A. Gattiker, S. Duvaud, M. R. Wilkins, R. D. Appel, A. Bairoch, Protein Identification and Analysis Tools on the ExPASy Server. *The Proteomics Protocols Handbook*, 571-607 (2005).
- [103] W. Minor, M. Cymborowski, Z. Otwinowski, M. Chruszcz, HKL-3000: the integration of data reduction and structure solution - from diffraction images to an initial model in minutes. *Acta Crystallographica Section D-Biological Crystallography* **62**, 859-866 (2006).
- [104] A. J. McCoy, R. W. Grosse-Kunstleve, P. D. Adams, M. D. Winn, L. C. Storoni, R. J. Read, Phaser crystallographic software. *Journal of Applied Crystallography* **40**, 658-674 (2007).
- [105] P. Emsley, B. Lohkamp, W. G. Scott, K. Cowtan, Features and development of Coot. *Acta Crystallographica Section D-Biological Crystallography* **66**, 486-501 (2010).
- [106] L. Schrödinger, The PyMOL Molecular Graphics System, Version 2.0. (2015).
- [107] E. Jurrus, D. Engel, K. Star, K. Monson, J. Brandi, L. E. Felberg, D. H. Brookes, L. Wilson, J. Chen, K. Liles, M. Chun, P. Li, D. W. Gohara, T. Dolinsky, R. Konecny, D. R. Koes, J. E. Nielsen, T. Head-Gordon, W. Geng, R. Krasny, G. W. Wei, M. J. Holst, J. A. McCammon, N. A. Baker, Improvements to the APBS biomolecular solvation software suite. *Protein Science* **27**, 112-128 (2018).
- [108] W. T. Alder BJ, Studies in molecular dynamics I: general method. *The Journal of Chemical Physics*, 459-466 (1959).
- [109] A. Voegler Smith, C. K. Hall, Alpha-Helix Formation: discontinuous molecular dynamics on an intermediate-resolution protein model. *Proteins-Structure Function and Bioinformatics* **44**, 344-360 (2001).
- [110] Y. Wang, Y. Gao, S. E. Hill, D. J. E. Huard, M. O. Tomlin, R. L. Lieberman, A. K. Paravastu, C. K. Hall, Simulations and Experiments Delineate Amyloid Fibrilization by Peptides Derived from Glaucoma-Associated Myocilin. *Journal of Physical Chemistry B* **122**, 5845-5850 (2018).
- [111] M. Cheon, I. Chang, C. K. Hall, Extending the PRIME model for protein aggregation to all 20 amino acids. *Proteins-Structure Function and Bioinformatics* **78**, 2950-2960 (2010).

- [112] H. D. Nguyen, C. K. Hall, Molecular dynamics simulations of spontaneous fibril formation by random-coil peptides. *Proceedings of the National Academy of Sciences of the United States of America* **101**, 16180-16185 (2004).
- [113] A. HC, Molecular dynamics simulations at constant pressure and/or temperature. *The Journal of Chemical Physics*, 2384-2393 (1980).
- [114] Y. Wang, Q. Shao, C. K. Hall, N-terminal Prion Protein Peptides (PrP(120-144)) Form Parallel In-register beta-Sheets via Multiple Nucleation-dependent Pathways. *Journal of Biological Chemistry* **291**, 22093-22105 (2016).
- [115] A. W. Hewitt, D. A. Mackey, J. E. Craig, Myocilin allele-specific glaucoma phenotype database. *Human Mutation* **29**, 207-211 (2008).
- [116] M. Faucher, J. L. Anctil, M. A. Rodrigue, A. Duchesne, D. Bergeron, P. Blondeau, G. Cote, S. Dubois, J. Bergeron, R. Arseneault, J. Morissette, V. Raymond, N. Quebec Glaucoma, Founder TIGR/myocilin mutations for glaucoma in the Quebec population. *Human Molecular Genetics* **11**, 2077-2090 (2002).
- [117] S. E. Hill, R. K. Donegan, E. Nguyen, T. M. Desai, R. L. Lieberman, Molecular Details of Olfactomedin Domains Provide Pathway to Structure-Function Studies. *PLoS One* **10**, e0130888 (2015).
- [118] R. K. Donegan, S. E. Hill, K. C. Turnage, S. D. Orwig, R. L. Lieberman, The glaucoma-associated olfactomedin domain of myocilin is a novel calcium binding protein. *Journal of Biological Chemistry* **287**, 43370-43377 (2012).
- [119] D. J. Selkoe, Alzheimer's disease: genes, proteins, and therapy. *Physiological Reviews* **81**, 741-766 (2001).
- [120] P. Westermark, U. Engstrom, K. H. Johnson, G. T. Westermark, C. Betsholtz, Islet amyloid polypeptide: pinpointing amino acid residues linked to amyloid fibril formation. *Proceedings of the National Academy of Sciences of the United States of America* **87**, 5036-5040 (1990).
- [121] T. Theint, P. S. Nadaud, D. Aucoin, J. J. Helmus, S. P. Pondaven, K. Surewicz, W. K. Surewicz, C. P. Jaroniec, Species-dependent structural polymorphism of Y145Stop prion protein amyloid revealed by solid-state NMR spectroscopy. *Nature Communications* **8**, 753 (2017).
- [122] A. Hatami, S. Monjazebe, S. Milton, C. G. Glabe, Familial Alzheimer's disease mutations within the Amyloid Precursor Protein alter the aggregation and conformation of the Amyloid-beta peptide. *Journal of Biological Chemistry* **292**, 3172-3185 (2017).
- [123] A. K. Schutz, T. Vagt, M. Huber, O. Y. Ovchinnikova, R. Cadalbert, J. Wall, P. Guntert, A. Bockmann, R. Glockshuber, B. H. Meier, Atomic-resolution three-

dimensional structure of amyloid beta fibrils bearing the Osaka mutation. *Angewante Chemie International Edition* **54**, 331-335 (2015).

- [124] M. I. Ivanova, S. A. Sievers, E. L. Guenther, L. M. Johnson, D. D. Winkler, A. Galaleldeen, M. R. Sawaya, P. J. Hart, D. S. Eisenberg, Aggregation-triggering segments of SOD1 fibril formation support a common pathway for familial and sporadic ALS. *Proceedings of the National Academy of Sciences of the United States of America* **111**, 197-201 (2014).
- [125] P. Krotee, S. L. Griner, M. R. Sawaya, D. Cascio, J. A. Rodriguez, D. Shi, S. Philipp, K. Murray, L. Saelices, J. Lee, P. Seidler, C. G. Glabe, L. Jiang, T. Gonen, D. S. Eisenberg, Common fibrillar spines of amyloid-beta and human Islet Amyloid Polypeptide revealed by Micro Electron Diffraction and inhibitors developed using structure-based design. *Journal of Biological Chemistry* **293**, 2888-2902 (2017).
- [126] M. K. Joe, S. Sohn, W. Hur, Y. Moon, Y. R. Choi, C. Kee, Accumulation of mutant myocilins in ER leads to ER stress and potential cytotoxicity in human trabecular meshwork cells. *Biochemical and Biophysical Research Communications* **312**, 592-600 (2003).
- [127] M. K. Joe, S. I. Tomarev, Expression of myocilin mutants sensitizes cells to oxidative stress-induced apoptosis: implication for glaucoma pathogenesis. *American Journal of Pathology* **176**, 2880-2890 (2010).
- [128] G. H.-F. Yam, K. Gaplovska-Kysela, C. Zuber, J. Roth, Aggregated myocilin induces russell bodies and causes apoptosis: implications for the pathogenesis of myocilin-caused primary open-angle glaucoma. *American Journal of Pathology* **170**, 100-109 (2007).
- [129] J. H. Fingert, A. F. Clark, J. E. Craig, W. L. Alward, G. R. Snibson, M. McLaughlin, L. Tuttle, D. A. Mackey, V. C. Sheffield, E. M. Stone, Evaluation of the myocilin (MYOC) glaucoma gene in monkey and human steroid-induced ocular hypertension. *Investigative Ophthalmology & Visual Science* **42**, 145-152 (2001).
- [130] A. R. Shepard, N. Jacobson, J. C. Millar, I. H. Pang, H. T. Steely, C. C. Searby, V. C. Sheffield, E. M. Stone, A. F. Clark, Glaucoma-causing myocilin mutants require the Peroxisomal targeting signal-1 receptor (PTS1R) to elevate intraocular pressure. *Human Molecular Genetics* **16**, 609-617 (2007).
- [131] T. V. Johnson, S. I. Tomarev, Rodent models of glaucoma. *Brain Research Bulletin* **81**, 349-358 (2010).
- [132] C. M. McDowell, T. Luan, Z. Zhang, T. Putliwala, R. J. Wordinger, J. C. Millar, S. W. John, I. H. Pang, A. F. Clark, Mutant human myocilin induces strain specific differences in ocular hypertension and optic nerve damage in mice. *Experimental Eye Research* **100**, 65-72 (2012).

- [133] I. Malyukova, H. S. Lee, R. N. Fariss, S. I. Tomarev, Mutated mouse and human myocilins have similar properties and do not block general secretory pathway. *Investigative Ophthalmology & Visual Science* **47**, 206-212 (2006).
- [134] D. Vollrath, Y. Liu, Temperature sensitive secretion of mutant myocilins. *Experimental Eye Research* **82**, 1030-1036 (2006).
- [135] S. Gobeil, L. Letartre, V. Raymond, Functional analysis of the glaucoma-causing TIGR/myocilin protein: integrity of amino-terminal coiled-coil regions and olfactomedin homology domain is essential for extracellular adhesion and secretion. *Experimental Eye Research* **82**, 1017-1029 (2006).
- [136] C. J. van der Heide, W. L. M. Alward, M. Flamme-Wiese, M. Riker, N. A. Syed, M. G. Anderson, K. Carter, M. H. Kuehn, E. M. Stone, R. F. Mullins, J. H. Fingert, Histochemical Analysis of Glaucoma Caused by a Myocilin Mutation in a Human Donor Eye. *Ophthalmology Glaucoma* **1**, 132-138 (2018).
- [137] K. G. Malmos, L. M. Blancas-Mejia, B. Weber, J. Buchner, M. Ramirez-Alvarado, H. Naiki, D. Otzen, ThT 101: a primer on the use of thioflavin T to investigate amyloid formation. *Amyloid* **24**, 1-16 (2017).
- [138] F. Chiti, M. Calamai, N. Taddei, M. Stefani, G. Ramponi, C. M. Dobson, Studies of the aggregation of mutant proteins in vitro provide insights into the genetics of amyloid diseases. *Proceedings of the National Academy of Sciences of the United States of America* **99 Suppl 4**, 16419-16426 (2002).
- [139] S. E. Hill, T. Miti, T. Richmond, M. Muschol, Spatial extent of charge repulsion regulates assembly pathways for lysozyme amyloid fibrils. *PLoS One* **6**, e18171 (2011).
- [140] D. M. Hartley, D. M. Walsh, C. P. Ye, T. Diehl, S. Vasquez, P. M. Vassilev, D. B. Teplow, D. J. Selkoe, Protofibrillar intermediates of amyloid beta-protein induce acute electrophysiological changes and progressive neurotoxicity in cortical neurons. *The Journal of Neuroscience* **19**, 8876-8884 (1999).
- [141] D. M. Walsh, D. M. Hartley, Y. Kusumoto, Y. Fezoui, M. M. Condron, A. Lomakin, G. B. Benedek, D. J. Selkoe, D. B. Teplow, Amyloid beta-protein fibrillogenesis. Structure and biological activity of protofibrillar intermediates. *Journal of Biological Chemistry* **274**, 25945-25952 (1999).
- [142] L. C. Zeng, Z. G. Han, W. J. Ma, Elucidation of subfamily segregation and intramolecular coevolution of the olfactomedin-like proteins by comprehensive phylogenetic analysis and gene expression pattern assessment. *FEBS Letters* **579**, 5443-5453 (2005).
- [143] S. I. Tomarev, N. Nakaya, Olfactomedin domain-containing proteins: possible mechanisms of action and functions in normal development and pathology. *Molecular Neurobiology* **40**, 122-138 (2009).

- [144] M. Torrado, R. Trivedi, R. Zinovieva, I. Karavanova, S. I. Tomarev, Optimedlin: a novel olfactomedin-related protein that interacts with myocilin. *Human Molecular Genetics* **11**, 1291-1301 (2002).
- [145] F. Topouzis, E. Anastasopoulos, Glaucoma – the Importance of Early Detection and Early Treatment. *European Ophthalmic Review* **13**, (2007).
- [146] R. Nuzzi, F. Tridico, Glaucoma: Biological Trabecular and Neuroretinal Pathology with Perspectives of Therapy Innovation and Preventive Diagnosis. *Frontiers in Neuroscience* **11**, 494 (2017).
- [147] A. C. Freise, A. M. Wu, In vivo imaging with antibodies and engineered fragments. *Molecular Immunology* **67**, 142-152 (2015).
- [148] T. Li, M. Vandesquille, F. Koukouli, C. Duffeffant, I. Youssef, P. Lenormand, C. Ganneau, U. Maskos, C. Czech, F. Grueninger, C. Duyckaerts, M. Dhenain, S. Bay, B. Delatour, P. Lafaye, Camelid single-domain antibodies: A versatile tool for in vivo imaging of extracellular and intracellular brain targets. *Journal of Controlled Release* **243**, 1-10 (2016).
- [149] C. H. van Dyck, Anti-Amyloid-beta Monoclonal Antibodies for Alzheimer's Disease: Pitfalls and Promise. *Biological Psychiatry* **83**, 311-319 (2018).
- [150] D. J. E. Huard, V. M. Crowley, Y. Du, R. A. Cordova, Z. Sun, M. O. Tomlin, C. A. Dickey, J. Koren, 3rd, L. Blair, H. Fu, B. S. J. Blagg, R. L. Lieberman, Trifunctional High-Throughput Screen Identifies Promising Scaffold To Inhibit Grp94 and Treat Myocilin-Associated Glaucoma. *ACS Chemical Biology* **13**, 933-941 (2018).